The Effect of Grain Refinement on the Oxidation Performance of MCrAlY alloys

Cory Kaplin

Submitted: February 2014

Department of Mining and Materials Engineering

A thesis submitted to McGill University in partial fulfillment of the requirements of a Doctorate of Philosophy in Engineering.

Abstract

MCrAlY's are a specific class of nickel-based superalloy primarily used as a thermal barrier coating (TBC) bond coat or for oxidation resistance. The focus of this thesis is to study the improvement of high temperature oxidation and corrosion performance of MCrAlY and related alloys through nanostructuring, from understanding the oxidation mechanism of grain refined materials to evaluation of their performance in a simulated service environment. Grain refinement of the metal substrate was shown to favour the formation of a single oxide layer of α-alumina that can prevent the formation of fast growing spinel oxides. Consequently lower overall oxidation rates are obtained, offering the possibility of longer service life for components and coatings.

Oxidation testing of conventional and bulk nanostructured NiAl samples consolidated by spark plasma sintering (SPS) reveals that while conventional samples have oxidation rates on the order of 10^{-11} $g^2/cm^4/s$ across all tested temperatures, nanostructured samples demonstrate decreasing oxidation rates with temperature, as low as 6.78×10^{-13} $g^2/cm^4/s$. This decrease in oxidation rate is attributed to an earlier transition through the metastable aluminum oxide phases. In-situ XRD during high-temperature oxidation testing has shown that lattice strain at the surface of the nanostructured samples is substantially higher than conventional, and that the decrease of this lattice strain with temperature is significant. It is believed that the relief of this lattice strain stimulates the earlier θ-α transition.

Ultrafine NiCoCrAlY samples have been obtained through cryomilling of NiCoCrAlY feedstock powder and sintering via SPS, these samples have been subjected to isothermal oxidation tests at 950, 1000 and 1050°C. In all cases cryomilled samples

demonstrate lower overall oxidation rates than their conventional counterparts. This is ascribed to an earlier transition trough the metastable alumina phases, resulting in a stable slow growing α-Al_2O_3. Lower rates seen at 1050 than at 1000°C in both conventional and cryomilled samples are the result of a change from oxidation dominated by θ-alumina to oxidation dominated by α-alumina, as the θ-α transition speeds up with increasing temperature.

Nanostructured HVOF-deposited NiCoCrAlY coatings were subjected to high temperature oxidation tests in both air and an environment containing SO_2 and varying levels of water vapour. It has been found that the oxides formed under all conditions are alumina followed by a spinel phase. In both air and the SO_2 environment an increase in total mass gain was seen up to 4% water vapour, followed by a decrease at 6 and 8%. This behaviour is attributed to an extension of the transient oxidation stage, resulting first in a variation in scale thickness through increased spinel growth and second in a rise in internal oxidation caused by increased oxygen transport through the scale in the presence of water vapour. It would appear that above 4% water vapour the thickened spinel is able to compensate for alumina loss and create a diffusion barrier to internal oxidation, once again reducing mass gain.

Lastly, NiCoCrAlY samples fabricated via SPS underwent thermal cycling oxidation tests at 1000°C in air for up to 200 1-hour cycles. Mass gain is notably lower in the cryomilled NiCoCrAlY samples. In both the conventional and cryomilled samples, characterization indicates a single layer oxide scale of α-alumina has formed, having undergone a transition from θ-alumina during oxidation testing. Spallation in the conventional sample allowed a significant amount of internal spinel oxide formation, while this was not found in the cryomilled sample. The difference in behaviour is attributed to increased pathways for aluminum diffusion to the surface and nucleation sites for the α-alumina transition, as well as improved scale adhesion through nanostructuring and stress relief through the accelerated θ-α transition.

Résumé

La famille des alliages MCrAlY est une classe de Superalliages à base de nickel principalement utilisés en tant que revêtement ou afin d'augmenter la résistance à l'oxydation. Cette thèse portera principalement sur l'étude de l'amélioration de l'oxydation à haute température et du comportement en corrosion chaud du MCrAlY et de ses alliages par l'étude de leur nanostructure en développant la compréhension des mécanismes d'oxydation des matériaux à grains raffinée jusqu'à l'évaluation de leur performance en environnement simulé. Il a été démontré que l'affinement de la taille des grains favorise la formation d'une couche d'oxyde simple d'alumine α qui prévient la croissance rapide des oxydes spinel. Ainsi, le taux d'oxydation est réduit ce qui permet une longévité en service accrue pour une grande variété de pièces et de revêtements.

Des essais d'oxydation d'échantillons de NiAl conventionnels ainsi que d'échantillons de NiAl nanostructurés fabriqués par SPS révèlent qu'alors que les échantillons conventionnels présentent des taux d'oxydation de l'ordre de 10^{-11} $g^2/cm^4/s$ pour toute l'étendue des températures testées, les échantillons consolidés par SPS montrent un taux d'oxydation diminuant avec la température atteignant un minimum de $6{,}78 \times 10^{-13}$ $g^2/cm^4/s$. Cette diminution du taux d'oxydation est attribuable à une transition plus rapide des phases métastables de l'oxyde d'aluminium. L'étude par XRD in situ lors d'essais d'oxydation à haute température a révélé une contrainte du réseau beaucoup plus élevée à la surface des échantillons nanostructurés que pour les échantillons conventionnels ainsi qu'une diminution significative de cette contrainte avec la température. Il est donc possible de croire que l'allégement de la contrainte du réseau stimule une accélération de la transition θ-α.

Des échantillons de NiCoCrAlY ultrafins ont été obtenus en broyant cryogéniquement une poudre brute d'alliage et en frittant par SPS la poudre résultante. Ces échantillons ont été soumis à des essais d'oxydation à températures constantes de 950, 1000 et 1050°C. Dans tous les cas les échantillons cryogéniquement broyés ont montré des taux d'oxydation plus lents que leurs équivalents conventionnels. Cette réduction du taux d'oxydation est attribuée à une transition plus rapide des phases métastables de l'alumine laissant plutôt place à l'alumine α, une phase stable à croissance lente. Les taux d'oxydation plus lents à 1050 qu'à 1000°C pour les échantillons conventionnels et cryogéniquement broyés sont le résultat du changement de l'oxydation dominée par la phase d'alumine θ vers l'alumine α, la transition θ-α s'effectuant plus rapidement à température plus élevée.

Également, des revêtements nanostructurés de NiCoCrAlY déposés par HVOF ont été soumis à des essais d'oxydation à haute température dans l'air et dans un environnement contenant du SO_2, tous deux avec différents niveaux de vapeur d'eau. Il a été observé que les oxydes formés dans toutes les conditions sont d'abord de l'alumine suivi par une phase de spinel. Dans les deux types d'environnements une augmentation du gain de masse totale a été observée jusqu'à un taux de vapeur d'eau de 4% suivi d'une diminution à 6 et 8%. Ce comportement est attribué à une extension de l'étape d'oxydation transitoire menant d'abord à un changement de l'épaisseur de la couche d'oxyde causée par une augmentation de la croissance des spinel et ensuite par une augmentation de l'oxydation interne causée par l'augmentation du taux de transport d'oxygène dans la couche d'oxyde en présence de vapeur d'eau. Il semble qu'au dessus de 4% de vapeur d'eau la couche de spinel épaisse est capable de compenser pour la perte d’alumine et de créer une barrière contre l’oxydation interne réduisant ainsi le gain de masse.

Finalement, des échantillons de NiCoCrAlY fabriqués par SPS ont été exposés à des essais d’oxydation par cycles thermiques à 1000°C dans l’air pour un maximum de 200 cycles d’une heure. Le gain de masse est significativement plus faible dans le cas des échantillons broyés cryogéniquement. De plus, la caractérisation des échantillons conventionnels et cryobroyés révèle la présence d’une couche simple d’alumine α provenant de la transition de l’alumine θ lors de l’essai d’oxydation. La spallation dans l’échantillon conventionnel a permis la formation d’une quantité considérable de spinel internes alors que ce comportement n’a pas été observé dans l’échantillon cryogéniquement broyé. Cette différence de comportement est attribuée au plus grand nombre de voies disponibles pour la diffusion de l’aluminium vers la surface ainsi qu’à la présence de plus de sites de nucléation pour la transition de l’alumine α et à l’adhésion accrue de la couche d’oxyde due à la nanostructuration et la diminution de la tension lors de la transition θ-α accélérée.

Acknowledgements

First and foremost I would like to thank my wife, Anik, for her love and support over the years. The idea of doing a PhD was hers in the first place, and I thank her many times over for helping to guide me in my chosen path. I would like to thank my family as well for their endless encouragement and for putting up with all the science at the dinner table.

My supervisor Mathieu has been a trusted ally and advisor throughout my time at McGill. I know that along with all his help face-to-face, he has always been in my corner behind the scenes, making sure his students are in good stead. I have Mathieu to thank for the fantastic experience that grad school has been, and for giving me the chance to take the trip of a lifetime during my studies.

My friends and coworkers at McGill have been, without a doubt, the best support team any student could ask for. To all the members of NAINlab, past and present: Dom, Jason, all three Daves, Pat, Alex, Nesli, Bamidele, Rabab, Jesus, Rosen, Beto, Masum Marie-Pier, Phil, Sam, Ramona, Yaneth and Graeme and to all those honorary members who figured it out just a bit too late: Cecile, Florencia, Pantcho, Renaud, Holger, Mert, Nate, Ryan, Huseyin, Schockley, Pinard, and the unforgettable Musti, I thank you for putting a smile on my face every day for over 5 years. A special thanks goes to Dave and Jay for helping me in the pursuit of awesomeness, and to our office mates Deniz, Lydia and Dong Geun for putting up with the pursuit of awesomeness. Prof. Jung, Sriraman, Manas, Justine, Holger, Rosen, Saikat, Alex and Graeme have each helped make this research possible in some way, and I remain in their debt.

The administrative staff in the department have always been ready to lend a helping hand or bend a rule to make life easier, to Barbara, Terry and Courtney I say thank you, your help has always been appreciated. The same should be said for the department technical staff: Monique, Ray, Robert, Helen and Lou, who have been integral in getting this project off the ground. I would like to extend an extra thanks to Barbara Hanley, without whom my travels would have been impossible.

Finally I would like to thank the Natural Science and Engineering Research Council of Canada (NSERC) for the Alexander Graham-Bell Canada Graduate Scholarship, Hydro-Quebec and the McGill Faculty of Engineering for the Hydro-Quebec McGill Engineering Doctoral Award (MEDA), and Imperial Oil for their financial support of this research.

Author Contributions

This thesis has been constructed as a manuscript-based format and contains four manuscripts either published or in the process of submission for publication. Chapters 4 through 7 are individual manuscripts and are presented accordingly. The contributions of the various co-authors are listed below.

- Mr. Rosen Ivanov performed sample preparation and transmission electron microscopy analysis of consolidated nanostructured NiAl samples in Chapter 4.
- Dr. Manas Paliwal provided technical expertise as well as assistance with thermogravimetric analysis of consolidated NiAl samples in Chapter 4.
- Prof. In-Ho Jung provided technical expertise for thermogravimetric analysis in Chapter 4.
- Ms. Justine Fassoni provided assistance with sample consolidation and preparation, as well as conducted thermal cycling experiments and mass gain analysis of consolidated NiCoCrAlY samples in Chapter 7.
- Prof. Mathieu Brochu supervised the overall project while offering technical and scientific input for each manuscript.

Table of Contents

List of Figures

List of Tables

Chapter 1: Introduction

1.1 Introduction

Corrosion and oxidation are among the most common issues affecting major industries throughout the world. An often-cited report by the National Association of Corrosion Engineers estimated that the total direct cost of corrosion and oxidation in United Sates was $276 billion in 2002, amounting to some 3.1% of America's GDP [1.1]. This figure is equivalent to roughly $500 billion in 2013 dollars, and as such should be considered a major economic interest. In some sectors, the cost of oxidation and corrosion can amount to as much as 7% of total industry turnover [1.2].

Among the most challenged are those industries working at high temperatures, where corrosion and oxidation problems can be exacerbated. It is estimated that over 40% of industrial products require high temperature for production or processing [1.3], and this can result in significant degradation and reduced lifetime of various components. Figure 1.1 presents the expected component lifetime as a function of operating temperature for a range of extreme industrial applications [1.4].

Two applications of particular interest for this thesis are aero- and land-based gas turbines and petrochemical refining. Both involve very high operating temperatures and a range of oxidation and corrosion issues. Aerospace materials suffer from wide variety of corrosion problems, ranging from general oxidation to stress corrosion cracking, hydrogen embrittlement to galvanic corrosion [1.5]. Within the turbine itself, extreme stresses due to temperature gradients, thermal cycling, and high loads also can intensify corrosion and oxidation processes.

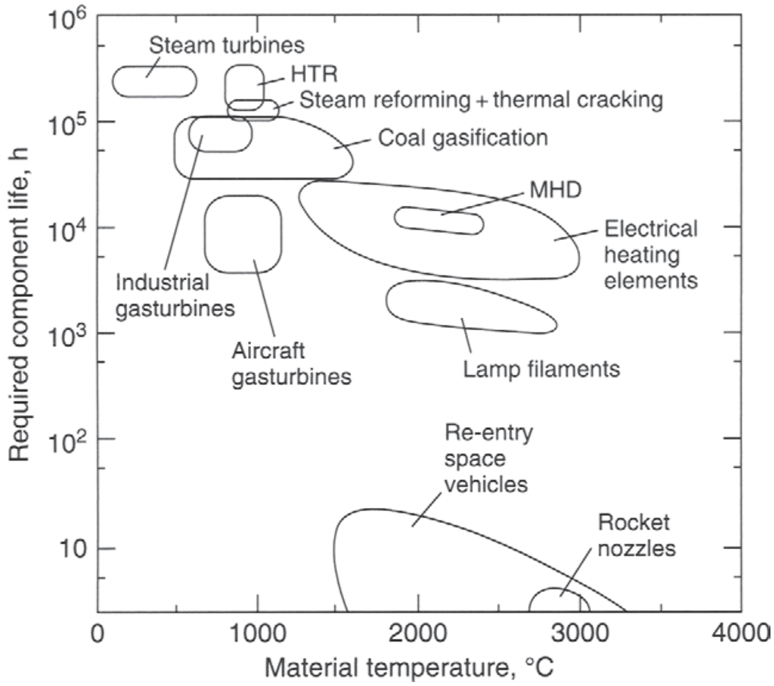

Figure 1.1: Component lifetime as a function of operating temperature for various industrial applications [1.4].

Corrosion and oxidation can be particularly detrimental in the petrochemical industry; corrosion control can often account for 60% to 70% of a plant's maintenance budget [1.6]. Sulphur evolves from the refining process and is present in effluent gasses as H_2S, H_2SO_4, and most notably SO_2. Other issues include atmospheric corrosion, various forms of aqueous corrosion by acids evolved in the process and the presence of water, both internal to refining process and externally in many extracting and refining platforms [1.7]. Combined with the high temperatures found in boilers and other components, a significant maintenance issue arises.

In both industries the current trends in corrosion prevention are the selection of materials with inherent corrosion resistance, the application of protective coatings and careful design to minimize potential corrosion areas [1.5, 1.7]. In the first and second case, a number of high temperature alloys have been employed that harness passivating oxidation behaviour as a method of preventing further corrosion and oxidation. These alloys include chromium or aluminum as alloying elements in sufficient concentration that they will form an oxide scale of either chromia or alumina Between the two, alumina is considered the most protective [1.8]. At temperatures in excess of 1000°C, alumina-formers are said to offer the best possible oxidation and corrosion resistance through the formation of a very stable and non-reactive coating. This being said, limitations remain in terms of mechanical properties of corrosion resistant bulk materials and element depletion in coatings [1.8]. As a result, there exists a constant challenge to improve the oxidation performance of these various alloys and extend component lifetime accordingly, which could yield as much as an estimated 30% in savings over the total cost of corrosion in the United States [1.2].

1.2 Nickel superalloys

Superalloys are a class of metal alloy designed for high temperature applications that exhibit a combination of mechanical strength and resistance to degradation; they have been necessary for many industrial advances over the last 50 years. Primary uses of superalloys include gas turbines, power generation, chemical and petrochemical processing and of course aerospace applications [1.9].

Among the most common superalloys are those based on Nickel, these are noteworthy in that they can be used in load bearing application at up to 80% of their melting temperature, higher than any other engineering alloys [1.10]. The most common alloying elements are Co, Cr, Mo, Al, Ti and Fe either in solid solution or as second and third phases. An overview of the alloying elements and their benefits can be seen in

Figure 1.2. The most well-known alloy series are Hastelloy (Cr and Mo rich), Inconel (Co and Mo rich), Nimonic (Co and Cr rich, often with Al) and Réné (containing Co, Cr, Mo and Al) [1.10]. Both Nimonic and Réné series can fall under the MCrAlY category of alloys, to be discussed in a later section.

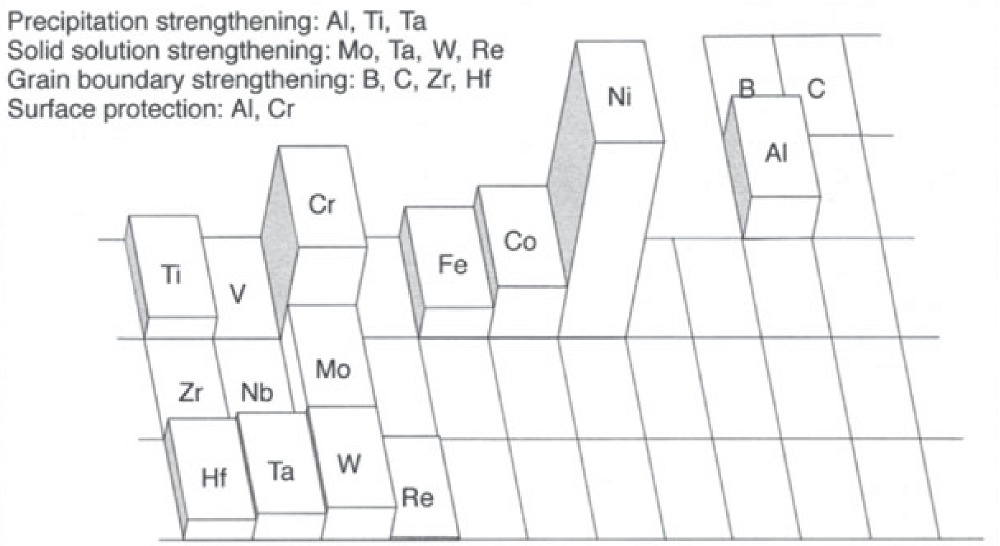

Figure 1.2: Major alloying elements in nickel-base superalloys [1.9].

There are several major phases that can be found in Ni-base alloys [1.10]. The primary matrix, γ, is a face-centered cubic (FCC) nickel phase with high solid solubility for numerous elements including Co, Fe, Cr and Mo, among others. Coherent precipitates of Ni_3Al and Ni_3Ti are denoted as the γ' phase are responsible for high temperature strength and creep resistance. Coherent body-centered tetragonal (BCT) Ni_3Nb precipitates are known as γ'' and give significant mid-temperature strength to Ni-Fe superalloys, but become unstable at higher temperatures. Body-centered cubic (BCC) NiAl, the β phase, provides environmental resistance and will be discussed in the next section. Carbides formed with various reactive elements are also possible, and sometimes form in-service.

Oxidation resistance in nickel superalloys began with the addition of chromium as an alloying element first in the Brightray series of alloys followed by Inconel [1.9]. Later, the addition of aluminum led to increased oxidation resistance and the development of the MCrAlY series. It is important to note, however, that historically the addition of Al or Cr to improve environmental resistance has been met with a loss of mechanical properties [1.11] and thus the ongoing trend of using protective coatings of various Ni-base alloys either as a mechanically sound substrate or as protective outer layer is of interest.

1.2.1 NiAl Alloys

Nickel-aluminum alloys have been of interest to many industries, particularly aerospace, for over 3 decades. High melting temperatures, good environmental resistance, and relatively inexpensive raw material cost have been some of the driving factors for the research and development of these alloys [1.12]. The Ni-Al phase diagram is presented in Figure 1.3, of particular interest are the numerous intermetallic phases. NiAl and Ni_3Al are common phases in nickel-base superalloys, as discussed previously, and have melting points of 1638 and 1385°C respectively. Also, due to the large portion of aluminum, these phases offer significant density reduction in nickel alloys [1.13].

Despite relatively poor room temperature toughness and high temperature creep resistance, NiAl offers a number of advantages over other nickel-base alloys [1.14]: first, the density of NiAl (5.95 g/cm^3) is roughly 30% less than most nickel base superalloys. The thermal conductivity of NiAl is typically 4 to 8 times greater than Ni-base superalloys. NiAl possesses excellent oxidation resistance through the formation of an alumina scale. NiAl possesses a lower ductile-to-brittle transition temperature than other intermetallics. Finally NiAl has an extremely high melting temperature, as noted in the previous paragraph.

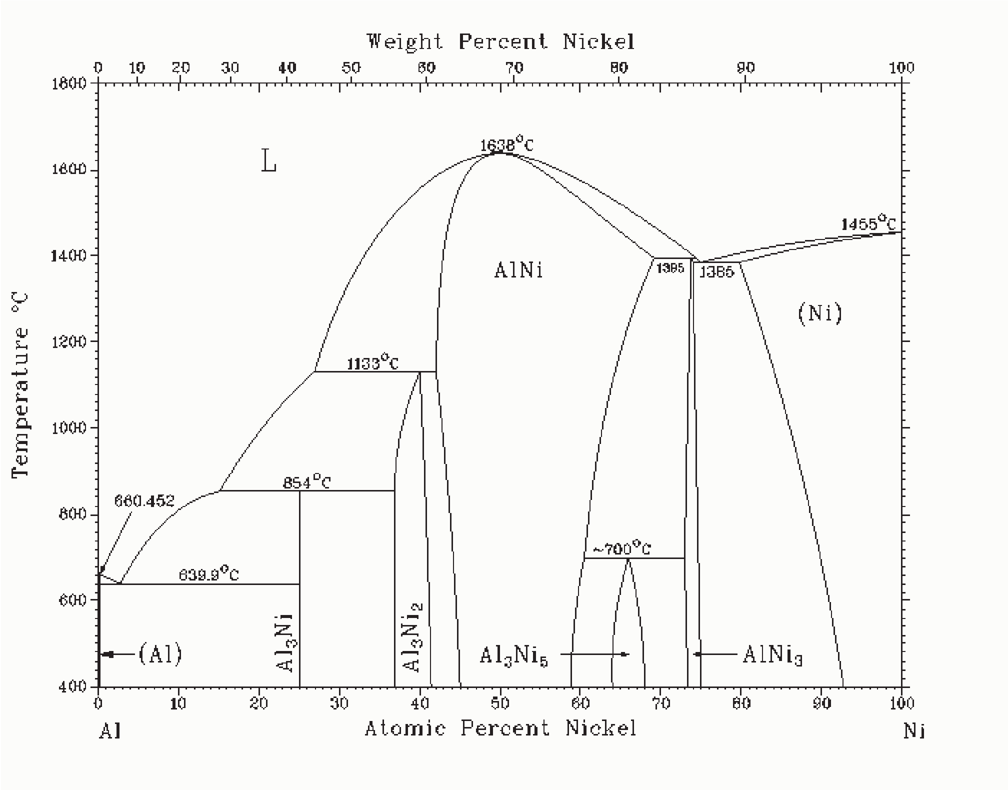

Figure 1.3: The Ni-Al phase diagram [1.10].

Interest in NiAl dates back as far as 1952, with exploratory studies into high temperature properties, followed by processing and mechanical property studies in the 1960's [1.15]. Plagued by the low temperature brittleness issues mentioned previously, research slowed in the late sixties and seventies, though a small number of researchers continued a steady research campaign. Beginning in the 1970's with Goward *et al.*, research into the environmental resistance of NiAl arose, including its use as a coating material, rather than structural components [1.16]. In the eighties, Smialek and Meier were among the first to identify the extremely low oxidation rate of the protective scales formed on NiAl [1.17]. At the same time, a number of other avenues of research were launched, including surface science and catalytic behaviour, use as an interconnect material for the electronics industry, along with a renewed interest in structural applications among government aerospace research programs [1.17]. This being said, the "modern era" of NiAl research, beginning in the late 80's, has been focused in large part on the oxidation properties of both bulk and coated NiAl alloys and the related superalloys.

The β-NiAl intermetallic has a cubic ordered B2 structure, consisting essentially of two interlocking unit cells, with Ni atoms occupying the corner of one sub-unit cell and Al occupying corner positions of the second sub-unit cell [1.18]. This structure is stable over a relatively wide concentration range and significant long-range order is maintained up to the melting point of 1638°C. A martensitic transformation has been found in Ni-rich NiAl alloys [1.18], though most current research, including this thesis, is focused on stoichiometric NiAl or concentrations very close to it.

Several major trends exist in the current research on NiAl. The logical first among these is the synthesis of NiAl intermetallic from Ni and Al precursors. Numerous studies dating from 1994 to present have cited mechanical alloying, using different high energy milling techniques, among the most efficient processes to achieve this [1.19-1.22]. Because of the high thermal stability of NiAl intermetallic, many of these studies focus on nanostructured powders. Joardar *et al.* have conducted some of the most extensive research on the milling of NiAl [1.23, 1.24] and have determined ideal conditions for the synthesis of NiAl intermetallic, as a function of milling time and ball-to-powder ratio [1.24]. The determined that a minimum energy input must be attained to fully synthesize NiAl intermetallic, be it by increased milling time, milling speed, or ball-to-powder ratio.

The bulk of these studies were conducted on planetary ball mills, however in 2012 Kubaski *et al.* explored milling in both planetary and attritor mills under various conditions [1.22], finding that in fact that under optimized conditions attritor mills had the most efficient conversion to NiAl.

A second major research trend is the addition of various alloying elements or dopants to NiAl. Numerous studies have explored elemental additions, in particular yttrium [1.25, 1.26], platinum [1.27, 1.28], hafnium [1.28-1.30], finally Gong, Hu and coworkers have conducted numerous studies on the addition of dysprosium [1.30-1.32]. Most of these studies have an interest in improving oxidation properties of NiAl alloys and are based on the work of Pint *et al.* in 1997, who explored the effect of various dopants on the oxidation behaviour of NiAl [1.33]. The authors determined that many of these dopants can improve oxidation rate by affecting the metastable transition in the alumina phase. The transitional phases of alumina will be discussed in greater detail in the oxidation section.

1.2.2 MCrAlY alloys

MCrAlY's are a specific class of nickel-based superalloy primarily used as a thermal barrier coating (TBC) bond coat or for oxidation resistance where M = Ni, Co or both. They were initially developed in the early 1970's as "overlay" coatings and offered several advantages over other coating materials at that time, including NiAl [1.34]; these alloys offer a wider range of compositions that yields the possibility of tailoring properties. In particular, compositional variation has the potential to improve oxidation resistance or offer superior ductility over other coatings. Also, better scale adhesion was attributed to Y addition [1.34]. It would appear the benefits of MCrAlY coatings have remained relevant, as these materials continue to experience wide spread use today.

The most common MCrAlY alloys currently used are NiCoCrAlY and CoNiCrAlY with aluminum concentrations in the range of 8 to 12% by mass. Ni is the base element of these alloys due to the high temperature properties of Ni base superalloys mentioned in section 1.2. The addition of Al provides high temperature oxidation resistance, as in the case of NiAl [1.35]. However, as the addition of Al can have a detrimental effect on some mechanical properties, Cr is added in the range of 16 to 22% and serves to lower the minimum threshold of Al to form an alumina scale [1.8]. Cr can also offer oxidation resistance in mid-temperature ranges and improve hot corrosion resistance [1.4].

The simple Ni-Cr-Al system generates a phase structure that is consistent across all MCrAlY alloys. The ternary phase diagram of Ni-Cr-Al is presented in Figure 1.4 [1.4]. The γ-Ni phase forms the primary matrix of the alloy and is soluble to Cr. The β-NiAl intermetallic is the second phase to form and provides the aluminum necessary for good oxidation resistance. The γ' Ni_3Al phase is also possible and is occurs as coherent precipitates within the γ phase, and is said to improve the mechanical properties of MCrAlY alloys [1.36].

Cobalt is generally added to Ni-base superalloys as a phase stabilizer; in the case of MCrAlY alloys it enters into solid solution in the γ phase and serves to stabilize the β-NiAl phase, maintaining the γ-β structure over a wider range of compositions [1.4, 1.37]. Studies have shown that Y addition helps slow the growth of non-alumina oxides during the initial stages of oxidation [1.35]. A the typical γ-β microstructure of MCrAlY alloys is shown in Figure 1.5 [1.38]. Compositional variations, in general, are used to tailor the ratio of these two phases and accordingly tailor oxidation resistance and other properties.

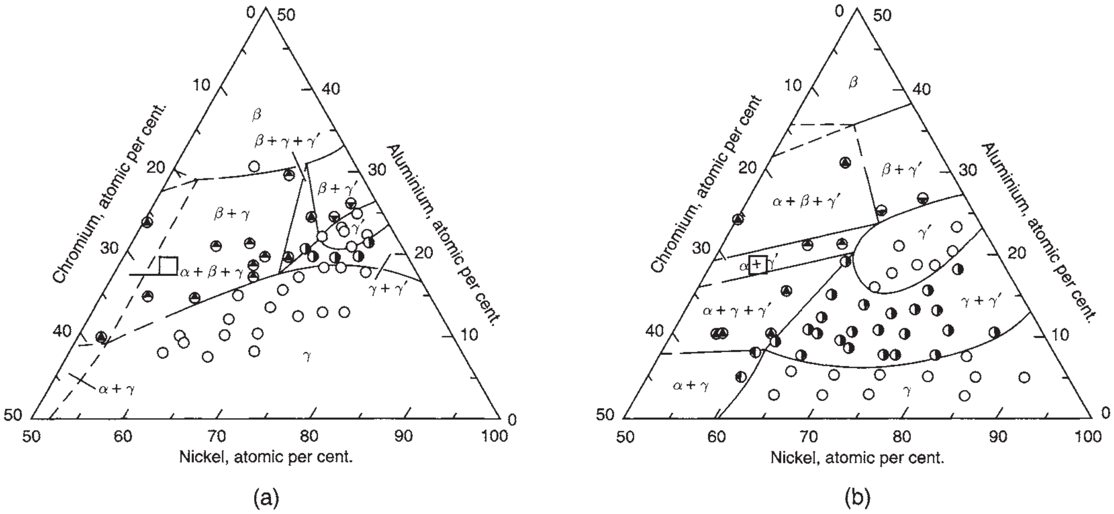

Figure 1.4: Ternary phase diagram of Ni-Cr-Al at 1150°C (A) and 850°C (B) [1.4].

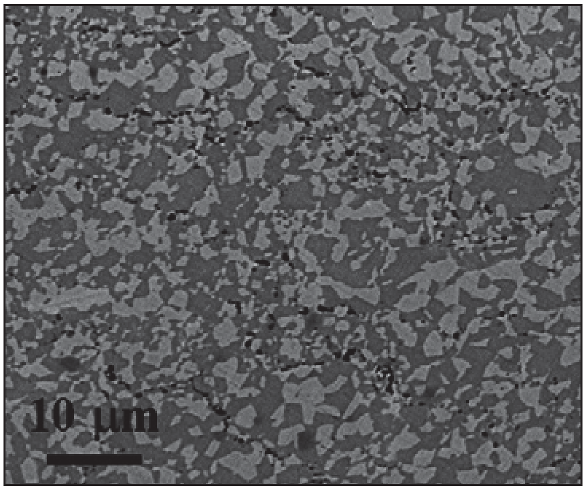

Figure 1.5: A typical MCrAlY microstructure of γ (light) and β (dark) [1.38].

The first MCrAlY coatings were deposited by electron-beam physical vapour deposition (EB-PVD) [1.34], and a number of studies have explored this deposition method [1.36, 1.39-1.43]. In this case, vaporized MCrAlY alloy is deposited onto components and normally requires post-deposition treatment such as shot peening to reduce defects. Many researchers have sought the “ideal” post-treatment. More recently, thermal spray deposition methods such as low-pressure plasma spray (LPPS) and high-velocity oxy-fuel spray (HVOF) have become increasingly competitive [1.34] and have been studied extensively [1.44-1.51]. In thermal spray processes molten or semi-molten powders are sprayed at high velocities onto the superalloy substrate and deposit to form a coating. With parameter optimization these processes can preserve aspects of powder morphology, allowing for more microstructural control in the deposited coatings [1.4].

As MCrAlY alloys are primarily used in high temperature environments, several researchers have investigated the high temperature phase stability of these alloys. One of the first comprehensive modelling studies, undertaken by Quadakkers and coworkers [1.52] explored the stabilizing effect of Co on the γ-β structure at high temperature. Several later studies were carried out by Buršík *et al.* [1.38], Hemker *et al.* [1.44, 1.53], Nijdam *et al.*, [1.40] and Liang *et al.* [1.54] establishing a relative understanding of the high temperature phases present in MCrAlY alloys. However, due to the wide range of alloy compositions that fall under the class of MCrAlY, results can vary substantially from one study to another. A comprehensive thermodynamic modelling study in 2010 by Ma and Schoenung [1.55] has unified much of this work. Across the range of compositions and temperatures the γ and β phases generally remain stable, the addition of Co helps in this. However, Co additions can also reduce the portion of the γ’ strengthening phase, though it is widely accepted that this phase dissolves in the range of 800 to 950°C. Excessive Co addition can cause the formation of the brittle Cr-based σ phase, to the detriment of mechanical properties. Finally, across several of the studies cited, it is accepted that the fraction of β-phase present is proportional to the aluminum composition.

1.3 Oxidation

Oxidation is a form of corrosion wherein metals and alloys react in the presence of oxygen or other oxygen-bearing environments. The result of oxidation is the formation of an oxide scale which, depending on the scale that forms, can either degrade or protect the underlying metal [1.3]. In its simplest form, the oxidation reaction can be described as follows:

$$2M(s) + O_2(g) = 2MO(s) \qquad \text{Eq. 1.1}$$

From a thermodynamic standpoint, the oxidation reaction will occur when the oxygen potential in the surrounding environment exceeds the equilibrium oxygen partial pressure of the oxide [1.3]. This equilibrium oxygen pressure is determined from the standard free energy of formation of the oxide. Assuming ideal behaviour of solid constituents (i.e. the metal and the oxide), the equilibrium partial pressure can be determined through equation 1.2:

$$p(O_2) = exp(\Delta G°/RT) \qquad \text{Eq. 1.2}$$

Where $p(O_2)$ is the equilibrium oxygen partial pressure, $\Delta G°$ is the free energy of formation of the oxide, R is the ideal gas constant and T is temperature. The Ellingham diagram, commonly used to represent the thermodynamic likelihood of an oxide to form, is essentially a graphical representation of this relationship for a number of oxides. It is presented in Figure 1.6. In general strong oxide formers are located lower on the diagram and weak oxide formers are higher on the diagram [1.56].

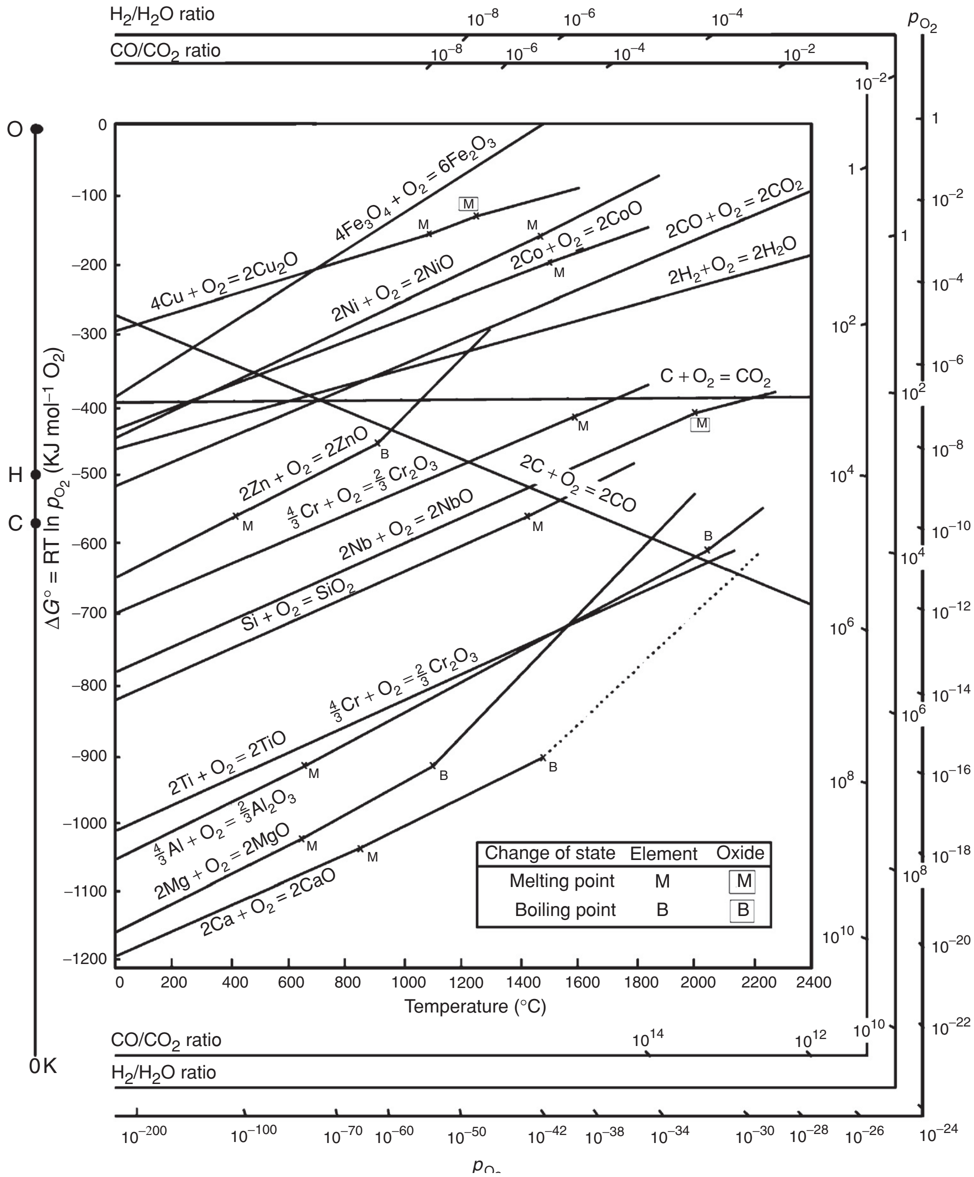

Figure 1.6: Standard free energy of formation for selected oxides as a function of temperature [1.56].

While thermodynamics can offer information on oxides that will form in equilibrium and the relative stability of these oxides, real-world oxidation behaviour involves equally important kinetic considerations. A kinetic approach to oxidation is complementary to thermodynamics as it explores the rate at which oxides will form, rather than which oxides those are [1.57]. Kinetics can be explored by monitoring the amount of metal consumed in the oxidation reaction, the amount of oxygen consumed, or the amount of oxide produced [1.56]. Of the three methods, the third is the most commonly used and arguably the most practical, through constant monitoring of weight gain of the oxidized sample.

Oxidation kinetics have been found to follow several possible rate laws. The first case is the linear law, wherein the rate of reaction is constant regardless of time. In general linear oxidation is controlled by the surface reaction step or by diffusion of oxygen through the gas phase [1.56]. In the second possible rate law, oxidation is controlled by the diffusion of species through the oxide scale and is proportional to the square root of time [1.56], this is known as parabolic oxidation. Finally the logarithmic law is generally only associated with the formation of very thin oxide films at low temperatures. For the purposes of oxidation resistance, parabolic behaviour is desired, as the oxidation rate drops over time with the formation of an oxide scale that blocks diffusion of oxygen, metal(s) or both [1.3].

In general the transport mechanisms within oxides can fall into two broad categories as identified by Wagner [1.56]. First, consider the reaction in Eq. 1.1. In the physical sense, this can be represented by the schematic in Figure 1.7. In order for the oxidation reaction to continue, oxygen must travel through the oxide scale to react with the metal, or metal ions must travel through the oxide to react with the oxidizing gas. In both cases transport is achieved through defect in the oxide scale. In negative semiconducting (n-type) oxides, transport is achieved through negative carriers, either an excess of metal ions or a deficit of non-metal ions [1.56]. In positive semiconducting (p-type) oxides, transport is achieved through positive carriers, either through a deficit of metal ions or an excess of non-metal ions [1.56]

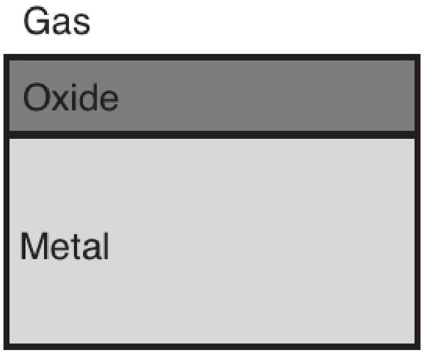

Figure 1.7: Schematic representation of basic oxidation.

High temperature conditions can enhance diffusion in materials and reaction rates, and therefore have a significant effect on oxidation. In this case the need for protection of metals from breakaway oxidation, fast growing oxides, or spallation is undeniable. Several potential oxidation behaviours at high temperature are presented in Figure 1.8 [1.57]. Corundum, α-alumina, is one of the lowest oxides on the Ellingham diagram (Figure 1.6) and is considered the most stable and protective oxide scale at high temperatures [1.58]. The transport mechanisms in Al are not fully understood as there is no reliable Al isotope for use in tracer experiments, however tracer experiments using oxygen have revealed very high activation energies for oxygen transport across the scale both through lattice diffusion and grain boundary diffusion [1.58]. It is this restriction on ionic transport that yields such a protective oxide scale. Consequently, the addition of aluminum in order to form a protective oxide scale is one of the guiding principles in MCrAlY alloy development and the reason for their superior oxidation performance.

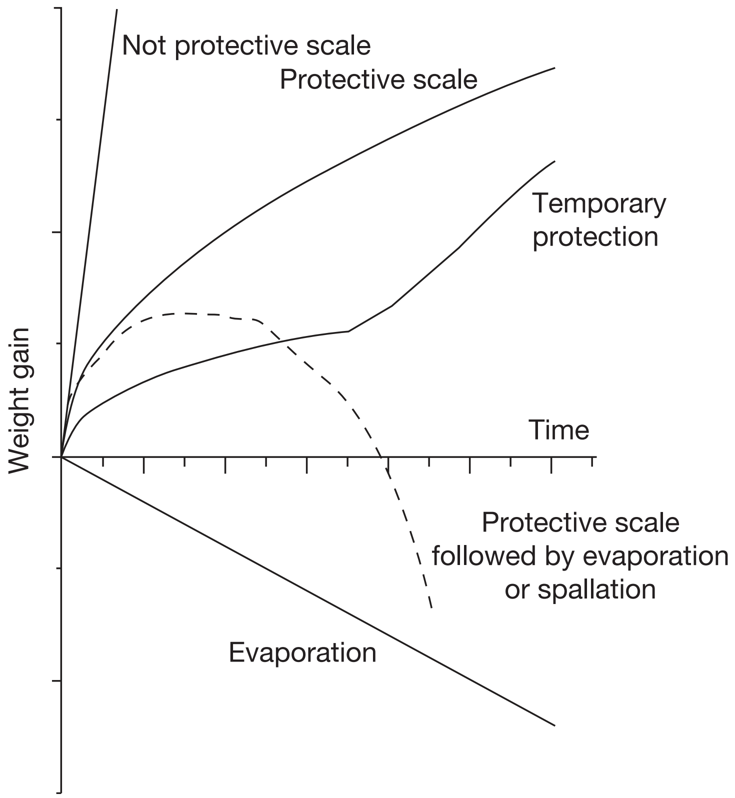

Figure 1.8: Various oxidation kinetics observed a high temperature [1.57].

1.3.1 Oxidation of NiAl alloys

The oxidation resistance for which NiAl alloys are most known is due to their ability to form an aluminum oxide scale through the selective oxidation of Al. As discussed in the previous section, the extremely low free energy of formation, alumina is among the most thermodynamically stable oxides and also among the most likely oxides to form on the surface of an alloy. Above 30 at% aluminum, NiAl alloys form exclusive external scales of alumina, and this compositional range can be extended at higher temperatures [1.56]. Figure 1.9 presents the possible oxides formed.

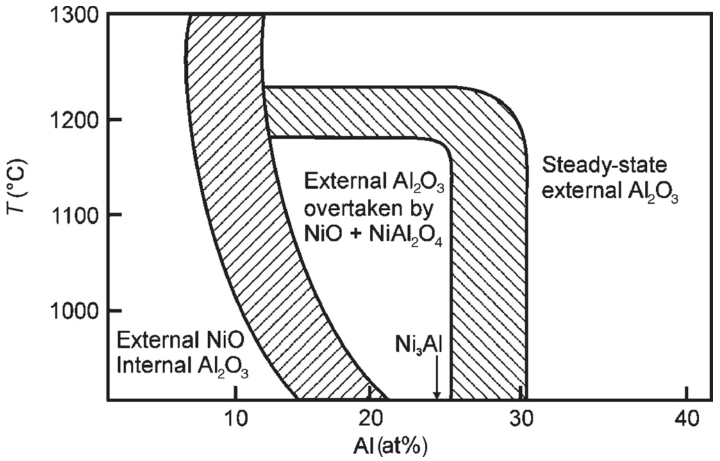

Figure 1.9: Oxides formed on NiAl as a function of temperature and aluminum concentration [1.56].

For the stoichiometric range of intermetallic β-NiAl oxidation, in its most simplistic interpretation, will follow classic parabolic oxidation kinetics as described by Pierragi [1.59]. In this case oxidation can be described by the simple equation:

$$\Delta m^2 = k_p (t) \qquad \text{Eq. 1.3}$$

Where Δm is mass gain, k_p is the parabolic rate constant, and t is time. This type of oxidation occurs when the oxidation reaction is diffusion limited through the oxide scale that forms, this diffusion block serves as a passivating, protective layer [1.56].

Extensive research has been conducted on the underlying oxidation mechanisms of NiAl. The transient oxidation mechanism was elucidated in the 90's by Brumm and Grabke [1.60, 1.61] as well as Yang *et al.* [1.62]. They established that the growth of the alumina scale on the NiAl surface transitions through several metastable structures, namely δ-Al_2O_3, γ-Al_2O_3 and θ-Al_2O_3 before eventually transforming to the stable corundum α-Al_2O_3 phase. These transitions are also accompanied by microstructural transformations. In all cases the aluminum lattice is close packed, however the oxygen lattice will change with each transitional phase [1.63]. The initial δ and γ phases have an overall microstructure that is cubic, and this will transform to the monoclinic θ phase with a corresponding 11% increase in density. Monoclinic θ will then transform into rhombohedral α-Al_2O_3 resulting in another 12% increase in density [1.63]. The final α-Al_2O_3 corundum phase is the stable phase that is most desirable, as this structure has the slowest diffusion properties and results in a highly dense passivating oxide layer [1.60]. The extensive work of Brumm and Grabke revealed the time-temperature dependence of the θ-α transition, finding that at 900°C the initial oxide formed is γ with a relatively quick transition to θ while the transition to α can be measured in hundreds of hours. At higher temperatures, ranging form 950 to 1050°C, the θ-α transition becomes the controlling oxidation step, and this transition results in a comparative drop in oxidation rates between early-stage and late-stage oxidation. Finally at temperatures in excess of 1100°C the transition to α is found to be too short to measure. Yang *et al.* later established that the transition to α-alumina is nucleated at the metal-oxide interface and grows outward to consume existing θ-alumina [1.62].

1.3.2 Oxidation of MCrAlY alloys

As discussed in section 1.2.1, the Ni-Cr-Al system can serve as a basis for understanding behaviour of the MCrAlY system, and this is no less true in oxidation. In the presence of oxygen thermodynamics dictate that Ni-Cr-Al can form a number of possible oxides: NiO, Cr_2O_3, Al_2O_3 and Ni $(Cr, Al)_2O_4$ Spinels [1.56]. It is the variation in concentration and subsequent effect on kinetics that dictate which oxides will form under particular conditions, and are best described by oxide maps; the oxide map for Ni-Al-Cr is presented in Figure 1.10.

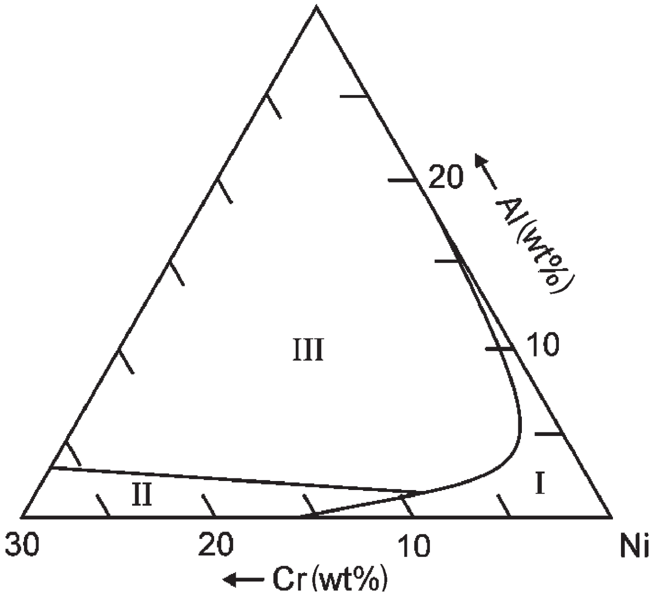

Figure 1.10: Oxide map for the Ni-Cr-Al system [1.56].

In this case three possible oxidation regions exist. At high Ni concentrations (Region I) NiO will form externally on the metal while a mix of Cr_2O_3, Al_2O_3 and Ni(Cr, Al)$_2$O$_4$ will form internally. At higher Cr concentrations (Region II) an external Cr_2O_3 scale is formed while Al_2O_3 develops internally. Finally throughout the broadest range of concentrations (Region III) only an external Al_2O_3 scale will form [1.56].

While the oxidation map in Figure 1.10 explains long-term oxidation behaviour, given that Ni-Cr-Al alloys have a two-phase structure consisting of one aluminum rich phase and one aluminum poor phase, there must be some variation in initial oxidation behaviour. This is most commonly described as the initial transient oxidation stage (similar to the transient metastable oxidation of aluminum described in the previous section) that occurs at the very beginning of oxidation [1.35]. In this stage the β-NiAl phase will form an alumina scale as described in the previous section, while the Ni and Cr-rich γ phase can form other oxide products including NiO, Cr_2O_3 and spinels [1.35]. Over time Al diffusion through the γ phase and surface growth on NiAl will allow the more stable alumina scale to develop under the transient oxides and become the dominant oxide forming [1.56]. Near the surface of the metal an aluminum-depleted zone will develop accordingly, marked by dissolution of the β phase near the interface [1.64]. After long periods the lack of aluminum in this depleted zone will limit the formation of new alumina and result in the oxidation of other species, yielding a second oxide layer that can again consist of NiO, Cr_2O_3 and spinels.

The oxidation of MCrAlY alloys such as NiCoCrAlY and CoNiCrAlY is very similar to that of Ni-Cr-Al, though the presence of alloying elements can modify this behaviour somewhat. Increased aluminum content increases the presence of β phase in the alloy and reduces the depletion zone while also encouraging the formation of alumina [1.4], while the addition of Co is know to stabilize the β-phase and similarly encourage alumina formation. Co base alloys have also been shown to form thicker transient scales of CoO and spinel [1.35] and lastly the addition of Y has been shown to have a positive effect on scale adhesion, being more relevant in the later stages of oxidation [1.34]. Increasing temperature has been shown to encourage the rapid formation of an alumina scale and supress the formation of other transient oxides [1.35], a similar effect has been found under reduced oxygen partial pressures [1.35, 1.65].

Numerous studies have explored the high temperature oxidation of MCrAlY alloys at different compositions. Studies by Unocic *et al.* [1.66], Belzunce *et al.* [1.67] and other researchers [1.65, 1.68, 1.69] have explored oxidation of NiCrAlY and consistently show the formation of a two-layer scale, the inner layer comprised of α-Al_20_3 and an outer layer that contains $NiAl_2O_4$ spinel and often Cr_2O_3. Investigations of CoNiCrAlY by Brandl *et al.* [1.70], Tang *et al.* [1.71] and others [1.72, 1.73] similarly reveal a two-layer oxide scale with an inner slow-growing alumina scale, though in this case Co-based spinels are often found and Cr_2O_3 has not been reported.

Studies of NiCoCrAlY have been somewhat more varied in their results. Studies by Nijdam *et al.* [1.74], Peng *et al.* [1.75], Mercer *et al.* [1.76] and Li *et al.* [1.77] have found a two-layer oxide with the expected inner layer of α-alumina and an outer layer of $NiAl_2O_4$ spinel. Brandl *et al.* [1.78] found similar Ni-based spinels along with Cr_2O_3 at lower temperatures (950°C) and Co-based spinels at higher temperatures (1050°C) in the outer layer. Interestingly, a second study by Brandl *et al.* [1.45] and a study by Subanovik *et al.* [1.79] found only a single layer of alumina formed on NiCoCrAlY which, given then protective nature of alumina, is the most desirable scenario. This was also observed by Mercier *et al.* [1.73] for polished CoNiCrAlY samples. Finally two of the most comprehensive studies on the oxidation behaviour of various MCrAlY alloys are comparative studies of multiple compositions by Brandl *et al.* [1.80] and Seo *et al.* [1.81]. In the former, NiCoCrAlY and CoNiCrAlY HVOF coatings both yielded a two-layer scale with an inner layer of alumina and an outer layer containing chromia. In the case of CoNiCrAlY the outer layer also contained CoO and in NiCoCrAlY the outer layer also contained Ni-base spinels. The latter study investigated long-term oxidation of NiCrAlY, NiCoCrAlY, CoCrAlY and CoNiCrAlY. In this case all samples formed an inner layer of α-alumina; the NiCrAlY and CoCrAlY samples formed outer layers of Cr_2O_3 as well as some NiO or CoO, this is expected given the consistency of results for NiCrAlY and long oxidation time. CoNiCrAlY was the best performing material and formed mostly alumina with a small amount of Co-based spinel. NiCoCrAlY formed alumina and an outer layer of Ni-based spinel. It is worth noting that several of these studies also detected residual θ-alumina in the oxide scale, indicative of the metastable oxide transformation during the early stages.

The relative variation of oxidation behaviour reported for NiCoCrAlY demonstrates the need for further study of this alloy under high temperature oxidizing conditions. Additionally, some results indicate the possibility of forming a single-layer corundum oxide scale or delaying the formation of a second layer, which could have interesting yields in terms of long-term oxidation resistance and component lifetime.

1.4 Nanomaterials

The concept of nanotechnology as a field of study began in 1959 with a speech by the Nobel Prize winning physicist Richard Feynman called “There’s plenty of room at the bottom” [1.82]. Despite only recent scientific interest, historical uses of nanomaterials are widespread, although tradesmen and artisans may not have known it at the time. Various types of metallic nanoparticles are responsible for the different colors in ancient stained glass windows, most notably the rose window of the Notre Dame Cathedral [1.83]. Many ancient pigments and paints are now known to contain nanoparticles, and the famous Damascus Steels are among the first carbon-based nanotechnologies [1.83].

From the perspective of material science and materials engineering, nanomaterials refer to any material whose features can be controlled on the nano scale (10^{-9} meters) [1.84]. More specifically, this generally refers to materials with a grain size on the order of 1 to 100 nm, though some consider the upper limit of what constitutes a nano grain to be as much as 500 nm [1.84]. These materials are characterized by extremely high surface area or grain boundary volume, which results in notably different properties when compared to conventional grain sized materials. The most well known of these differences is increased hardness; some researchers have found hardness of nanomaterials 2 to 7 times that of equivalent conventional materials [1.85, 1.86]. Other benefits include increased strength, particularly in the case of grapheme and carbon nanotubes [1.82] and a wide range of other properties.

Looking at nanostructure in the context of this thesis, grain refinement to the nano regime is believed to have a significant effect on the oxidation. In general, reduced grain size is associated with increased oxidation resistance [1.35]. Early work of chromia-forming stainless steels showed that increased grain boundary volume resulted in increased flux of Cr to the interface [1.35]. Additionally it has been shown that the process of nanostructuring also produces increased chemical homogeneity in alloys [1.87]. This in turn may reduce the transient formation of undesirable oxides in alloys like MCrAlY that have a seeding phase for the desirable oxide. Wang has also shown that the metastable formation of alumina, accelerated through certain dopants, can be equally accelerated through substrate nanostructure [1.88]. He has cited increased grain boundary area on the substrate surface as a key factor, providing more nucleation sites for α-alumina within the transient θ-alumina scale.

Within MCrAlY and related alloys, nanostructured coatings are thought to produce a more consistent and better-adhered alumina layer than their conventional counterparts. One of the first studies to propose this behaviour was on the simple Ni-Cr-Al system in 1998. Liu *et al.* studied a range of compositions for this ternary across a range of grain sizes [1.89]. They found that the minimum concentration required to form an alumina scale was drastically reduced at grain sizes below ~100 nm and plotted these results on a modified oxidation map presented here in Figure 1.11.

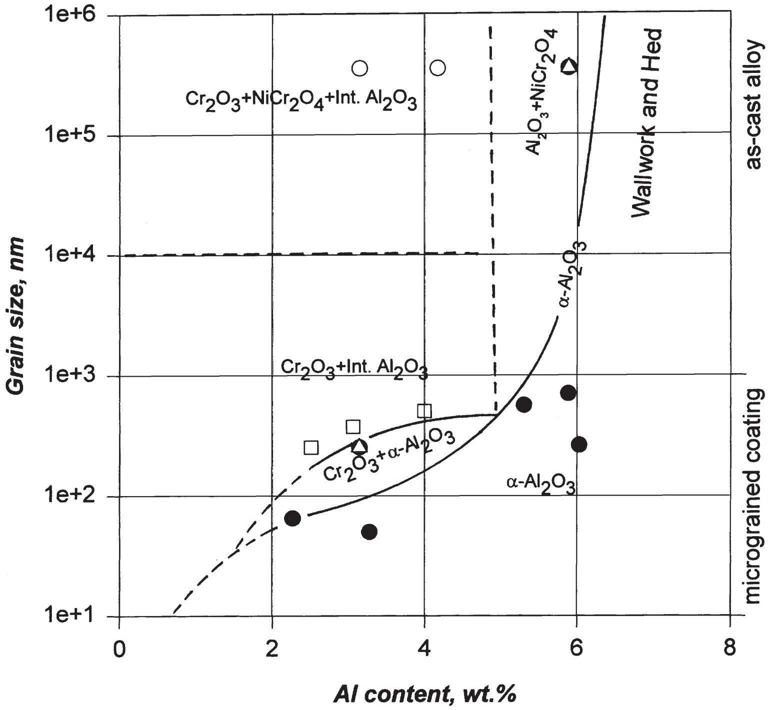

Figure 1.11: Oxides formed as a function of aluminum concentration and grain size in Ni-Cr-Al [1.89].

Several studies have examined the effect of nanostructure on NiCrAlY and CoCrAlY alloys. In the case of sputtered coatings [1.90, 1.91] the formation of an exclusive alumina layer was found, though after very long oxidation times at higher temperatures (1100°C) spinels may form [1.90]. In plasma sprayed [1.92] and HVOF sprayed [1.93] NiCrAlY a single alumina layer was found to form. This has been attributed to increased grain boundary area allowing for greater Al diffusion [1.93]. Unfortunately, these results are not consistent across the literature. For example Zhang *et al.* studied cold-sprayed nanostructured NiCrAlY coatings surface treated by shot peening. It was found similarly that the surface treated coating developed a dense single-layer oxide of α-Al_2O_3 while the non-surface treated (but still nanostructured) coating developed a layer of Al_2O_3 followed by a layer of Cr_2O_3 [1.94].

Similar inconsistencies exist in the study of nanostructured CoNiCrAlY. Todde *et al.* have studied SPS-consolidated nanostructured CoNiCrAlY and found that increased milling time yields increased grain refinement, which in turn supressed formation of the second spinel oxide layer [1.95]. Tang *et al.* studied HVOF-deposited nanostructured CoNiCrAlY and found that a single alumina layer formed up until all aluminum present in the coating had been consumed, at which point other oxides formed [1.96] They found that along with improved aluminum transport, milling led to the formation of small amounts of aluminum oxide within the cryomilled powder and subsequent coating. These oxides served as nucleation points for the formation of a denser alumina scale [1.96]. In contrast to these studies Mercier *et al.* [1.73] found that for HVOF-deposited nanostructured CoNiCrAlY an additional surface treatment was necessary to form a single-layer alumina scale, much like the work of Zhang *et al.* on NiCrAlY, though in this case grinding was used rather than shot peening. They found the formation of surface artefacts in spraying acted as seeds for the second spinel layer and effectively negated the benefits of nanostructure; the subsequent surface treatment eliminated said artefacts [1.73]. A second study by Tang *et al.* of HVOF-deposited nanostructured CoNiCrAlY supports the result found by Mercier *et al.* [1.71].

To date, only one study has been performed on nanostructured NiCoCrAlY, also by Mercier *et al.* [1.97] on cryomilled and HVOF deposited coatings. Similar to their CoNiCrAlY study, surface treatment was required in order to form a single alumina layer, untreated coatings (while still nanostructured) also formed an outer spinel layer. It is also worth noting that while several of the above-cited studies found the presence of the metastable θ-alumina [1.71, 1.73, 1.91, 1.96], there has been little discussion on the effect of nanostructure on the θ-α transition in MCrAlY alloys.

1.5 Fabrication techniques

Numerous fabrication techniques exist for the formation and consolidation of nanostructured powders and bulk nanomaterials. In general, two broad approaches exist, the bottom-up method and the top-down method. The bottom-up approach involves the synthesis of nanomaterials from nucleation at the atomic level, building up particles to reach the nanoscale, these methods include amorphous crystallization, electro-deposition and inert-gas condensation, among others [1.98]. The top-down approach involves the deformation of large materials to rearrange dislocations and create nano-scale grains within the larger particle or bulk, in essence “breaking-down” larger grains [1.99]. This approach includes severe plastic deformation and various types of mechanical milling.

1.5.1 Cryomilling

Cryomilling, or mechanical milling in a liquid nitrogen environment, is among the most well-known and commonly used methods for the synthesis of nanostructured powders [1.100]. It is a solid-state processing technique that involves continuous welding, fracture and re-welding of powder particles that results in refined grain size and well as decreased particle size [1.101-1.103]. As depicted in Figure 1.12, this grain refinement occurs through the formation of a high-density dislocation array in the material, which annihilate and recombine to form new grain boundaries. Once formed, grain boundary sliding allows for random grain orientation [1.101, 1.102, 1.104].

The addition of liquid nitrogen to the mill prevents oxidation of the powders during milling [1.100]. Additionally, milling in a cryogenic environment can increase fracture and recrystallization in the milled powder while also controlling powder temperature, as milling is a high-energy process that can be plagued by excess heating of the powders [1.104]. Lastly, in some cases the presence of liquid nitrogen can result in the formation of nitrides, which can aid in grain boundary pinning and increase the thermal stability of nanostructured powders [1.86].

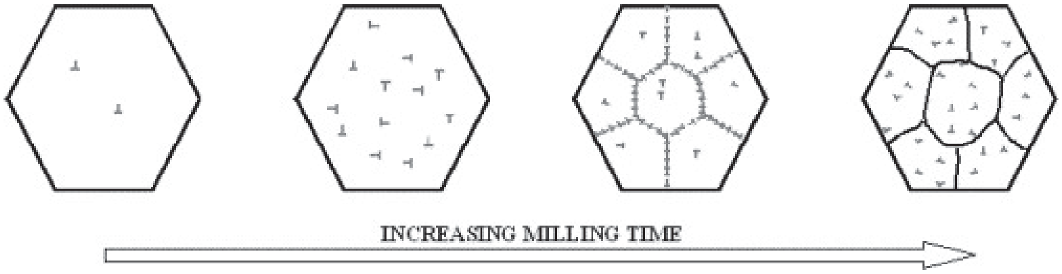

Figure 1.12: Stages of nanostructure formation in cryomilling [1.86].

1.5.2 Spark Plasma Sintering

Spark Plasma Sintering (SPS) is a powder consolidation process that can be used to preserve nanostructure [1.105]. It is a pressure assisted sintering technique that can offer notable advantages over other sintering methods. Powder is pressed in a graphite die through which a current is pulsed. As the powder bed conducts this current, contact points between particles are heated through the Joule process. This self-heating from within the powder bed can result in extremely high heating rates, on the order of 1000°C/min [1.105]. This can result in rapid sintering of the particles, yielding highly-dense, consolidated bulk materials [1.106]. Additionally, because SPS is performed under a vacuum, internal oxidation and other effects present in HVOF are negated. A schematic of the SPS process is presented in Figure 1.13.

It is believed that in the small gaps between powder particles in the SPS, spark discharges occur, which cause instantaneous melting and vaporization of the material, forming the plasma to which SPS owes its name. This vaporized material immediately cools and condenses to form necks between powder particles [1.105, 1.106, 1.108, 1.109]. Nonetheless, while this phenomenon is well cited, it has not been proven conclusively and some controversy exists as to the exact mechanism of neck formation in the SPS [1.110]. Research into the overall mechanism of densification in SPS is ongoing, though it is known that the combined effects of joule heating and applied pressure can activate mechanisms of plastic flow, creep and electromigration [1.110] which can also contribute to densification and consolidation of the sintered powder.

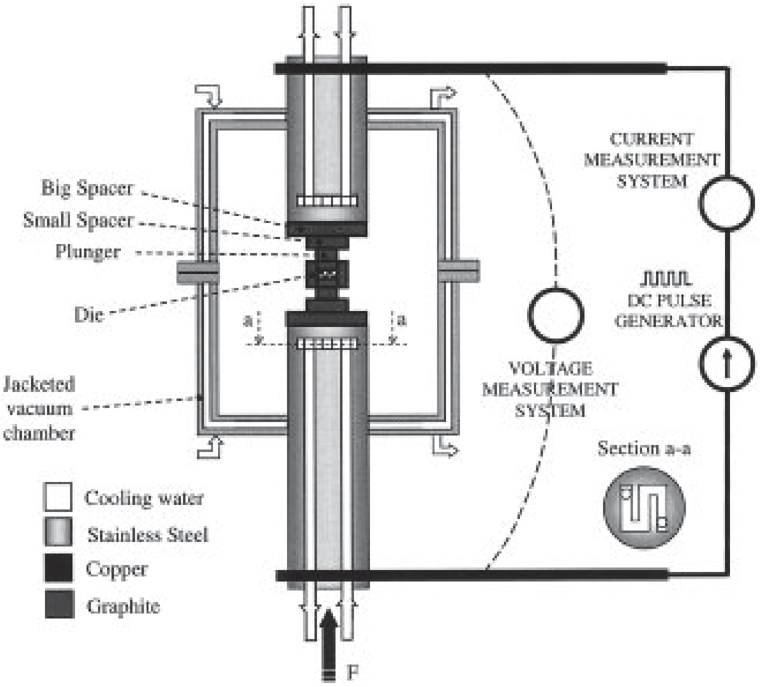

Figure 1.13: A schematic of the Spark Plasma Sintering process [1.107].

To date, a small number of studies have explored the consolidation of NiAl powders via SPS. Yin *et al.* have used SPS to successfully consolidate dense NiAl intermetallic rods for a hot corrosion study [1.111] and Anderson *et al.* conducted a TEM study of SPS-consolidated NiAl and found that a small amount of alumina formed at grain boundaries during sintering [1.112]. Two recent studies have also investigated

$NiAl/Al_2O_3$ composites consolidated by SPS and have noted vastly increased mechanical properties in the composite samples [1.113, 1.114].

A similarly small number of studies have used SPS to consolidate MCrAlY powders. Song *et al.* have consolidated NiCrAlY powders and subjected the consolidated samples to an extensive series of heat treatments, finding significant microstructural changes after heat treatment [1.115]. Oquab *et al.* have successfully fabricated dense NiCoCrAlY coatings and found good high temperature oxidation performance [1.116]. Todde *et al.* have been the first to consolidate grain refined MCrAlY alloys, in a study of the oxidation performance of cryomilled and SPS-consolidated CoNiCrAlY powders [1.95]. The samples remained in the ultrafine regime after SPS consolidation. Song *et al.* [1.117] and Boidot *et al.* [1.118] have also used spark plasma sintering to direct-consolidate full multi-layer thermal barrier coatings and have identified SPS as an interesting and rapid method of fabricating complex, multi-layer coating systems. Perhaps the most extensive study to date was conducted by Monceau *et al.* [1.119] who have consolidated a wide range of materials by SPS, including numerous Pt-Al based systems, NiAl and several MCrAlY compositions. They have also proposed SPS as a method to direct-sinter complex multi-layered systems.

1.5.3 High-Velocity Oxy-Fuel Spray

HVOF is one of many thermal spray techniques that can be used to deposit MCrAlY coatings [1.120]. A mixture of fuel and air or oxygen is combusted and the hot gas forced through a converging-diverging nozzle to reach gas velocities in the supersonic range. The powder feedstock is injected into the high velocity gas flow and subsequently heated and accelerated to impact the substrate [1.121]. Particle velocities greater than 1000 m/s are obtainable, substantially higher than many other spray techniques. On impact, the partially melted particles form thin “splats” that rapidly cool and solidify, forming the coating [1.121]. Figure 1.14 shows a typical HVOF setup using acetylene as fuel.

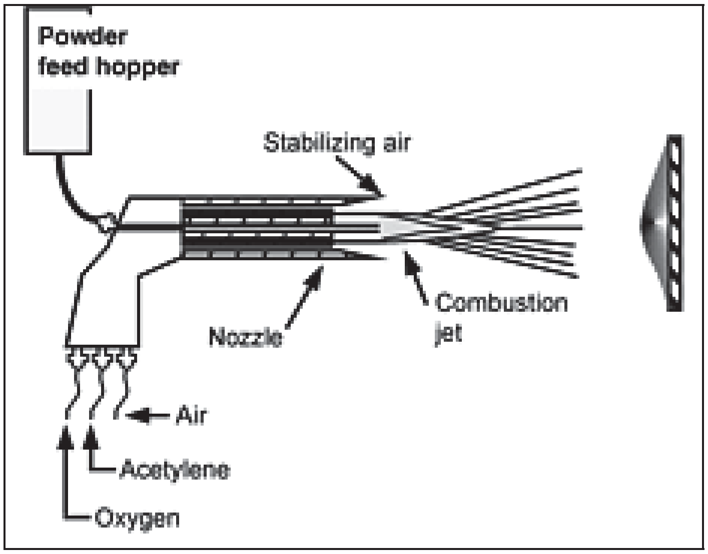

Figure 1.14: A typical HVOF spray gun [1.121].

Numerous studies of MCrAlY alloys employ HVOF as a deposition method [1.72, 1.122-1.124] and have noted the formation of oxide dispersions, normally alumina, within the deposited coating and is generally perceived as a beneficial effect. The most extensive work in this regard has been the work of Brandl *et al.* [1.45, 1.70, 1.78] who have identified the oxide dispersion formed during thermal-spray as a primary reason for the improved oxidation performance of HVOF MCrAlY coatings when compared to Plasma-Spray. All of the studies cited have used conventional grain sized powders and subjected the subsequent coatings to heat treatment steps, and several note that surface modification can also be beneficial to oxidation rate [1.70, 1.78]. In contrast to these studies, several have found the oxide dispersions during HVOF to be detrimental to oxidation performance [1.64, 1.71, 1.73, 1.97, 1.125-1.127]. Zhao *et al.* and Li *et al.* have both noted internal oxidation of deposited coatings can be attributed to in-flight oxidation [1.126, 1.127] and they, along with Mori *et al.* found that minimizing oxygen pick-up in flight will yield better oxidation performance [1.64]. Tang *et al.*, Ni *et al.* and two studies by Mercier *et al.* [1.71, 1.73, 1.97, 1.125] came to similar conclusions about in-flight oxidation, but focused on post-spraying treatment to remove some of the artefacts created during spraying, in turn yielding better oxidation performance.

Due to only partial melting and rapid cooling of particles on impact, HVOF has been proven to preserve nanostructure in coatings deposited from nanostructured feedstock. Several studies of nanostructured or ultrafine MCrAlY alloys deposited by HVOF have shown that grain size was maintained, or only partially altered within the coating. [1.71, 1.73, 1.96, 1.97] This being said, in almost all of these studies, in-flight or on-impact oxidation has been detrimental to oxidation performance. In these cases it was found that as-sprayed nanostructured coatings formed a two-layer oxide scale, while samples subjected to surface grinding, post-spraying, formed the desired single layer of alumina and demonstrated accordingly lower oxidation rates.

1.6 References

[1.1] G. H. Koch, M. P. H. Brongers, N. G. Thomson, P. Virmani, J. H. Payer, *Corrosion Costs and Preventive Strategies in the USA*, Report FHWA-RD-01-156 to Federal Highways Administration, C. C. Technologies Laboratories, 2001.

[1.2] J. A. Richardson, J. L. Dawson, *Economic Aspects of Corrosion* in: Shrier's Corrosion, Elsevier, Oxford, 2010, 3040-3051.

[1.3] A. S. Khanna, *High Temperature Oxidation* in: Handbook of Environmental Degradation of Materials, Elsevier, 2002.

[1.4] S. Bose, *High Temperature Coatings*, Buttersworth Heinemann, Burlington, 2007.

[1.5] C. J. E. Smith, *Management of Corrosion of Aircraft* in: Shrier's Corrosion, Elsevier, Oxford, 2010, 3175-3197.

[1.6] R. Terms, A. M. Al Zahrani, *Cost of corrosion in oil production and* refining, Saudi Aramco Journal of Technology, Summer (2006) 2-14.

[1.7] J. L. Dawson, G. John and K. Oliver, *Management of Corrosion in the Oil and Gas Industry* in: Shrier's Corrosion, Elsevier, Oxford, 2010, 3230-3269.

[1.8] B. A. Pint, J. R. DiStefano, I. G. Wright, *Oxidation resistance: One barrier to moving beyond Ni-base superalloys*, Materials Science and Engineering A 415 (2006) 255–263.

[1.9] G. W. Meetham, M. H. Van de Voorde, *Nickel Alloys* in: Materials for High Temperature Engineering Applications, Springer, 2000, 68-82.

[1.10] N. S. Stoloff, *Wrought and P/M Superalloys – Nickel Alloys* in: ASM Handbook, Volume 1, ASM Handbook Comittee, Pittsburgh, 2004, 2301 – 2344.

[1.11] M. McLean, *Nickel-base superalloys: current status and potential* in: High-Temperature Structural Materials, Springer, 1996, 1-13.

[1.12] D. B. Miracle, R. Darolia, *NiAl and its Alloys* in: Structural Applications of Intermetallic Compounds, John Wiley and Sons, 2000, 55-74.

[1.13] N. Cinca, J. M. Guilemany, *Thermal spraying of transition metal aluminides: An overview*, Intermetallics 24 (2012) 60-72.

[1.14] R. Darolia, D. F Lahrman, R. D. Field, J. R. Dobbs, K. M. Chang, E. H. Goldman, D. G. Konitzer, *Overview of NiAl Alloys for High Temperature Structural Applications* in: Ordered Intermetallics – Physical Metallurgy and Mechanical Behaviour, Springer, 1992, 679-698.

[1.15] R. D. Noebe, R. R. Bowman, M. V. Nathal, *The Physical and Mechanical Metallurgy of NiAl* in: Physical Metallurgy and Processing of Intermetallic Compounds, Chapman and Hall, 1996, p. 212-296.

[1.16] G. W. Goward, Journal of Metals 22 (1970) 31-39.

[1.17] J. L. Smialek, G. H. Meier, *High Temperature Oxidation* in Superalloys II, John Wiley and Sons, New York, 1987, 293-326.

[1.18] D. Miracle, *Overview No. 104 The physical and mechanical properties of NiAl*, Acta Metallurgica et Materialia 41 (1993) 649-684.

[1.19] Z. G. Liu, J. T. Guo, L. L. He, Z. Q. Hu, *Formation of B2 intermetallic NiAl and FeAl by mechanical alloying*, Nanostructured Materials 4 (1994) 787-794.

[1.20] W. Hu, M. Li, M. Fukumoto, *Preparation and properties of HVOF NiAl nanostructured coatings*, Materials Science and Engineering A 478 (2008) 1-8.

[1.21] M.H. Enayati, F. Karimzadeh, S.Z. Anvari, *Synthesis of nanocrystalline NiAl by mechanical alloying*, Journal of Materials Processing Technology 200 (2008) 312-315.

[1.22] E.T. Kubaski, O.M. Cintho, J.L. Antoniassi, H. Kahn, J.D.T. Capocchi, *Obtaining NiAl intermetallic compound using different milling devices*, Advanced Powder Technology 23 (2012) 667-672.

[1.23] J. Joardar, S. K. Pabi, H.-J. Fecht, B. S. Murty, *Stability of nanocrystalline disordered NiAl synthesized by mechanical alloying*, Philosophical Magazine Letters 82 (2002) 469-475.

[1.24] J. Joardar, S.K. Pabi and B.S. Murty, *Milling criteria for the synthesis of nanocrystalline NiAl by mechanical alloying*, Journal of Alloys and Compounds, Volume 429, Issues 1–2, 21 February 2007, Pages 204-210.

[1.25] G.H. Xu, K.F. Zhang, Z.Q. Huang, *The synthesis and characterization of ultrafine grain NiAl intermetallic*, Advanced Powder Technology, Volume 23, Issue 3, May 2012, Pages 366-371.

[1.26] H.J. Choi, J. Jedlinski, B. Yao, Y.H. Sohn, *Transmission electron microscopy observations on the phase composition and microstructure of the oxidation scale grown on as-polished and yttrium-implanted β-NiAl*, Surface and Coatings Technology 205 (2010) 1206-1210.

[1.27] H. Svensson, M. Christensen, P. Knutsson, G. Wahnström, K. Stiller, *Influence of Pt on the metal–oxide interface during high temperature oxidation of NiAl bulk materials*, Corrosion Science 51 (2009) 539-546.

[1.28] K. M. Carling, A. M. Carter, *Effects of segregating elements on the adhesive strength and structure of the α-Al2O3/β-NiAl interface,* Acta Materialia 55 (2007) 2791-2803.

[1.29] M.A. Bestor, J.P. Alfano, M.L. Weaver, *Influences of chromium and hafnium additions on the microstructures of β-NiAl coatings on superalloy substrates*, Intermetallics 19 (2011) 1693-1704.

[1.30] D. Li, H. Guo, H. Peng, S. Gong, H. Xu *Improved alumina scale adhesion of electron beam physical vapour deposited Dy/Hf-doped β-NiAl coatings*, Applied Surface Science 283 (2013) 513-520.

[1.31] X. Zhao, H. Guo, Y. Gao, S. Wang, S. Gong, *Effects of Dy on Transient Oxidation Behaviour of EB-PVD β-NiAl Coatings at Elevated Temperatures*, Chinese Journal of Aeronautics 24 (2011) 363-368.

[1.32] L. Wang, D. Li, J. Chang, H. Guo, S. Gong, H. Xu, *Isothermal Oxidation Behaviour of Dysprosium/S-Doped b-NiAl Alloys at 1200°C*, Journal of Materials Science and Technology, in press, corrected proof, Aug 2013.

[1.33] Pint et al, M. Treska, L. W. Hobbs, *The Effect of Various Oxide Dispersions on the Phase Composition and Morphology of* $A1_2O_3$ *Scales Grown on β-NiAl*, Oxidation of Metals 47 (1992) 1-20.

[1.34] G. W. Meetham, M. H. Van de Voorde, *Coatings for High Temperature Materials* in: Materials for High Temperature Engineering Applications, Springer, 2000, 140-147.

[1.35] B.A. Pint, *High Temperature Corrosion of Alumina-forming Iron, Nickel and Cobalt-base Alloys* in: Shrier's Corrosion, Elsevier, Oxford, 2010, 606-645.

[1.36] B. Baufeld, M. Bartsch, P. Broz, M. Schmucker, *Microstructural changes as postmortem temperature indicator in Ni–Co–Cr–Al–Y oxidation protection coatings*, Materials Science and Engineering A 384 (2004) 162-171.

[1.37] J. J. Liang, H. Wei, Y.L. Zhu, X.F. Sun, T. Jin, Z.Q. Hu, M.S. Dargusch, X. Yao*, Influence of Co addition on constituent phases and performance of a NiCrAlYRe alloy system*, Surface and Coatings Technology 205 (2011) 4968-4979.

[1.38] J. Bursík, P. Broz, J. Popovic, *Microstructure and phase equilibria in Ni‑Al‑Cr‑Co alloys*, Intermetallics 14 (2006) 1257-1261.

[1.39] A. Hesnawi, H. Li, Z. Zhou, S. Gong, H. Xu, *Isothermal oxidation behaviour of EB-PVD MCrAlY bond coat*, Vacuum 81 (2007) 947-952.

[1.40] T. J. Nijdam, W. G. Sloof, *Microstructural evolution of a MCrAlY coating upon isothermal annealing*, Materials Characterization 59 (2008) 1697-1704.

[1.41] A. Weisenburger, G. Rizzi, A. Scrivani, G. Mueller, J. R. Nicholls, *Pulsed electron beam treatment of MCrAlY bondcoats for EB-PVD TBC systems part 1 of 2: Coating production*, Surface and Coatings Technology 202 (2007) 704-708.

[1.42] J. He, H. Guo, H. Peng, S. Gong, *Microstructural, mechanical and oxidation features of NiCoCrAlY coating produced by plasma activated EB-PVD*, Applied Surface Science 274 (2013) 144-150.

[1.43] P. Song, D. Naumenko, R. Vassen, L. Singheiser, W. J. Quadakkers, *Effect of oxygen content in NiCoCrAlY bondcoat on the lifetimes of EB-PVD and APS thermal barrier coatings*, Surface and Coatings Technology 221 (2013) 207-213.

[1.44] K. J. Hemker, B. G. Mendis, C. Eberl, *Characterizing the microstructure and mechanical behavior of a two-phase NiCoCrAlY bond coat for thermal barrier systems*, Materials Science and Engineering A 483-484 (2008) 727-730.

[1.45] W. Brandl, D. Toma, H. J. Grabke, *The characteristics of alumina scales formed on HVOF-sprayed MCrAlY coatings*, Surface and Coatings Technology 108-109 (1998) 10-15.

[1.46] E. Lugscheider, C. Herbst, L. Zhao, *Parameter studies on high-velocity oxy-fuel spraying of MCrAlY coatings*, Surface and Coatings Technology 108–109 (1998) 16-23.

[1.47] Li, C. Langlade, S. Fayeulle, D. Tréheux, *Influence of the microstructure of plasma deposited MCrAlY coatings on their tribological behaviour*, Surface and Coatings Technology 100–101 (1998) 7-11.

[1.48] U. Bardi, L. Carrafiello, R. Groppetti, F. Niccolai, G. Rizzi, A. Scrivani, F. Tedeschi, *On the surface preparation of nickel superalloys before CoNiCrAlY deposition by thermal spray*, Surface and Coatings Technology 184 (2004) 156-162.

[1.49] S.-W. Myoung, S.-H. Park, P.-H. Lee, Y.-G. Jung, D. Joo, K.-H. Lee, H.-S. Lee, U. Paik, *Phase transformation and oxidation behavior of Pt-modified MCrAlY coatings*, Progress in Organic Coatings 61 (2008) 316-320.

[1.50] Y. Li, C.-J. Li, G.-J. Yang, L.-K. Xing, *Thermal fatigue behavior of thermal barrier coatings with the MCrAlY bond coats by cold spraying and low-pressure plasma spraying*, Surface and Coatings Technology 205 (2010) 2225-2233.

[1.51] I. Keller, D. Naumenko, W.J. Quadakkers, R. Vaßen, L. Singheiser, *Influence of vacuum heat treatment parameters on the surface composition of MCrAlY coatings*, Surface and Coatings Technology 215 (2013) 24-29.

[1.52] D.R.G. Achar, R. Munoz-Arroyo, L. Singheiser, W.J. Quadakkers, *Modelling of phase equilibria in MCrAlY coating systems*, Surface and Coatings Technology 187 (2004) 272-283.

[1.53] B.G. Mendis, K.J. Hemker, *Thermal stability of microstructural phases in commercial NiCoCrAlY bond coats*, Scripta Materialia 58 (2008) 255-258.

[1.54] J.J. Liang, H. Wei, Y.L. Zhu, T. Jin, X.F. Sun, Z.Q. Hu, *Phase stabilities in a NiCrAlYRe coating alloy*, Surface and Coatings Technology 206 (2012) 2746-2750.

[1.55] K. Ma, J. M. Schoenung, *Thermodynamic investigation into the equilibrium phases in the NiCoCrAl system at elevated temperatures*, Surface and Coatings Technology 205 (2010) 2273-2280.

[1.56] N. Birks, G. H. Meier, F. S. Pettit, *Introduction to the high temperature of metals*, 2nd edition, Cambridge University Press, Cambridge, 2006.

[1.57] S. Chevalier, *Mechanisms and Kinetics of Oxidation* in: Shrier's Corrosion, Elsevier, Oxford, 2010, 132-152.

[1.58] B. Pierragi, Defects and Transport in Oxide Scales in: Shrier's Corrosion, Elsevier, Oxford, 2010, 101-131.

[1.59] B. Pierragi, *Calculations of parabolic reaction rate constants*, Oxidation of Metals 27 (1987) 177-185.

[1.60] M. W. Brumm, H. J. Grabke, *The oxidation behaviour of NiAl - I. Phase transformations in the alumina scale during oxidation of NiAl and NiAl-Cr alloys*, Corrosion Science 33 (1992) 1677-1690.

[1.61] H. J. Grabke, *Oxidation of NiAl and FeAl*, Intermetallics 7 (1999) 1153-1158.

[1.62] J. C. Yang, E. Schumann, I. Levin, M. Ruhle, *Transient Oxidation of NiAl*, Acta Materialia 46 (1998) 2195-2201.

[1.63] K. Wefers, C. Misra, *Oxides and Hydroxides of Aluminum*, Alcoa Technical paper, 1987.

[1.64] T. Mori, S. Kuroda, H. Murakami, H. Katanoda, Y. Sakamoto, S. Newman*, Effects of initial oxidation on β phase depletion and oxidation of CoNiCrAlY bond coatings fabricated by warm spray and HVOF processes*, Surface and Coatings Technology 221 (2013) 59-69.

[1.65] C. G. Levi, E. Sommer, S. G. Terry, A. Catanoiu, M. Rühle, *Alumina grown during deposition of thermal barrier coatings on NiCrAlY*, Journal of the American Ceramic Society 86 (2003) 676-685.

[1.66] K. A. Unocic, B. A. Pint, *Oxidation behavior of co-doped NiCrAl alloys in dry and wet air,* Surface and Coatings Technology 237 (2013) 8-15.

[1.67] F.J Belzunce, V Higuera, S Poveda, *High temperature oxidation of HFPD thermal-sprayed MCrAlY coatings,* Materials Science and Engineering A 297 (2001) 162-167.

[1.68] C. Zhu, P. Li, A. Javed, G.Y. Liang, P. Xiao, *An investigation on the microstructure and oxidation behavior of laser remelted air plasma sprayed thermal barrier coatings*, Surface and Coatings Technology 206 (2012) 3739-3746.

[1.69] H. Choi, B. Yoon, H. Kim, C. Lee, *Isothermal Oxidation of air plasma spray NiCrAlY bond coatings*, Surface and Coatings Technology 150 (2002) 297-308.

[1.70] W. Brandl, G. Marginean, D. Maghet, D. Utu, *Effects of specimen treatment and surface preparation on the isothermal oxidation behaviour of the HVOF-sprayed MCrAlY coatings,* Surface and Coatings Technology 188-189 (2004) 20-26.

[1.71] F. Tang, L. Ajdelsztajn, G. E. Kim, V. Provenzano, J. M. Schoenung, *Effects of surface oxidation during HVOF processing on the primary stage oxidation of a CoNiCrAlY coating*, Surface and Coatings Technology 185 (2004) 228-233.

[1.72] S. Saeidi, K. T. Voisey, D. G. McCartney, *The effect of heat treatment on the oxidation behavior of HVOF and VPS CoNiCrAlY coatings*, Journal of Thermal Spray Technology 18 (2009) 209-216.

[1.73] D. Mercier, C. Kaplin, G. Goodall, G. Kim, M. Brochu, *Parameters influencing the oxidation behavior of cryomilled CoNiCrAlY*, Surface and Coatings Technology 205 (2010) 2546-2553.

[1.74] T.J. Nijdam, W.G. Sloof, *Combined pre-annealing and pre-oxidation treatment for the processing of thermal barrier coatings on NiCoCrAlY bond coatings*, Surface and Coatings Technology 201 (2006) 3894-3900.

[1.75] H. Peng, H. Guo, J. He, S. Gong, *Oxidation and diffusion barrier behaviours of double-layer NiCoCrAlY coatings produced by plasma activated EB-PVD*, Surface and Coatings Technology 205 (2011) 4658-4664.

[1.76] C. Mercer, K. Kawagishi, T. Tomimatsu, D. Hovis, T.M. Pollock, *A comparative investigation of oxide formation on EQ (Equilibrium) and NiCoCrAlY bond coats under stepped thermal cycling*, Surface and Coatings Technology 205 (2011) 3066-3072.

[1.77] Z. Li, S. Qian, W. Wang, *Characterization and oxidation behaviour of NiCoCrAlY coating fabricated by electrophoretic deposition and vacuum heat treatment*, Applied Surface Science 257 (2011) 4616-4620.

[1.78] W. Brandl, D. Toma, J. Krüger, H.J. Grabke, G. Matthäus, *The oxidation behaviour of HVOF thermal-sprayed MCrAlY coatings,* Surface and Coatings Technology 94-95 (1997) 21-26.

[1.79] M. Subanovic, P. Song, E. Wessel, R. Vassen, D. Naumenko, L. Singheiser, W.J. Quadakkers, *Effect of exposure conditions on the oxidation of MCrAlY-bondcoats and lifetime of thermal barrier coatings*, Surface and Coatings Technology 204 (2009) 820-823.

[1.80] W. Brandl, H.J. Grabke, D. Toma, J. Krüger, *The oxidation behaviour of sprayed MCrAIY coatings*, Surface and Coatings Technology 86-87 (1996) 41-47.

[1.81] D. Seo, K. Ogawa, Y. Suzuki, K. Ichimura, T. Shoji, S. Murata, *Comparative study on oxidation behavior of selected MCrAlY coatings by elemental concentration profile analysis,* Applied Surface Science 255 (2008) 2581-2590.

[1.82] L. Williams, W. Adams, *Nanotechnology Demystified*, McGraw Hill, Ney York, 2007.

[1.83] R. Vajtai, *Science and engineering of nanomaterials* in: Springer Handbook of Nanomaterials, Springer, Dordrecht, 2013, 1-38.

[1.84] K. T. Ramesh, *Nanomaterials: Mechanics and Mechanisms*, Springer, Dordrecht, 2009.

[1.85] E. Bonetti, L. Pasquini, E. Sampaolesi, *The influence of grain size on the mechanical properties of nanocrystalline aluminum,* Nanostructured Materials 9 (1997) 611-614.

[1.86] D. B. Witkin, E.J. Lavernia, *Synthesis and mechanical behavior of nanostructured materials via cryomilling,* Progress in Materials Science 51 (2006) 1-60.

[1.87] H. Habazaki, *Corrosion of Amorphous and Nanograined Alloys* in: Shrier's Corrosion, Elsevier, Oxford, 2010, 2192-2204.

[1.88] F. Wang, *The Effect of Nanocrystallization on the Selective Oxidation and Adhesion of* Al_2O_3 *Scales*, Oxidation of Metals 48 (1997) 215-224.

[1.89] Z. Liu, W. Gao, K. L. Dahm, F. Wang, *Oxidation behaviour of sputter-deposited Ni‑Cr‑Al micro-crystalline coatings,* Acta Materialia 46 (1998) 1691-1700.

[1.90] X. Ren, F. Wang, *High-temperature oxidation and hot-corrosion behavior of a sputtered NiCrAlY coating with and without aluminizing*, Surface and Coatings Technology 201 (1006) 30-37.

[1.91] G.-M. Liu, M.-S. Li, J.-H. Ma, N. Du, Y.-C. Zhou, *Transient oxidation behavior of nanocrystalline CoCrAlY coating at 1 050 °C.* Transactions of Nonferrous Metals Society of China 17 (2007) 595-599.

[1.92] M. Daroonparvar, M. A. Mat Yajid, N. M. Yusof, M. S. Hussain, H. R. Bakhsheshi-Rad, *Formation of a dense and continuous* Al_2O_3 *layer in nano thermal barrier coating systems for the suppression of spinel growth on the* Al_2O_3 *oxide scale during oxidation*, Journal of Alloys and Compounds 571 (2013) 205-220.

[1.93] L. Ajdelsztajn, J. A. Picas, G. E. Kim, F. L. Bastian, J. Schoenung, V. Provenzano, *Oxidation behavior of HVOF sprayed nanocrystalline NiCrAlY powder*, Materials Science and Engineering A 338 (2002) 33-43.

[1.94] Q. Zhang, C.-J. Li, C.-X. Li, G.-J. Yang, S.-C. Lui, *Study of oxidation behavior of nanostructured NiCrAlY bond coatings deposited by cold spraying*, Surface and Coatings Technology 202 (2008) 3378-3384.

[1.95] S. Todde, R. Licheri, R. Orru, G. Cao, *Spark plasma sintering processing for the evaluation of cryomilled CoNiCrAlY alloys for high temperature applications in oxidizing environment,* Chemical Engineering Journal 200-202 (2012) 68-80.

[1.96] F. Tang, L. Ajdelsztajn, J.M. Schoenung, *Influence of Cryomilling on the Morphology and Composition of the Oxide Scales Formed on HVOF CoNiCrAlY Coatings*, Oxidation of Metals 61 (2004) 219-238.

[1.97] D. Mercier, B. D. Gauntt, M. Brochu, *Thermal stability and oxidation behavior of* *nanostructured NiCoCrAlY coatings*, Surface and Coatings Technology 205 (2011) 4162-4168.

[1.98] H. Gleiter, *Nanostructured materials: basic concepts and microstructure,* Acta Materialia 48 (2000) 1-29.

[1.99] H. Gleiter, *Nanocrystalline materials,* Progress in Materials Science 33 (1989) 223-315.

[1.100] J. He, J. M. Schoenung, *Review: Nanostructured Coatings*, Materials Science and Engineering A 336 (2002) 274-319.

[1.101] H. J. Fecht, *Nanostructure formation by mechanical attrition,* Nanostructured Materials 6 (1995) 33-42.

[1.102] C. C. Koch, *Top-Down Synthesis of Nanostructured Materials: Mechanical and Thermal Processing Methods,* Review on Advanced Materials Science 5 (2003) 91-99.

[1.103] E. J. Lavernia, B.Q. Han, J.M. Schoenung, *Cryomilled nanostructured materials: Processing and properties,* Materials Science and Engineering A 493 (2008) 207-214.

[1.104] C. Suryanarayana, *Mechanical alloying and milling,* Progress in Materials Science 46 (2001) 1-184.

[1.105] J. C. Ye, L. Ajdelsztajn, J. M. Schoenung, *Bulk Nanocrystalline Aluminum 5083 Alloy Fabricated by a Novel Technique: Cryomilling and Spark Plasma Sintering*, Metallurgical and Materials Transactions 37A (2006) 2569-2579.

[1.106] M. Tokita, *Mechanism of Spark Plasma Sintering (SPS),* in: Sumitomo Coal Mining Company, Ltd., Japan.

[1.107] A. Cincotti, A. M. Locci, R. Orrù, G. Cao, *Modeling of SPS Apparatus: Temperature, Current and Strain Distribution with No Powders,* AIChE Journal 53 (2007) 703-719.

[1.108] W. Chen, U. Anselmi-Tamburini, J.E. Garay, J.R. Groza, Z.A. Munir*, Fundamental investigations on the spark plasma sintering/synthesis process: I. Effect of dc pulsing on reactivity,* Materials Science and Engineering A 294 (2005) 132-138.

[1.109] M. Kubota, B.P. Wynne, *Electron backscattering diffraction analysis of mechanically milled and spark plasma sintered pure aluminum,* Scripta Materialia 57 (2007) 719-722.

[1.110] J. Milligan, PhD Thesis: *Surface Modification of Heat Treatable Al Components Using Cryomilled and Rapidly Solidified Al-Si,* McGill University, Montreal, 2013.

[1.111] H. Yin, T. Yu, D. Tang, X. Ruan, H. Zhu, D. Wang, *Electrochemical preparation of NiAl intermetallic compound from solid oxides in molten $CaCl_2$ and its corrosion behaviors in NaCl aqueous solution*, Materials Chemistry and Physics 133 (2013) 465-479.

[1.112] K.R Anderson, J.R Groza, M Fendorf, C.J Echer, *Surface oxide debonding in field assisted powder sintering,* Materials Science and Engineering A 270 (1999) 278-282.

[1.113] A. Michalski, J. Jaroszewicz, M. Rosiński, D. Siemiaszko, *NiAl–Al_2O_3 composites produced by pulse plasma sintering with the participation of the SHS* *reaction,* Intermetallics 14 (2006) 603-606.

[1.114] V. Udhayabanu, K.R. Ravi, B.S. Murty, *Ultrafine-grained, high-strength NiAl with* Al_2O_3 *and* Al_4C_3 *nanosized particles dispersed via mechanical alloying in toluene with spark plasma sintering,* Materials Science and Engineering A 585 (2013) 379-386.

[1.115] J. Song, K. Ma, Y. Li, L. Zhang, J. M. Schoenung, *High temperature microstructure and microhardness evolution in dense NiCrAlY bulk material fabricated by spark plasma sintering*, Materials Science and Engineering A 528 (2011) 3210-3217.

[1.116] D. Oquab, C. Estournès, D. Monceau, *Oxidation Resistant Aluminized MCrAlY Coating Prepared by Spark Plasma Sintering (SPS),* Advanced Engineering Materials 9 (2007) 413-417.

[1.117] J. Song, K. Ma, L. Zhang, J. M. Schoenung, *Simultaneous synthesis by spark plasma sintering of a thermal barrier coating system with a NiCrAlY bond coat,* Surface and Coatings Technology 205 (2010) 1241-1244.

[1.118] M. Boidot, S. Selezneff, D. Monceau, D. Oquab, C. Estournès, *Proto-TGO formation in TBC systems fabricated by Spark Plasma Sintering,* Surface and Coatings Technology 205 (2010) 1245-1249.

[1.119] D. Monceau, D. Oquab, C. Estournès, M. Boidot, S. Selezneff, Y. Thebault, Y. Cadoret, Pt-modified Ni aluminides, *MCrAlY-base multilayer coatings and TBC systems fabricated by Spark Plasma Sintering for the protection of Ni-base superalloys*, Surface and Coatings Technology 204 (2009) 771-778.

[1.120] M. R. Dorfman, *Thermal Spray Coatings* in: Handbook of Environmental Degradation of Materials, Elsevier, Oxford, 2012, 569-596.

[1.121] R. Knight, R. Smith, *Thermal Spray Forming of Materials* in: ASM Handbook, Volume 7: Powder Metal Technologies and Applications, ASM Handbook Comittee, Pittsburgh, 1998, 957-963.

[1.122] B.A. Pint, M.A. Bestor, J.A. Haynes, *Cyclic Oxidation Behavior of HVOF Bond Coatings Deposited on La- and Y-doped Superalloys,* Surface and Coatings Technology 206 (2011) 1600-1604.

[1.123] M. Mohammadi, S. Javadpour, S.A.J. Jahromi, K. Shirvani, A. Kobayashi, *Characterization and hot corrosion performance of LVPS and HVOF-CoNiCrAlYSi coatings,* Vacuum 86 (2012) 1458-1464.

[1.124] G. Marginean, D. Utu, *Cyclic oxidation behaviour of different treated CoNiCrAlY coatings,* Applied Surface Science 258 (2012) 8307-8311.

[1.125] L.-Y.Ni, Z.-L.Wu, C.-G. Zhou, *Effects of surface modification on isothermal oxidation behaviour of HVOF-sprayed NiCrAlY coatings*, Progress in Natural Science: Materials International 21 (2011) 173-179.

[1.126] C.-J. Li, W.-Y. Li, *Effect of sprayed powder particle size on the oxidation behavior of MCrAlY materials during high velocity oxygen-fuel deposition*, Surface and Coatings Technology 162 (2003) 31-41.

[1.127] L. Zhao, M. Parco, E. Lugscheider, *High velocity oxy-fuel thermal spraying of a NiCoCrAlY alloy*, Surface and Coatings Technology 179 (2004) 272-278.

Chapter 2: Research Objectives

The primary focus of this thesis is to study the potential improvement of high temperature oxidation and corrosion performance of MCrAlY and related alloys through nanostructuring, from understanding the oxidation mechanism of grain refined materials to evaluation of their performance in a simulated service environment. Grain refinement of the metal substrate was shown to favour the formation of a single oxide layer of α-alumina that can prevent the formation of fast growing spinel oxides. Consequently lower overall oxidation rates are expected, offering the possibility of longer service life for components and coatings. However, the state of the knowledge is based on a small number of studies with empirically drawn relationships, where no concrete explanation of behaviour has been made. The thesis will serve to fill this gap. Oxidation behaviour will be explored first in bulk nanostructured samples subjected to controlled isothermal oxidation experiments. Second, the benefits of nanostructure will be extrapolated to more realistic industrial conditions.

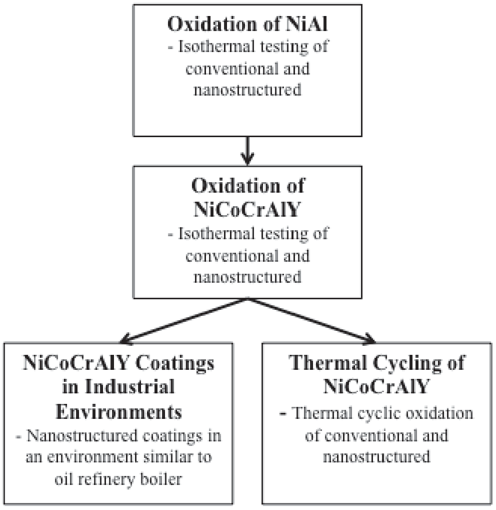

Figure 2.1: Overall project outline for this thesis.

This manuscript-based thesis is divided into four chapters that focus on the oxidation of Al-containing Ni-based alloys. The project is outlined in Figure 2.1.

- Chapter 4 describes the oxidation of the key single-phase component, NiAl. It explores the effect of nanostructure on oxidation mechanisms through isothermal oxidation kinetics of cryomilled and conventional NiAl samples, consolidated by spark plasma sintering. Differences in oxidation behaviour were explored through thermogravimetric analysis, dynamic scanning calorimetry and residual strain analysis, with particular emphasis on the formation and metastable phase transformation of alumina.
- In Chapter 5 the isothermal oxidation of conventional and grain refined NiCoCrAlY itself is studied. This chapter investigates the oxidation performance of cryomilled and conventional bulk NiCoCrAlY samples, consolidated by spark plasma sintering. Using similar oxidation conditions to Chapter 4, kinetics were studied through thermogravimetric analysis and compared to kinetics in NiAl as well as existing studies on MCrAlY.
- Having established an understanding of oxidation behaviour under controlled conditions, the next two chapters explore the oxidation of NiCoCrAlY subject to a different consolidation technique, a variation of industrial environments, and cyclic oxidation. Chapter 6 explores the effect of environment. Freestanding nanostructured NiCoCrAlY coatings were subjected to isothermal oxidation testing in an environment containing SO_2 and varying levels of water vapour, to mimic the conditions in an oil refinery boiler.

- Chapter 7 discusses the thermal cycling performance of the bulk NiCoCrAlY samples, with an emphasis on the improved thermal cycling performance of nanostructured samples through reduced spallation and subsequent internal oxidation.

Chapter 3: Experimental Methods and Materials

3.1 Starting Materials

Two alloys were used for fabrication and subsequent oxidation testing. The first was an intermetallic nickel aluminum alloy consisting of 50% Ni and 50% Al, in atomic %. This alloy was obtained as commercially available 99.0% pure nickel aluminum intermetallic powder from Alfa Aesar. The second starting material was a commercially available gas atomized two-phase NiCoCrAlY alloy powder, Ni-130/Ni-191 from Praxair Surface Technologies. The compositions of the starting powders, as specified by Praxair S.T., are presented in Table 3.1, and micrographs of the starting powders are presented in Figure 3.1.

Table 3.1: Chemical composition of the starting powders

	Alloy Composition (Mass %)				
	Ni	Co	Cr	Al	Y
NiAl	68			32	
NiCoCrAlY	46.5	23	17	13	0.5

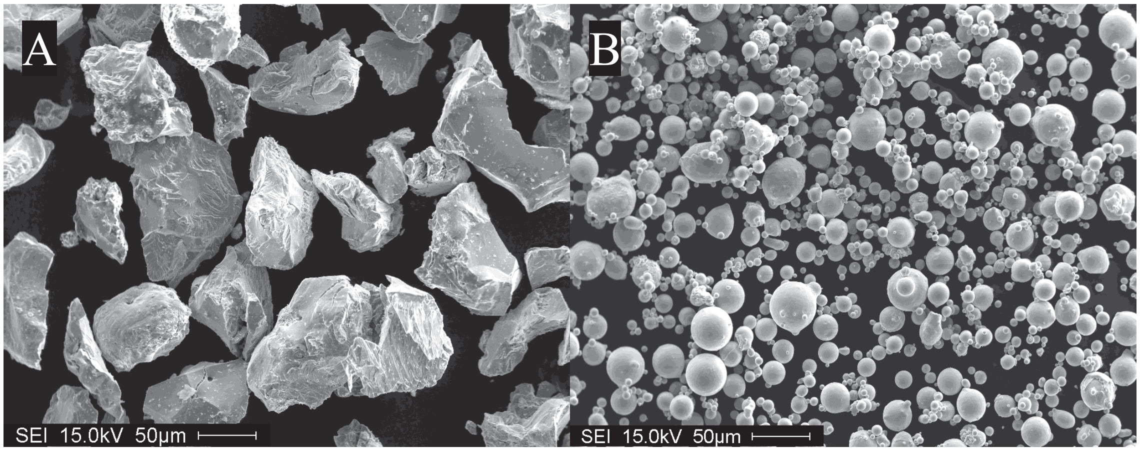

Figure 3.1: Micrographs of the as-received NiAl (A) and NiCoCrAlY (B) powders.

3.2 Fabrication Techniques

3.2.1 Cryomilling

Portions of both the NiAl and NiCoCrAlY powders were subjected to cryomilling to refine grain structure. Small-batch cryomilling of the NiAl powder was carried out in a Union process HD-01 attrition mill, in a stainless steel vial with stainless steel grinding media. Large-batch cryomilling of the NiCoCrAlY powder was carried out in a union process 1-S attrition mill, also using stainless steel vials and grinding media. The milling setup is presented in Figure 3.2.

In both cases milling was conducted for 16 hours, using a ball to powder ratio of 32:1. Impeller rotation speed was 180 revolutions per minute. To reduce adhesion of powder to the grinding media, impeller, and inside of the vial, 0.2% stearic acid (chemical formula: $CH_3(CH_2)_{16}CO_2H$) was added as a surfactant. Liquid nitrogen was continuously added to the vessel to maintain cryogenic temperature of –196°C and to reduce oxidation.

Figure 3.2: The Union Process mill used for grain refinement of the NiCoCrAlY powder.

3.2.2 Spark Plasma Sintering

Spark plasma sintering of nanostructured and conventional samples of both powders was conducted in a Thermal Technologies 10-3 SPS unit, shown in Figure 3.3. Iso-Carb 85 graphite dies with 20 mm diameter were used to press pucks of thicknesses ranging from 3 to 8 mm. Temperature was monitored via a thermocouple inserted into the lower punch and feeding a PID control loop. Pressure is applied to the die through hydraulic rams mated to a 10-ton press. In this case pressure was limited to 50 MPa due to structural stability limitations of the graphite dies. Pulsed DC current is generated from three 1000-amp power supplies in series, capable of generating a maximum current of 3000 amps and a maximum voltage of 10 V. Both the hydraulic press and power supplies are mated to the PID controller, such that custom heating and pressure profiles can be created. With proper controller tuning, heating rates in the 100's of degrees Celsius can be obtained. A sealed chamber surrounding the die and mechanical vacuum pump ensured that all sintering took place under vacuum.

Figure 3.3: The Thermal Technologies SPS used for powder consolidation.

A series of test samples were necessary to determine the ideal consolidation procedure for each powder. In both conventional and nanostructured powders density should be maximized, but in the nanostructured powders this must be achieved ideally with minimal grain growth. Density was measured using the Archimedes method according to ASTM Standard B962-08. The equation used to calculate density:

$$\theta = \frac{m_a \theta_w}{m_{ao} - (m_{wo} - m_{wire})} \qquad \text{Eq. 3.1}$$

where θ is the density of the sample, m_a is the mass of the sample in air, θ_w is the density of water (1.006 g/cm^3 at room temperature), m_{ao} is the mass of the sample impregnated with oil and measured in air, and m_{wo} is the mass of the sample impregnated with oil and measured in water. Finally m_{wire} is the mass of the wire used to suspend the sample in water. Grain size was measured via x-ray diffraction using the Scherrer Equation [3.1], which will be discussed, in a later section. Using the measured densities and grain sizes, an optimum sintering program was obtained for each sample category that would maximize sample density while also minimizing grain growth in nanostructured samples.

NiAl and NiCoCrAlY powders were stored in sealed containers in a humidity-controlled cabinet. Conventional NiAl powders were heated at 150°C/minute up to 1500°C, held at this temperature for 10 seconds, cooled to 1400°C, held for 30 minutes and finally cooled to ambient temperature. Nanostructured NiAl powder were also heated at 150°C/minute up to 1500°C, but in this case they were held for 15 seconds and immediately cooled to room temperature. Conventional NiCoCrAlY samples were heated using a 200°C/minute ramp to 1100°C, held for 7 minutes and cooled to ambient temperature. Lastly, nanostructured NiCoCrAlY powder was heated at 250°C/minute to

1100°C, held for 10 seconds and finally cooled to ambient temperature. In all cases density of the final sample was over 96% of theoretical density. In all cases a vacuum of at least 6 x 10^{-2} torr was maintained.

3.2.3 High-Velocity Oxy-Flame Spray

Nanostructured NiCoCrAlY powder was deposited onto copper substrates measuring approximately10 x 50 x 70 mm. Deposition was conducted at Raymor Industries Inc. via high-velocity oxy-flame spray (HVOF), using proprietary thermal spray parameters used for deposition of MCrAlY bond coats in aerospace applications. The bulk of the copper substrates was cut away, leaving behind only a thin layer of copper, that was leached in a 15% nitric acid bath. The final samples were freestanding coatings of 470 μm average thickness. The final freestanding coatings, used also in a study by Mercier *et al.* [3.2] are presented in Figure 3.4.

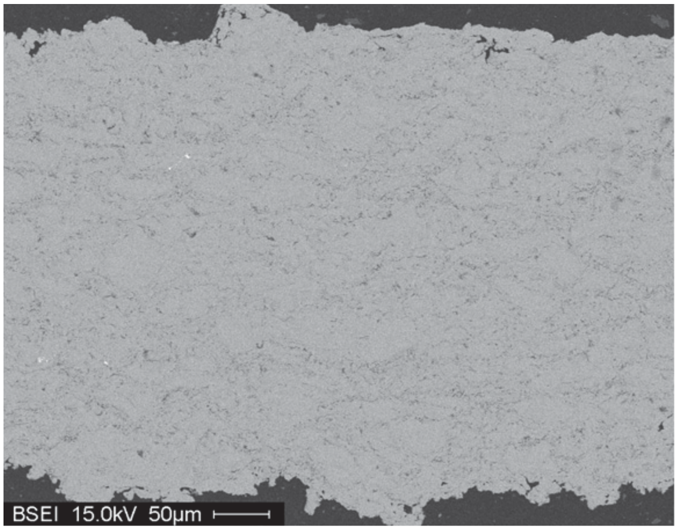

Figure 3.4: Freestanding NiCoCrAlY coatings fabricated by HVOF [3.2].

3.3 Oxidation

A series of oxidation tests were undertaken to evaluate the oxidation behaviour of the various samples produced for this thesis. The focus of these tests was both a comparison of oxidation behaviour between refined and conventional grain sizes and also an evaluation of oxidation behaviour under different industrial conditions, namely mixed oxidative environments and thermal cycling.

3.3.1 Oxidation via Thermogravimetric Analysis

Isothermal Oxidation testing of NiAl and NiCoCrAlY samples consolidated by SPS was conducted in a Netsch STA 449 F3 Jupiter DT-TGA with coincident Thermogravimetric Analysis (TGA) and Differential Scanning Calorimetry (DSC). Consolidated SPS samples were cut on a diamond saw to approximately 3 x 3 x 3 mm and ground to 1200 grit on all sides. Samples were placed in the TGA and heated at 10°C/minute up to 950, 1000 and 1050°C, held at said temperature for 24 hours and cooled to ambient temperature. Heating and cooling stages were conducted under an argon purge, while during the oxidation stage synthetic air (80% nitrogen and 20% oxygen) was flowed through the sample chamber. In the case of NiAl samples, a second set of oxidation tests was conducted under identical conditions, but with synthetic air exposure during the heating stage as well as the isotherm. This second set of tests was conducted to reduce buoyancy effects during the gas change, in order to more clearly identify the onset point of oxidation.

In all cases the TGA output mass gain data in terms of mg/s, which is not normalized for surface area. The data was accordingly converted to $g/cm^2/s$ using the surface area of the sample, calculated by simple geometry from measurements made with a micrometer prior to oxidation. Parabolic rate constants were calculated from this data using the method proposed by Pierragi [3.3]. An idealized version of this calculation is presented in Figure 3.5. In Figure 3.5-A the data is plotted as mass gain versus time, and follows classic parabolic oxidation kinetics. In order to obtain the parabolic rate constant, the data is plotted against the square root of time in Figure 3.5-B, and the slope of this line is the root of the parabolic rate constant, k_p, given in $g^2/cm^4/s$. In the cases where an initial transient oxidation stage occurs, the plot of mass gain versus square root of time may have two segments, as in Figure 3.5-C. In this case the slope of each segment is calculated and related to the parabolic rate constants for the initial transient stage and final passivating stage, respectively.

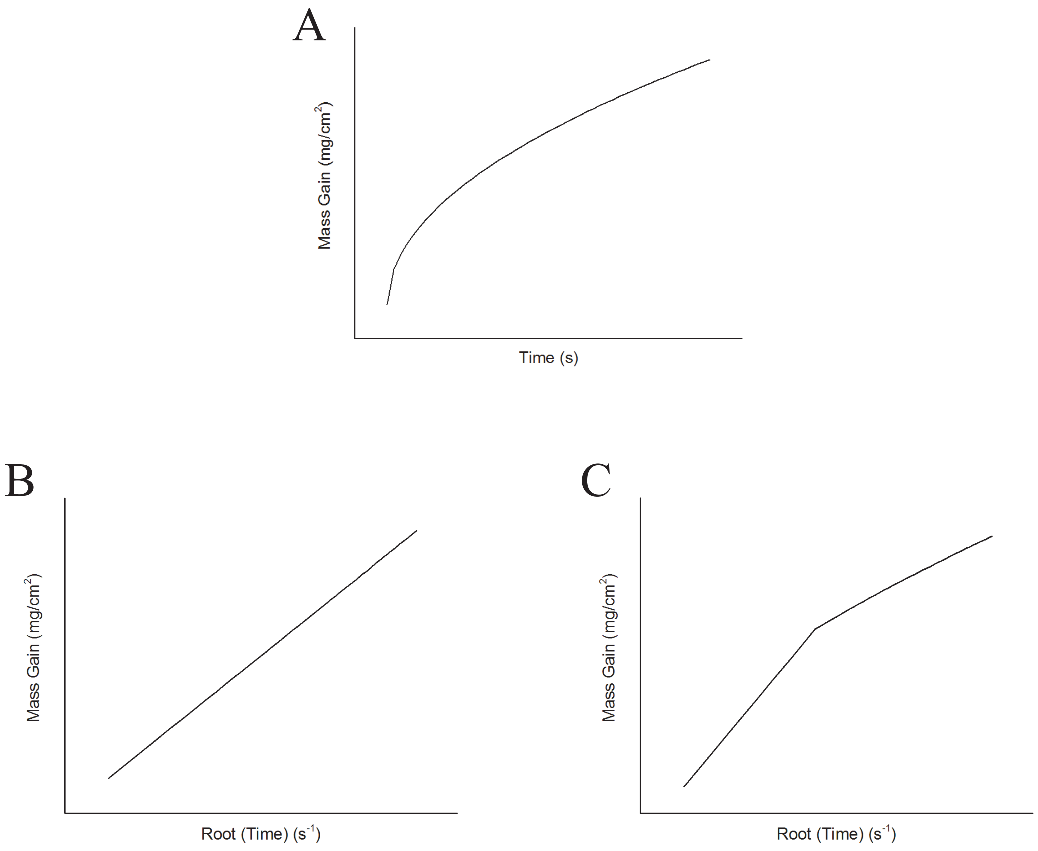

Figure 3.5: Sample plots of TGA data: (A) mass gain versus time, (B) mass gain versus the square root of time, (C) mass gain versus root(time) for two-stage oxidation.

3.3.2 Oxidation via Controlled-Environment Thermogravimetric Analysis

s^{-1}HVOF-deposited NiCoCrAlY samples were subjected to oxidation testing in humid environments in order to better understand the effect of water vapour on the oxidation behaviour of these alloys. Due to the environmental limitations of the conventional TGA described in the previous section, a custom-built controlled environment TGA was developed. This TGA used a traditional vertical ceramic tube furnace mated to a Cahn D-100 balance, shielded with helium; a schematic of the apparatus is shown in Figure 3.6, and the actual apparatus in Figure 3.7.

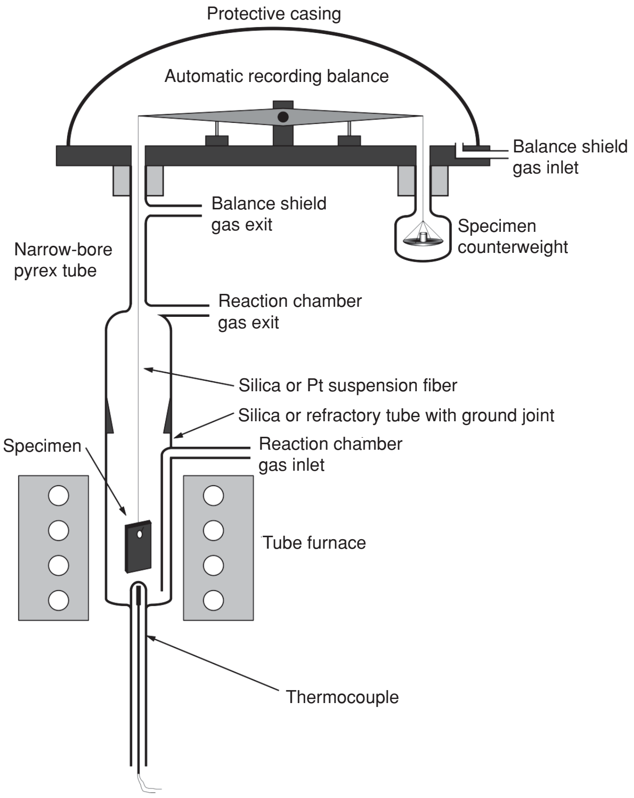

Figure 3.6: Schematic of a controlled environment testing apparatus [3.4]

After measuring surface area, samples were placed on an alumina plate suspended via a platinum wire from the balance into the furnace. The system was then closed and heated to 1000°C at 4.2°C/min with an argon gas purge flowing at 0.25 lpm. Once at temperature and stable, the Ar was replaced with air, also flowing at 0.25 lpm, for 48 hours followed by a final Ar purge and cooling. Prior to entering the furnace, the air was bubbled through water at varying temperatures to pick up 0, 4 or 8% water vapour. Calculation of parabolic rate constants (k_p) was performed using the method described in the previous section.

Figure 3.7: The custom built controlled-environment TGA.

3.3.3 Oxidation in H_2O and SO_2-Bearing Environments

Static oxidation tests of HVOF-deposited NiCoCrAlY samples were conducted in a similar custom-built tube furnace without TGA, presented in Figure 3.8. Samples were placed in the tube on an alumina sample holder then closed and heated to 1000°C at 8°C/min in air. Once the desired temperature was reached air or a mixture containing 0.5% SO_2 described in Table 3.2 was introduced. In this case a wider range of water vapour levels was used: the incoming gas was bubbled through a water bath at various temperatures to pick up 0, 2, 4, 6 or 8% water vapour.

Table 3.2: Composition of the SO_2-bearing environment

Gas Composition (Mass %)			
N_2	CO_2	O_2	SO_2
82.5	12	5	0.5

Figure 3.8: Apparatus for controlled-environment static oxidation tests.

Tests of 24-hour durations were run; in each case the system was purged with air on completion of the test and furnace-cooled to ambient temperature. Mass of samples for the oxidation tests was measured before and after testing using a Sartorius BP 110S scale.

3.3.4 Thermal Cyclic Oxidation

SPS-consolidated NiCoCrAlY samples were subject to thermal cycling in air. Cyclic oxidation testing was conducted in a custom-built tube furnace, where the hot section of the furnace was rail-mounted and could be moved onto or off of a quartz tube. Three full SPS-consolidated discs were kept for the 200-cycle tests, while half-discs were used for the shorter tests. The samples were polished to 1200 grit on all surfaces and placed in the quartz tube on an alumina sample holder, after which a continuous flow of laboratory air was introduced at 2 lpm. The furnace was heated to 1000°C and, once at temperature, moved over the quartz tube such that the samples were aligned with the hot zone of the furnace. A thermocouple on the sample holder reached 1000°C within 3 minutes. After 60 minutes the furnace was moved away and the airflow increased to 8 lpm for a 15-minute forced-air quench. The airflow was then reduced once again to 2 lpm and the cycle restarted. After every 8 cycles the samples were removed from the furnace and weighed. Samples were removed after 24, 48, 96 and 144 cycles to characterize morphology, and 3 samples were kept for 200 cycles to monitor mass change.

3.4 Analysis & Characterization

3.4.1 Thermodynamic modelling

A thermodynamic study of the oxidation of the NiCoCrAlY system was also conducted using FactSage thermochemical software. In oxidation of alumina-forming alloys, the oxygen partial pressure can vary through the thermally grown oxide layers. At the metal interface, the oxygen partial pressure is low and the system is considered to be in metallic saturation. A gradient of oxygen partial pressure exists across the oxide layer, and the gas interface can be considered in relative oxygen saturation. Calculations using the FACT53, FTOxid and SGTE databases were conducted to determine the oxide layers present at equilibrium in the SO_2-bearing environment with 4% water vapour. The thermodynamic calculations do not account for the kinetic effects of diffusion and also assume the entire metallic substrate reacted to form oxide.

3.4.2 X-Ray Diffraction

Conventional X-Ray Diffraction (XRD) patterns were acquired using a Bruker D8 Discover XRD using a Cu source (Cu Kα λ = 1.54056 Å) and Vantec-5000 2D detector operated at various scan angles, with a dwell time of 200 seconds per frame. Additional conventional XRD scans were Philips PW1070 X-Ray Diffractometer with a Cu source and point detector, operated at a scan angle ranging from 30° to 80°, step size of 0.005° and dwell time of 0.5s per step.

Glancing-Angle X-Ray Diffraction (GAXRD) patterns were obtained on the Bruker D8 using a Cu source and Lynxeye point detector with an incident angle of 2°, a scan angle ranging from 30° to 60°, a step size of 0.005° and a dwell time of 0.5s. Additional GAXRD scans were obtained using the same source and incident angle, but with a Vantec-5000 2D detector using a dwell time of 200 seconds per frame at various scan angles.

Finally, in-situ X-Ray Diffraction was conducted during high temperature oxidation using the same Bruker D8 Discover XRD with a platinum band heating stage, Cu source and Vantec-5000 2D detector. Samples were heated in ambient air at 10°C per minute, with in-situ XRD scans taken at multiple increments from 500 to 1000°C. In all cases phase identification was completed using X'Pert HighScore software.

3.4.3 Electron Microscopy

Cross sectional samples were mounted in Bakelite and ground using 220 and 320 grit silicon carbide paper, followed by polishing with 9 and 3 μm diamond suspension and final polishing using 0.05μm colloidal silica suspension on a Buehler Vibromet auto-polisher for a minimum of 2 hours.

Micrographs of polished cross-sections and oxidized surfaces were obtained using a Philips XL-30 FE-SEM with EDAX energy-dispersive x-ray spectroscopy (EDS) operated at 10 or 15 kV. Oxide layer thickness and β-phase depletion depth were measured from cross-section backscattered electron images using Clemex Vision software. Grain size of the ultrafine SPS-consolidated NiCoCrAlY samples was direct measured via SEM using the intersecting line method averaging at least 100 grains.

Grain size measurement of the nanostructured SPS-consolidated NiAl samples was carried out via Transmission Electron Microscopy (TEM) on a Philips CM200 TEM operated at 200 keV. Samples were prepared first by manual polishing with 1200 grit silicon carbide paper and second via electropolishing at 37 V in a solution of 25% Nitric Acid in Ethanol at -25°C. Grain size was averaged over approximately 100 grains in 8 micrographs.

3.5 References

[3.1] B. D. Cullity, Elements of X-Ray Diffraction, 2nd edition, Addison-Wesley, Reading, Massachusetts, 1978.

[3.2] D. Mercier, B. D. Gauntt, M. Brochu, *Thermal stability and oxidation behavior of nanostructured NiCoCrAlY coatings*, Surface and Coatings Technology 205 (2011) 4162-4168.

[3.3] B. Pierragi, *Calculations of parabolic reaction rate constants*, Oxidation of Metals 27 (1987) 177-185.

[3.4] N. Birks, G. H. Meier, F. S. Pettit, *Introduction to the high temperature of metals*, 2nd edition, Cambridge University Press, Cambridge, 2006.

Chapter 4: The effect of grain size on the oxidation of NiAl

C. Kaplin, R. Ivanov, M. Paliwal, I.-H. Jung and M. Brochu
McGill University
Department of Materials Engineering
3610 University Street, Montreal, QC, H3A 0C5

Preface

To understand the effect of nanostructure on the oxidation of the two-phase MCrAlY system, its effect on the constituent β-NiAl phase must first be explored. The β phase provides the source of aluminum in the formation of the alumina scale on MCrAlY alloys; as such its presence is essential to the oxidation performance of these alloys. The following chapter, to be submitted for publication in the journal "Intermetallics", explores isothermal oxidation kinetics of cryomilled and conventional NiAl samples, consolidated by spark plasma sintering. Differences in oxidation behaviour were studied through thermogravimetric analysis, dynamic scanning calorimetry and residual strain analysis, with particular emphasis on the formation and metastable phase transformation of alumina.

Abstract

Bulk nanostructured NiAl samples with a grain size of 104 nm have been obtained through cryomilling of NiAl intermetallic feedstock powder and subsequent sintering via SPS. Oxidation testing of these conventional and nanostructured NiAl samples reveals that while the conventional samples have oxidation rates on the order of 10^{-11} $g^2/cm^4/s$ across all tested temperatures, nanostructured samples demonstrate decreasing oxidation rates with temperature, as low as 6.78×10^{-13} $g^2/cm^4/s$. This decrease in oxidation rate is attributed to an earlier transition through the metastable aluminum oxide phases, resulting in a stable slow growing α-Al_2O_3 phase earlier in the oxidation tests. In-situ XRD during high-temperature oxidation testing has shown that lattice strain at the surface of the nanostructured samples is substantially higher than conventional, and that the decrease of this lattice strain with temperature is significant. It

is believed that the relief of this lattice strain stimulates the earlier θ-α transition seen in the nanostructured samples.

4.1 Introduction

A number of industrial processes and components including petroleum refining, nuclear power generation, aircraft turbine engines and land-based gas turbines operate in harsh environments where materials are regularly exposed to high temperatures, oxidative and corrosive gases [4.1]. In the particular case of gas turbines, efficiency generally increases with operating temperature, and as such the push for higher operating temperatures is a continual focus of research. Current practices to attain this goal include using various superalloy substrates and thermal barrier coatings (TBC).

A typical TBC consists of an yttria-partially-stabilized zirconia (YPSZ) top coat and nickel superalloy bond coat, normally of the MCrAlY class of alloys. These bond coats are chosen for their ability to grow Al_2O_3 on their surface when exposed to oxidative conditions, due to the presence of the β-NiAl intermetallic phase that provides a source of aluminum during high temperature oxidation [4.2]. The degradation of these coatings is often caused by faster growing spinel oxides that occur over the thermally grown alumina layer. Consequently, numerous studies have focused on improving the oxidation performance of MCrAlY alloys [4.3, 4.4] including several that have focused on nanostructuring of the base alloy in order to produce denser, thinner alumina layers [4.5-4.7].

While current studies indicate that nanostructure can be beneficial to the oxidation properties of MCrAlY alloys [4.5-4.7], little research to date has been conducted on nanostructuring of the NiAl intermetallic phase in and of itself. It stands to reason that since the β-NiAl phase seeds oxidation in MCrAlY class alloys, understanding the benefits of nanostructure in the NiAl system would serve to deepen understanding of the MCrAlY system overall, yet a deeper investigation of these effects remains to be made. Studies by Joardar *et al.*, Xu *et al.* and others have shed much light on the synthesis and mechanical properties of nanostructured NiAl [4.8-4.11] but few have delved into oxidation. This being said, the oxidation of conventional grain sized NiAl has been studied extensively. Research in the 90's by Brumm and Grabke [4.12, 4.13] as well as the work of Yang *et al.* [4.14] established firmly the transient oxidation mechanism of NiAl. The growth of the alumina scale on NiAl transitions through several metastable structures: δ-Al_2O_3, γ- Al_2O_3 and θ-Al_2O_3 before eventually transforming to the stable corundum α-Al_2O_3 phase. The initial phases δ and γ have a cubic structure that transforms to monoclinic in the case of θ with a corresponding 11% increase in density [4.15]. The final transition from monoclinic θ-Al_2O_3 to the rhombohedral α-Al_2O_3 results in another 12% change in density [4.15]. An earlier transition to α-Al_2O_3 is desirable because the slow diffusion of cations and oxygen through its lattice results in a slow and dense growing oxide [4.12]. Brumm and Grabke conducted extensive work on the θ-α transition, finding that at 900°C the initial oxide formed is γ with a relatively quick transition to θ while the transition to α can be measured in hundreds of hours. It was found that in the range of 950 to 1050°C the θ-α transition is the dominant effect, and a drop in oxidation rate can be seen as this change occurs, typically studies show a drop in oxidation rate of approximately one order of magnitude or less after the transition to α. In contrast at 1100°C the transition to α is too short to be measurable by TGA [4.12]. Yang *et al.* later established that the transition to α-alumina is nucleated at the metal-oxide interface and grows outward to consume existing θ-alumina.

The purpose of this study is to investigate the oxidation behaviour of conventional nanostructured bulk NiAl samples consolidated via Spark Plasma Sintering (SPS) in order to better understand the effect of nanostructure on the key β-NiAl intermetallic phase within the MCrAlY system. Cryomilling has been chosen as the method for forming nanostructure in the NiAl precursor powder, while SPS has been selected for sintering, as it is a promising technique for the consolidation of bulk nanostructured samples [4.16, 4.17]. This research is aimed at understanding oxidation kinetics through Thermogravimetric Analysis and Dynamic Scanning Calorimetry. Additionally, this study seeks to determine the potential underlying effect of nanostructure on the oxidizing surface through in-situ X-Ray Diffraction during high-temperature oxidation tests.

4.2 Experimental Procedures

NiAl samples were produced from commercially available 99.0% pure nickel aluminum intermetallic powder obtained from Alfa Aesar. A portion of said powder was nanostructured via cryomilling for 16 hours in a Union Process S-01 attrition mill at 180 rpm with stainless steel grinding media, with a ball to powder ratio of 32:1 and 0.2% stearic acid added as a surfactant to prevent coating the balls and interior of the milling vessel. Liquid nitrogen was continuously added to the vessel.

SPS was used to consolidate the conventional and nanostructured powder using a Thermal Technologies 10-3 unit. In all cases sintering was conducted under vacuum using a 150°C/minute ramp to 1500°C. Conventional samples were heated to 1500°C, cooled to 1400°C, held for 30 minutes and finally cooled to ambient temperature, while cryomilled samples were held at 1500°C for 15 seconds and cooled to ambient temperature. Samples fabricated by cryomilling and SPS sintering will henceforth be referred to as “nanostructured”. Density was measured using the Archimedes principle and grain size of the nanostructured samples was measured both via X-Ray Diffraction using the Scherrer Equation and via Transmission Electron Microscopy.

Transmission Electron Microscopy (TEM) was carried out on a Philips CM200 TEM operated at 200 keV. Samples were prepared first by manual polishing and second via electropolishing at 37 V in a solution of 25% Nitric Acid in Ethanol at -25°C. Grain size was averaged over approximately 100 grains in 8 micrographs.

Isothermal Oxidation testing was conducted in a Netsch STA 449 F3 Jupiter DT-TGA with coincident Thermogravimetric Analysis (TGA) and Differential Scanning Calorimetry (DSC). Consolidated SPS samples were cut on a diamond saw to approximately 3 x 3 x 3 mm and ground to 1200 grit on all sides. Samples were placed in the TGA and heated at 10°C/minute up to 950, 1000 and 1050°C, held at said temperature for 24 hours and cooled to ambient temperature. A first set of samples was heated and cooled in Ar, while exposed to a mixture of 80% N_2 and 20% O_2 during the isotherm. In order to clearly identify the onset point of oxidation, a second set of tests was conducted with synthetic air exposure throughout both the heating and isothermal stages. Parabolic rate constants were calculated using the method proposed by Pierragi [4.18].

X-Ray Diffraction (XRD) patterns were acquired using a Bruker D8 Discover XRD. Glancing-Angle X-Ray Diffraction (GAXRD) patterns were obtained using a Cu source and Lynxeye point detector with an incident angle of 2°, a step size of 0.005° and a dwell time of 0.5s. In-situ X-Ray Diffraction (XRD) was conducted during high temperature oxidation using the same Bruker D8 Discover XRD with a platinum band heating stage, Cu source and Vantec-5000 2D detector. Samples were heated in ambient air at the same ramp rate as the previous TGA and DSC experiments, with in-situ XRD scans taken at multiple increments from 500 to 1000°C. In all cases phase identification was completed using X'Pert HighScore software. Scanning electron microscope (SEM) observations were carried out on a Philips XL-30 FE-SEM with EDAX EDS.

4.3 Results & Discussion

4.3.1 Cryomilling and Consolidation of NiAl Powders

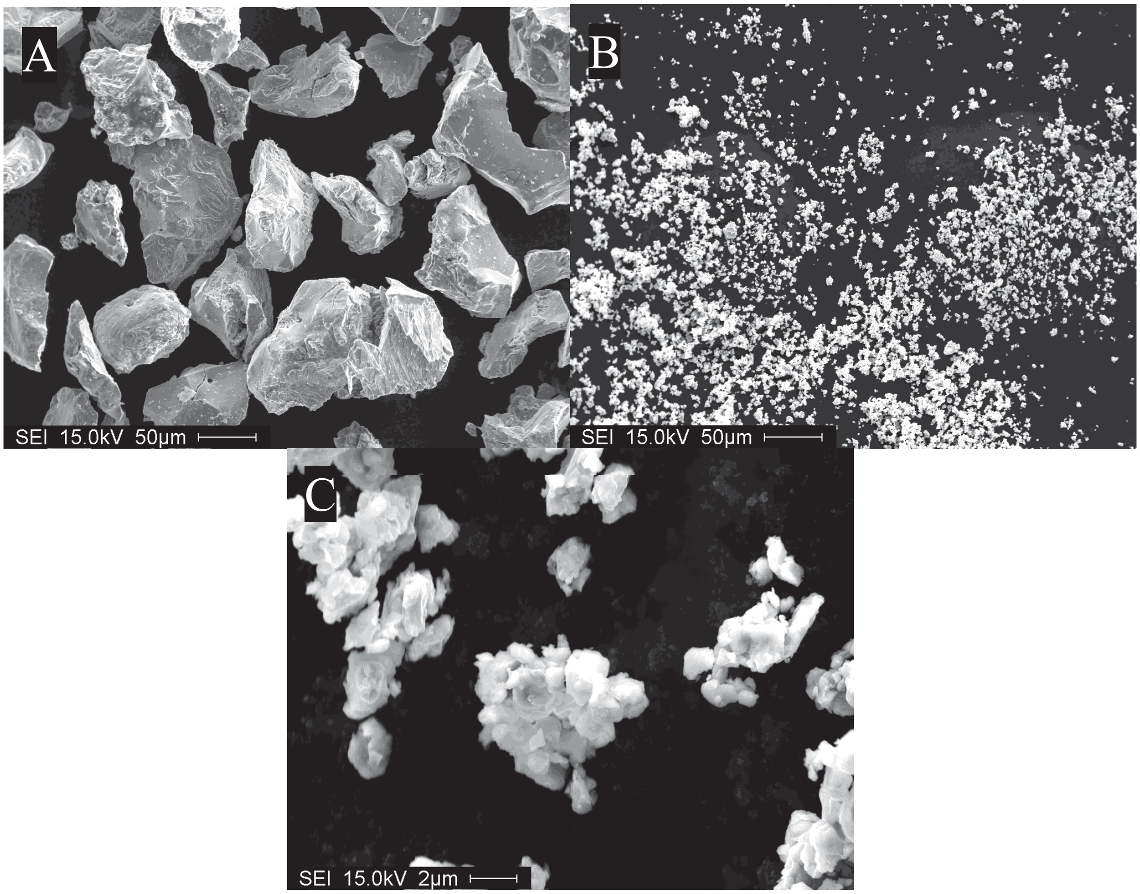

Figure 4.1: SEM images of as-received NiAl powder (A), cryomilled powder (B) and cryomilled powder at higher magnification (C).

Figure 4.1 shows SEM images of the NiAl powder before and after cryomilling. The cryomilled powder has a significantly smaller morphology while also showing the classic flattened, agglomerated morphology associated with milled powders. XRD patterns of the as-received conventional powder and milled powder are shown in Figure 4.2. All peaks present have been identified as NiAl phase, JCPDS #03-065-4197. Note the distinct peak broadening of the cryomilled powder with respect to conventional, also indicating that said powder has a refined grain structure.

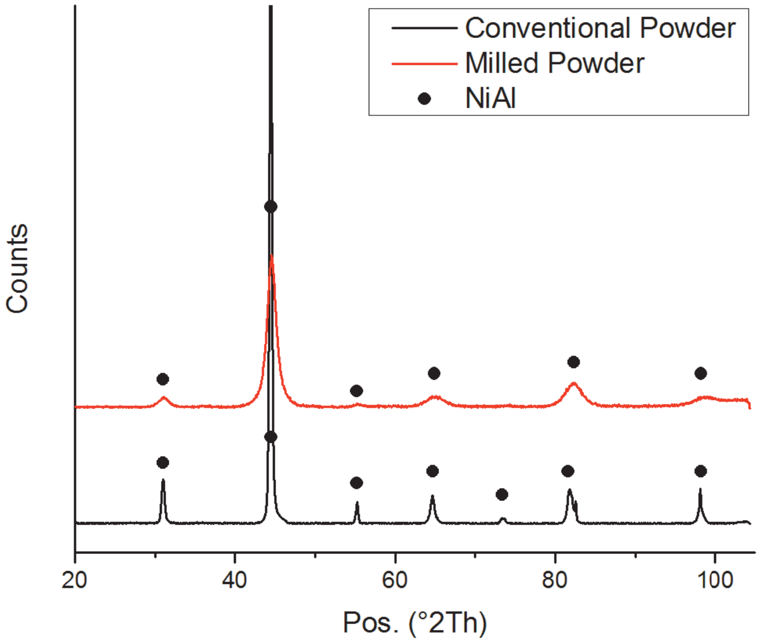

Figure 4.2: XRD patterns for conventional and cryomilled NiAl powder.

Cross-sectional images obtained by SEM of consolidated conventional and nanostructured samples are presented in Figure 4.3 and clearly show the difference in grain size of the consolidated samples. While the conventional sample has a grain size on the order of 20 to 60 microns, the nanostructured sample has a grain size of 104 nm according to XRD analysis using the Scherrer Equation [4.19] or an average of 94 nm direct-measured via TEM, with many grains in the 20-60 nm range. A representative TEM micrograph of a consolidated nanostructured sample is presented in Figure 4.4 and the grain size distribution from TEM grain size measurements is presented in Figure 4.5. Both conventional and nanostructured samples were consolidated to within 98% of theoretical density.

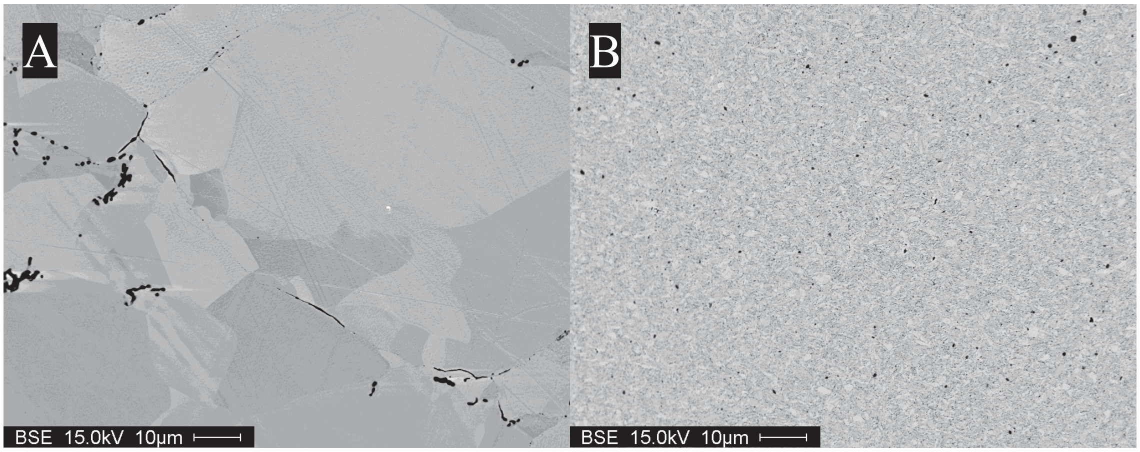

Figure 4.3: Cross-sectional SEM images of consolidated conventional (A) and nanostructured (B) NiAl samples.

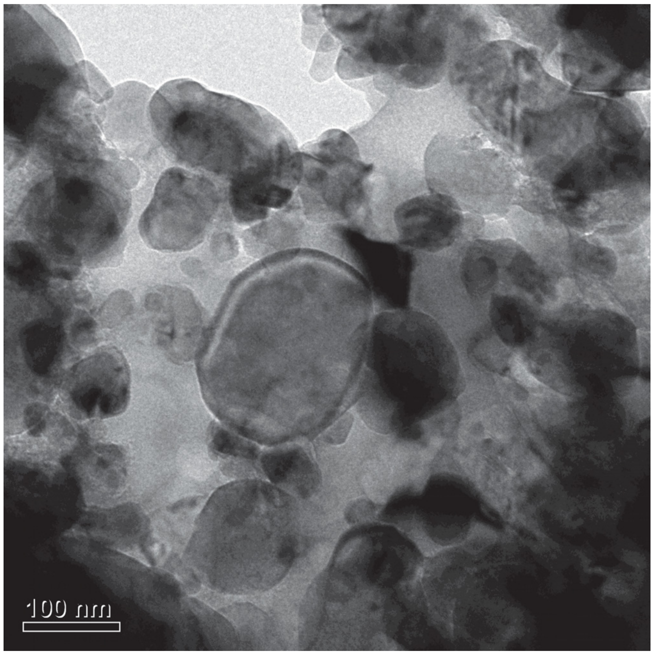

Figure 4.4: TEM image of consolidated nanostructured NiAl sample showing sub-100 nanometer grains.

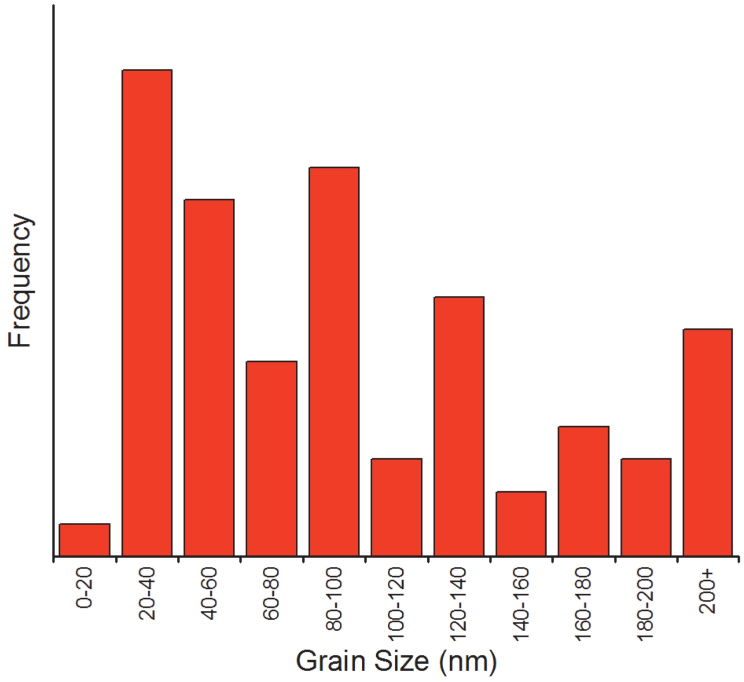

Figure 4.5: Grain size distribution of consolidated nanostructured NiAl sample, direct-measured via TEM.

4.3.2 Oxidation of Conventional and Nanostructured NiAl

Following successful fabrication of the conventional and nanostructured samples, oxidation tests were performed to compare their oxidation behaviour. The first set of oxidation tests were conducted with a ramp in Ar followed by isothermals at 950, 1000 and 1050°C in air for both nanostructured and conventional samples; the corresponding thermogravimetric data is presented in Figure 4.6. Slight fluctuations in the TGA curves are due to minor air pressure variations in the TGA chamber and are attributed entirely to machine error, as corresponding DSC data indicates stable, steady state oxidation for all samples. It is clear that nanostructured samples have distinctly less mass gain than their conventional counterparts throughout the test and also show a pattern of decreasing total mass gain with increasing temperature. This being said, the drop in oxidation rate due to the θ-α transition, expected in the early stages of oxidation for this temperature range is difficult to pinpoint in this experimental methodology.

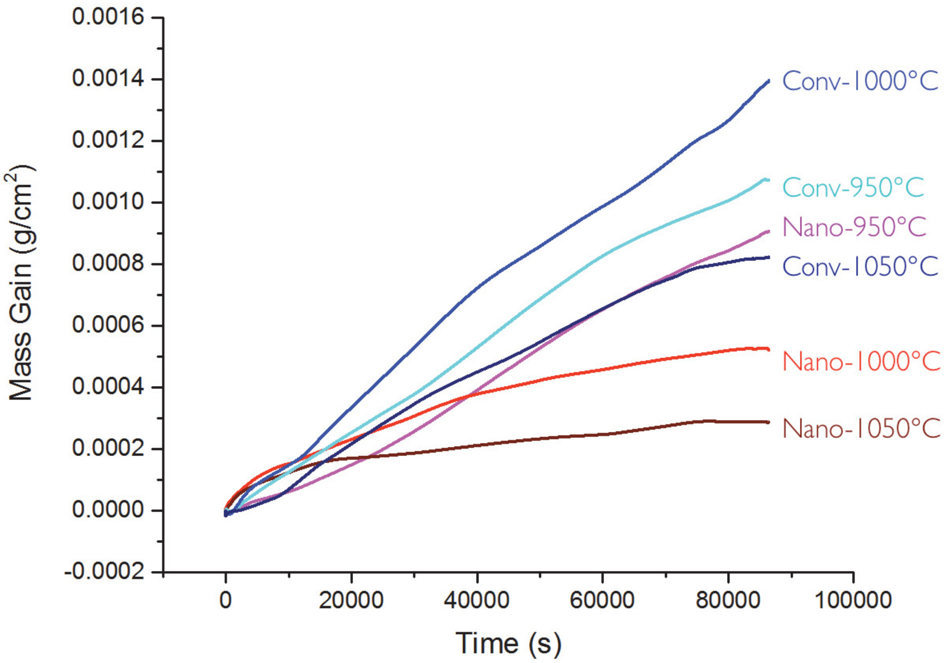

Figure 4.6: TGA data for conventional and nanostructured samples oxidized for 24 hours in air at 950, 1000 and 1050°C.

Parabolic rate constants calculated from this TGA data, using the method presented in section 3.3.1 are presented in Table 4.1 along with a reference rate constant from a previous study of HVOF-consolidated nanostructured NiCoCrAlY samples oxidized under similar conditions [4.7]. It is important to note that the conventional samples demonstrate similar oxidation rates on the order of 10^{-11} $g^2/cm^4/s$, while the nanostructured samples have oxidation rates that decrease with temperature, as low as 6.78×10^{-13} for the sample oxidized at 1050°C. Unsurprisingly, the nanostructured NiAl samples oxidized at 1000°C has a lower rate constant than the reference NiCoCrAlY sample, given the notably higher aluminum concentration in the intermetallic. A second comparative reference is presented in Figure 4.7, where the oxidation rates presented in Table 4.1 are superimposed over a summary graph from [4.12] showing numerous oxidation rates and corresponding transient oxides being formed. It is important to note that the oxidation rates for this reference study [4.12] are for large, cast NiAl samples oxidized up to several hundred hours in an atmosphere made up of He and 0.13 bar O_2.

Table 4.1: Parabolic rate constants for conventional and nanostructured samples oxidized for 24 hours in air at 950, 1000 and 1050°C.

	Parabolic Rate Constant, k_p ($g^2/cm^4/s$)	
Temp (°C)	Conventional	Nano
950	2.19×10^{-11}	1.65×10^{-11}
1000	3.27×10^{-11}	2.05×10^{-12}
1050	1.42×10^{-11}	6.78×10^{-13}
	Reference: nanostructured NiCoCrAlY [4.7]	
1000		2.27×10^{-11}

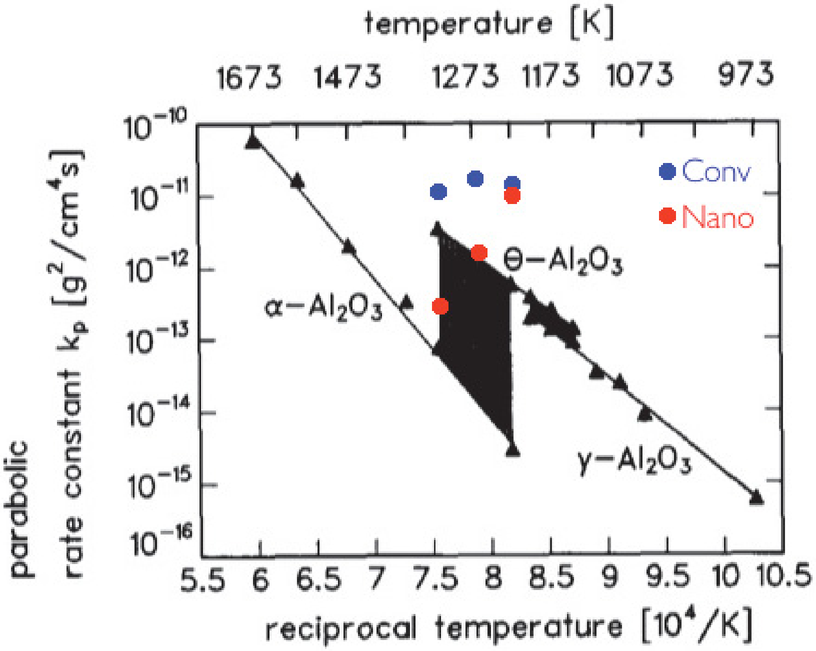

Figure 4.7: Comparison of oxidation rates from the current study to the work of Brumm & Grabke [4.12].

4.3.3 Initial Stage Oxidation Testing

The first set of oxidation results show clearly improved oxidation performance through nanostructuring. However, as mentioned earlier, the current results do not paint a clear picture of the initial stages of oxidation. Consequently, a second oxidation test was undertaken, this time with both the ramp and isothermal segments being conducted in air, with coincident DSC. The DSC data corresponding to this ramp is presented in Figure 4.8, with key peaks marked. Two exothermic peaks are present. The first (Peak 1) occurs slightly below 572°C in both samples; Wefers and Misra have identified the onset of γ in the γ-θ-α transition to occur between 500 and 725°C [4.12]. Interestingly, the onset of the second peak (Peak 2) occurs at a notably lower temperature in the nanostructured sample (671°C) than in the conventional (829°C). The authors believe this peak can be attributed to the onset of a transition from a metastable alumina to the more stable corundum structure, and that this earlier transition to a denser and more passivating layer of alumina leads in turn to overall lower oxidation rates. Yang *et al.* have identified α-alumina nucleation at the NiAl-θ-alumina interface of a sample oxidized at 950°C but did not conduct tests at lower temperature [4.14], an onset of the θ-α transition at 829°C nonetheless correlates well with his work.

This point can also be highlighted by the corresponding TGA data, through the entire isothermal stage, that is presented in Figure 4.9. In this case the ramp segment has been included, to show the change from initial rapid oxidation to stable oxidation indicative of a passivating layer. The inflection points have been circled and, as the DSC would indicate, the nanostructured sample has an earlier transition and overall lower oxidation rate that the conventional counterpart. These oxidation rates are presented in

Table 4.2, and have been calculated for both the initial oxidation stage and second oxidation stage. The conventional sample, as expected, shows a drop in oxidation rate transitioning from first to second stage, being roughly 5x lower, though both remain on the order of 10^{-11} $g^2/cm^4/s$. In contrast, the nanostructured sample has an initial oxidation rate a full order of magnitude higher (10^{-10}) than the conventional sample followed by a second stage oxidation rate that is a full order of magnitude lower (10^{-12}) than the conventional sample. This substantial drop in oxidation rate between initial and second stage oxidation is significantly larger than the conventional sample and others identified in literature [4.6, 4.12].

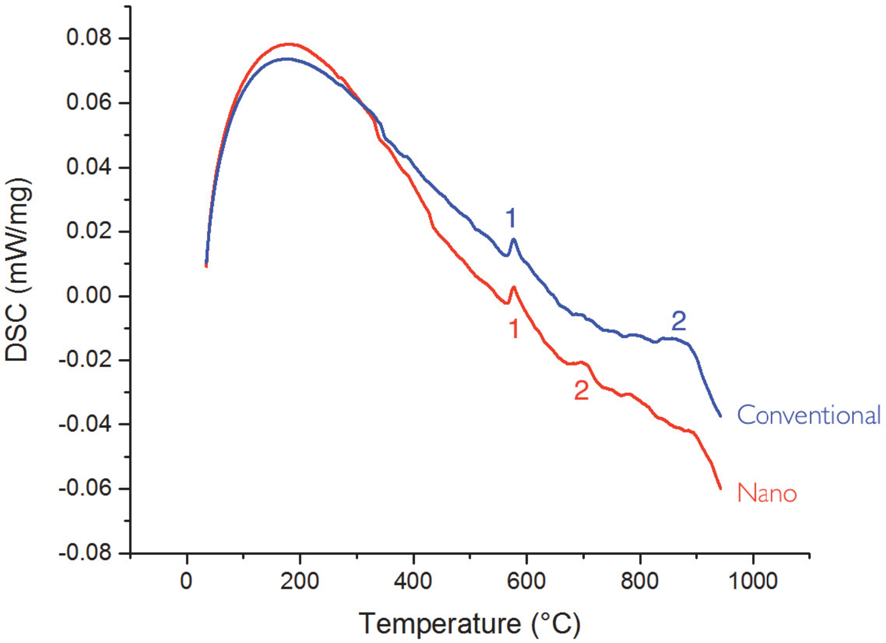

Figure 4.8: DSC data for conventional and nanostructured samples oxidized in air up to 950°C, exothermic oxidation peaks have been identified.

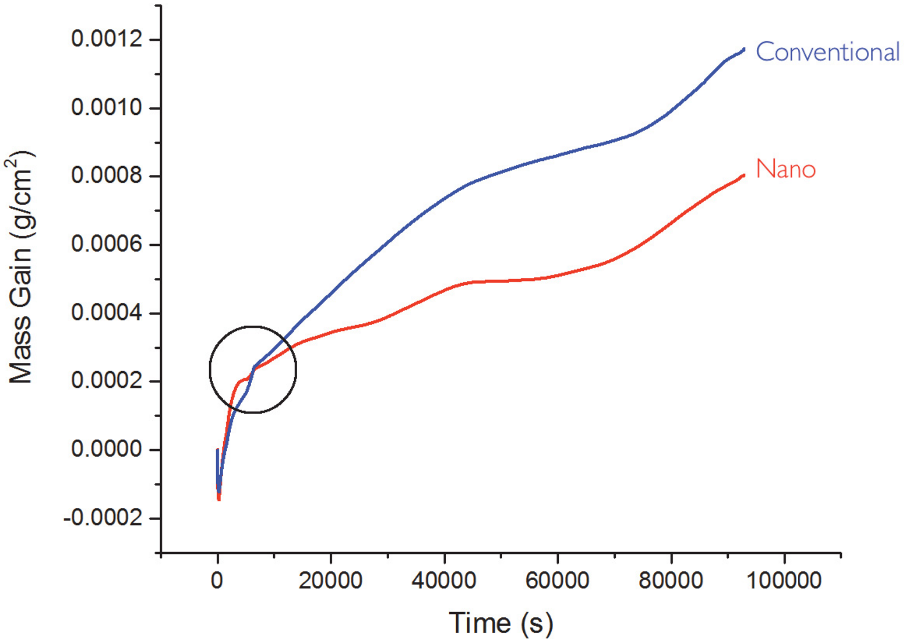

Figure 4.9: TGA data for conventional and nanostructured samples oxidized for 24 hours in air at 1050°C, key inflection points have been circled.

Table 4.2: Initial stage and second stage parabolic rate constants for conventional and nanostructured samples oxidized for 24 hours in air at 1050°C.

	Parabolic Rate Constant, k_p ($g^2/cm^4/s$)	
Temp (°C)	Conventional	Nano
1050 – Initial Stage	7.89×10^{-11}	1.06×10^{-10}
1050 – Second Stage	1.58×10^{-11}	4.35×10^{-12}

4.3.4 Characterization of the Oxide Scale

Following oxidation testing, the oxidized samples were characterized by XRD and SEM to confirm the oxides present and verify any evidence of residual transitional phases. Glancing-angle XRD (also known as grazing-incidence XRD) was chosen as the oxide layers formed are quite thin and GAXRD is known to be more sensitive to surface coatings and thin films [4.19]. These results are presented in Figure 4.10. After the oxidation treatment, peaks for the NiAl intermetallic phase (JCPDS # 03-065-4197) as well as the α-Al_2O_3 (JCPDS # 01-071-1123) phase are visible in both the nanostructured and conventional sample, however the conventional sample has a small number of peaks that indicate residual θ-Al_2O_3 (JCPDS # 00-035-0121).

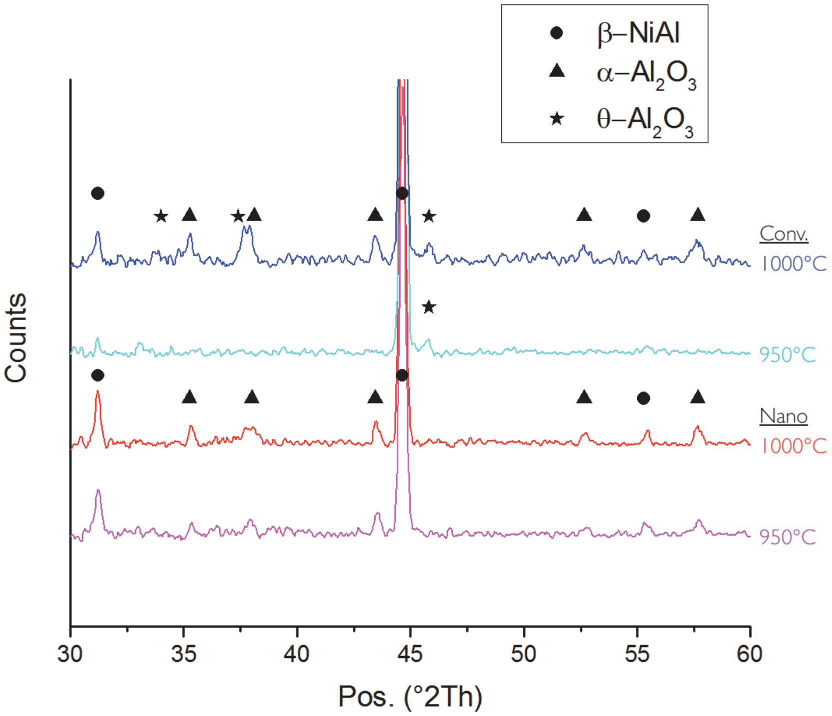

Figure 4.10: GAXRD data for conventional and nanostructured samples after 24 hours oxidation in air at 950 and 1000°C.

To complement this GAXRD data, surface micrographs of the oxidized samples are presented in Figure 4.11 at both low and high magnification. Several previous studies have shown that the evidence of the γ-θ-α transition can also be found in surface morphology of the oxide formed. Typically, in the initial stages of oxidation, the surface will form whiskers that evolve into a highly twinned needle structure that is characteristic of the γ-θ transition; this will in turn evolve into a more blade-like structure that will develop ridges indicating the θ-α transition. The final morphology of α-alumina is a much flatter structure, though some residual blades have been seen in samples that are almost fully transitioned to α-alumina [4.12-4.14, 4.20, 4.21]. The conventional samples in images A, B and C have a blade-like morphology that is typical of θ-alumina [4.12]. Micrographs B and particularly C, for samples oxidized at 1000 and 1050 respectively, do however show the ridge-like structure typical of the transition toward α-alumina [4.20]. In contrast, the micrographs for nanostructured samples, images D, E and F, have a rather different morphology. Figure 4.10-D, corresponding to the nanostructured sample oxidized at 950°C, has some of the residual blades seen in the conventional samples but with a flatter structure with what appear to be underlying ridges. Of greatest interest are images E and F, which show a very flat, interlocking-ridge like structure that is associated with corundum and suggests, along with the XRD data presented earlier, a complete and transition to the corundum structure.

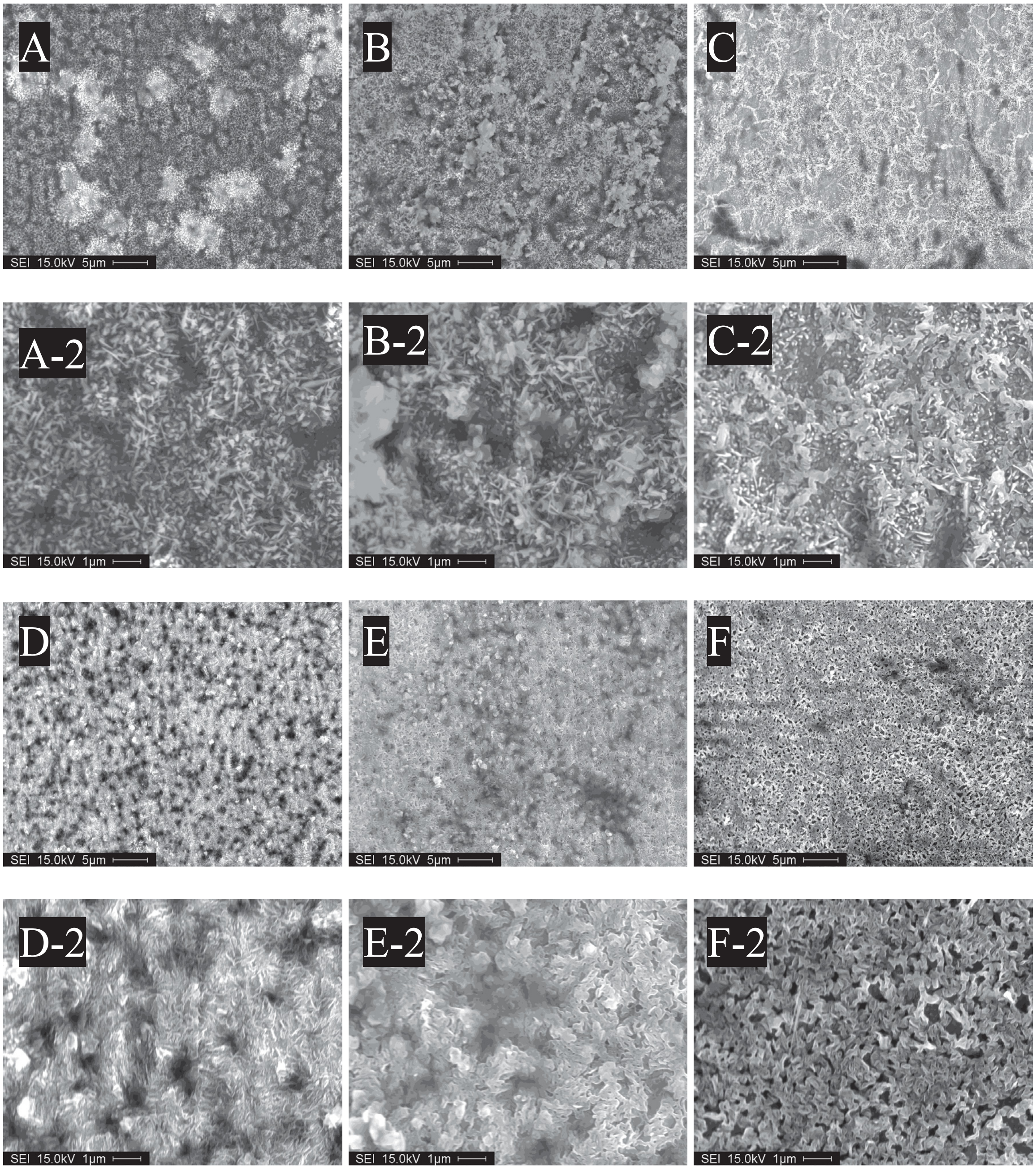

Figure 4.11: Surface micrographs of conventional samples oxidized in air for 24 hours at 950 (A), 1000 (B) and 1050°C (C) as well as nanostructured samples oxidized under corresponding conditions (D, E, F). Higher magnification is denoted by a "-2".

The oxidation testing presented in Figures 6 and 7 supports the idea that nanostructure can improve overall oxidation resistance. Looking first at the oxidation of conventional samples, all conditions show oxidation rates on the order of 10^{-11} $g^2/cm^4/s$ which is somewhat higher than the reference studies, but given the entirely different processing route of the samples presented herein, as well as the higher oxygen partial pressure, this difference is not unexpected. Based on this comparison and the micrographs presented in Figure 4.11, it is believed that these samples have begun transitioning to α-alumina but this transition is far from complete. The oxidation rates presented in Figure 4.7 would therefore correspond to the "θ-line". Looking next at the nanostructured samples, two trends are clear. First nanostructured NiAl samples show significantly lower oxidation rates than their conventional counterparts and second these rates are decreasing with temperature. The micrographs presented in Figure 4.10 and the oxidation rate of 1.65 x 10^{-11} $g^2/cm^4/s$ would indicate that the nanostructured sample oxidized at 950°C is also in the midst of the θ-α transition. However, the samples oxidized at 1000 and 1050°C have the notably lower oxidation rates that, based on Figure 4.7, would indicate that these samples have moved well into the α-transition and this is corroborated by the microstructures in Figure 4.10-E and -F.

4.3.5 In-Situ High Temperature XRD

Previous studies of the MCrAlY system have indicated that the higher grain boundary volume present in a nanostructured sample generates more pathways for aluminum diffusion as well as nucleation points for α-alumina, this consequently allows a more complete transition through the metastable alumina phases after shorter oxidation times or at lower temperature [4.6, 4.7]. While this is a valid point in the case of a two-phase system, in the case of a single-phase system with much higher aluminum concentration, increased grain boundary transport may be relevant but it is likely that other effects are in play. It is believed that the reduction of the high initial strain of the nanostructured NiAl lattice through grain growth and grain boundary movement leads to an earlier transition of the oxide crystal structure. Under high temperature oxidation conditions, the recrystallization and grain growth yields residual stresses at the interface or in the thin film that would catalyze subsequent phase transformation to α-alumina, the most energetically favourable structure.

This earlier phase transformation is apparent in the DSC data presented in Figure 4.8 where the exothermic peak believed to be associated with that θ-α transition occurs at roughly 671°C rather than 829°C seen in the conventional sample. The overall effect is best exemplified in Figure 4.8 and Table 4.2, where the nanostructured sample has an oxidation rate a full order of magnitude higher than the conventional sample in the initial stage, followed by a sharper inflection point that gives way to steady-state oxidation kinetics, that are overall much slower than the conventional sample. The decrease in oxidation kinetics with increasing temperature demonstrated by the nanostructured samples in Figure 4.5 is due to this rapid transition, and earlier passivation, an effect that is also enhanced with temperature. Being more pronounced at 1000 and 1050°C the earlier α-transition results in a decrease in overall oxidation rate for these temperatures.

In order to verify the evolution of the surface strain of the nanostructured sample, an oxidation experiment using in-situ high-temperature XRD was conducted. Conventional and nanostructured samples were oxidized in ambient air under similar ramp conditions to TGA and DSC tests discussed earlier, while XRD patterns were taken at multiple increments from 500 to 1000. The resulting XRD patterns were then used to calculate lattice strain via the Williamson-Hall method [4.22] resulting in a plot of lattice strain versus temperature, presented in Figure 4.12.

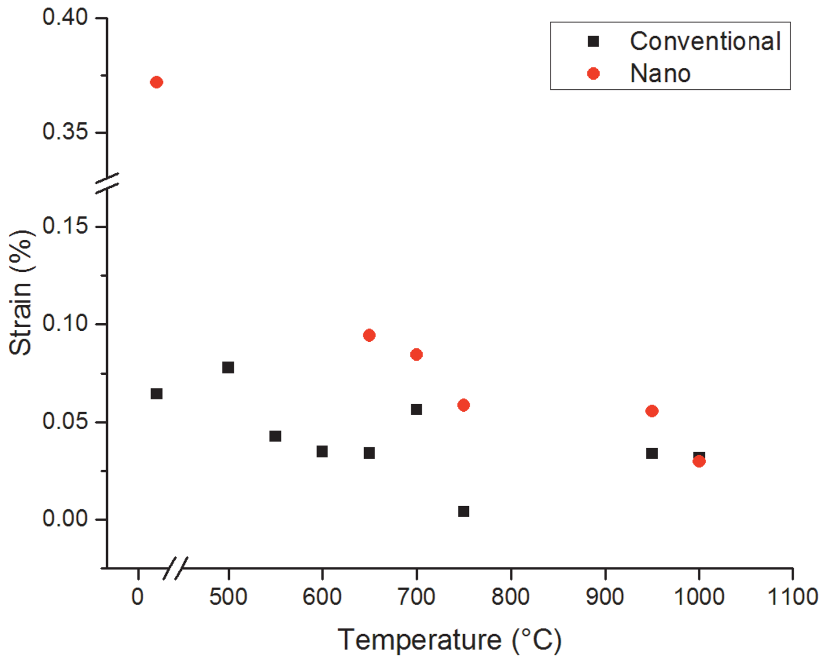

Figure 4.12: Strain as a function of temperature for conventional and nanostructured NiAl samples, calculated via the Williamson-Hall method.

The conventional sample presented in Figure 4.12 has, as expected, very little variation in lattice strain throughout the oxidation test, showing a trend that is essentially a straight line across all temperatures. In contrast the as-sintered nanostructured sample has significantly higher lattice strain that drops quickly with temperature, reaching the stable level seen in the conventional sample in the range of 700 to 800°C. The initial lattice strain of 0.37% is in a similar range though somewhat lower than values found by Kubaski *et al.* for NiAl powders synthesized in planetary and attritor mills under various conditions [4.23]. In the range of 700 to 800°C the minimum grain size of the nanostructured sample is ~150 nm, an increase from the minimum grain size of ~20 nm in the as-sintered nanostructured samples. Joardar *et al.* and have conducted several studies on the thermal stability of mechanically milled NiAl [4.8, 4.24]. In NiAl powder formed by mechanical milling, an exothermic reaction is seen in the range of 300 to 600°C; this reaction is attributed to strain relief through reordering and grain growth of the powder, and that these phenomena occur simultaneously [4.24]. They reported that samples annealed at 600°C demonstrated grain growth from the 10 to 15 nm range up to 51 nm after 4 hours annealing, at which point crystallite size stabilized. Similar grain growth is seen in the present study, but exacerbated due to higher oxidation temperatures. A similar study by Liu *et al.* found an exothermic reaction in the range of 537 to 645°C in milled NiAl powders, attributing this reaction to the release of stored energy introduced by milling [4.25]. It is important to note that both of these studies conducted DSC scans to a maximum of 700°C, and so grain growth at higher temperatures was not studied.

Zeman *et al.* have studied the metastable phase transformations in magnetron sputtered pure Al_2O_3 films, examining phase evolution form amorphous through γ, θ and α-alumina [4.26, 4.27]. They have found that the γ-α transition occurs through a transient θ formation that does not have a significant release of heat. The final transformation to α, in contrast, requires a reconstruction of the oxygen sublattice and is exothermic. They have also found that due to the higher activation energy of the θ-α transition, the α transformation is impeded at lower temperatures [4.26]. Research on the formation of alumina on NiAl single crystals by Lipkin *et al.* indicates that the heterogeneous nucleation and growth of α-alumina within a θ-alumina crystallite matrix results in a volumetric change that induces tensile stresses in the oxide [4.28]. It is noted, however, that compressive stresses can occur from the lateral growth of new oxide at grain boundaries, resulting in a stress gradient in the scale [4.28]. The relief of these stresses induces tearing in the oxide scale that creates channels for formation of new oxide. Finally, a similar but more exhaustive study of alumina formed on several NiAl single crystals of differing orientations at 1100°C by Heuer *et al.* has shown that the in-plain strain in the θ-alumina oxide layer decreases with increasing oxidation time [4.29]. This decrease coincides with the formation and growth of α-alumina over the same time period. Simultaneously, in-plane strain of the NiAl lattice dropped by ~0.1 to ~0.23 %, however it was found that θ-alumina was retained on crystals that demonstrated less strain relief, a similar behaviour to the conventional samples in the present study. In this case it was found that the tensile stresses generated by the θ-α transition, also found in [4.28], will relax with ongoing α-alumina transformation [4.29]. In the present study of a nanostructured substrate experiencing grain growth, further stress accommodation may be possible. Clarke [4.30] has modeled the growth of oxide scales and found, as noted by Lipkin *et al.*, that oxide growth at grain boundaries can induce compressive stresses in the oxide scale, resulting in equilibrating tensile stresses in the metal substrate. Clarke also notes the high growth stresses that occur in alumina scales grown on NiAl at high temperature; possible relaxation processes include several creep mechanisms and plastic deformation (wrinkling). Haslam *et al.* conducted molecular dynamics modeling of grain growth in nanostructured materials and found enhanced creep rates at the onset of grain growth [4.31]. While both of these models would require experimental verification in the NiAl system, the potential for grain growth induced stress accommodation in nanostructured NiAl is clear, be it compressive stress from oxide growth or tensile stress from oxide phase transformation.

It is believed that grain growth and grain boundary movement in the nanostructured sample occurring up to approximately 700°C based on Figure 4.12 and previously reported for NiAl alloys, is providing a catalyzing force to overcome the activation energy of the α-transition, which is typically impeded at lower temperatures [4.26]. Strain relief in the NiAl substrate has been shown to correlate with θ-α transition [4.29], and the decrease in strain in the present study of 0.31% is in a similar range to the ~0.23% reported for single crystals of NiAl. Additionally the correlation between the onset of θ-α transition in the nanostructured sample (671°C) and strain relief in said sample (stabilizing in the ~700°C range) is significant, as is correlation of grain size. In the same temperature range the cryomilled sample reached a stable grain size large enough to remove the effect of grain refinement after stress relaxation. Given these considerations, it is assumed that the strain relief in the nanostructured sample is contributing to an earlier θ-α transition, which in turn results in lower overall oxidation rates for the nanostructured samples when compared to conventional.

4.4 Conclusions

Bulk nanostructured NiAl samples have been obtained through cryomilling of NiAl intermetallic feedstock powder and subsequent sintering via SPS. XRD and TEM analysis indicated dense consolidated samples with a grain size of ~100 nm on average were successfully formed.

Subsequent oxidation testing of conventional grain sized and nanostructured NiAl samples reveals that while the conventional samples have oxidation rates on the order of

10^{-11} $g^2/cm^4/s$ across all tested temperatures, nanostructured samples demonstrate decreasing oxidation rates with temperature, as low as 6.78 x 10^{-13} $g^2/cm^4/s$ for the sample oxidized at 1050°C. This decrease in oxidation rate is attributed to a rapid transition through the metastable aluminum oxide phases, resulting in a stable slow growing α-Al_2O_3 phase earlier in the oxidation tests. XRD, SEM and DSC results are in agreement that this earlier transition is occurring in nanostructured samples.

Finally, in-situ XRD during high-temperature oxidation tests has shown that lattice stain at the surface of the nanostructured samples is substantially higher than conventional, but is rapidly relived during high temperature oxidation. It is believed that the rapid θ-α transition is stimulated by the exothermic strain relief in nanostructured samples, resulting in lower oxidation rates overall.

Acknowledgments

The authors would like to thank the Natural Sciences and Engineering Research Council of Canada and Hydro Quebec for funding this research.

4.5 References

[4.1] S. Bose, *High Temperature Coatings*, Buttersworth Heinemann, Burlington, 2007.

[4.2] J. Bursík, P. Broz, J. Popovic, *Microstructure and phase equilibria in Ni–Al–Cr–Co alloys*, Intermetallics 14 (2006) 1257-1261.

[4.3] H. Peng, H. Guo, R. Yao, J. He, S. Gong, *Improved oxidation resistance and diffusion barrier behaviors of gradient oxide dispersed NiCoCrAlY coatings on superalloy*, Vacuum 85 (2010) 627-633.

[4.4] M. Subanovic, P. Song, E. Wessel, R. Vassen, D. Naumenko, L. Singheiser, W.J. Quadakkers, *Effect of exposure conditions on the oxidation of MCrAlY-bondcoats and lifetime of thermal barrier coatings*, Surface and Coatings Technology 204 (2009) 820-823.

[4.5] L. Ajdelsztajn, J. A. Picas, G. E. Kim, F. L. Bastian, J. Schoenung, V. Provenzano, *Oxidation behavior of HVOF sprayed nanocrystalline NiCrAlY powder*, Materials Science and Engineering A 338 (2002) 33-43.

[4.6] D. Mercier, C. Kaplin, G. Goodall, G. Kim, M. Brochu, *Parameters influencing the oxidation behavior of cryomilled CoNiCrAlY*, Surface and Coatings Technology 205 (2010) 2546-2553.

[4.7] C. Kaplin, M. Brochu, *Effects of water vapor on high temperature oxidation of cryomilled NiCoCrAlY coatings in air and low-SO_2 environments*, Surface and Coatings Technology 205 (2011) 4221-4227.

[4.8] J. Joardar, S. K. Pabi, H.-J. Fecht, B. S. Murty, *Stability of nanocrystalline disordered NiAl synthesized by mechanical alloying*, Philosophical Magazine Letters 82 (2002) 469-475.

[4.9] G.H. Xu, K.F. Zhang, Z.Q. Huang, *The synthesis and characterization of ultrafine grain NiAl intermetallic*, Advanced Powder Technology, Volume 23, Issue 3, May 2012, Pages 366-371.

[4.10] E. Liu, J. Jia, Y. Bai, W. Wang, Y. Gao, *Study on preparation and mechanical property of nanocrystalline NiAl intermetallic*, Materials & Design 53 (2014) 596-601.

[4.11] W. Hu, M. Li, M. Fukumoto, *Preparation and properties of HVOF NiAl nanostructured coatings*, Materials Science and Engineering A 478 (2008) 1-8.

[4.12] M. W. Brumm, H.J. Grabke, *The oxidation behaviour of NiAl-I. Phase transformations in the alumina scale during oxidation of NiAl and NiAl-Cr alloys.* Corrosion Science 33 (1992) 1677-1690.

[4.13] H. J. Grabke, *Oxidation of NiAl and FeAl*, Intermetallics 7 (1999) 1153-1158.

[4.14] J. C. Yang, E. Schumann, I. Levin, M. Ruhle, *Transient Oxidation of NiAl*, Acta Materialia 46 (1998) 2195-2201.

[4.15] K. Wefers, C. Misra, *Oxides and Hydroxides of Aluminum*, Alcoa Technical paper, 1987.

[4.16] J. Milligan, M. Brochu, *Cladding AA7075 with a cryomilled Al–12Si alloy using spark plasma sintering*, Materials Science and Engineering A 578 (2013) 323-330.

[4.17] R. Vintila, A. Charest, R.A.L. Drew, M. Brochu, *Synthesis and consolidation via spark plasma sintering of nanostructured Al-5356/B4C composite*, Materials Science and Engineering A 528 (2011) 4395-4407.

[4.18] B. Pierragi, *Calculations of parabolic reaction rate constants*, Oxidation of Metals 27 (1987) 177-185.

[4.19] B.D. Cullity, *Elements of X-Ray Diffraction*, 2nd Edition, Addison-Wesley, 1978.

[4.20] J. Doychak, J. L. Smialek, T. E. Mitchell, *Transient Oxidation of Single Crystal ß-NiAl*, Metallurgical Transactions 20A (1989) 499.

[4.21] B.A. Pint, J.R. Martin, L.W. Hobbs, *The oxidation mechanism of θ-Al2O3 scales*, Solid State Ionics 78 (1995) 99-107.

[4.22] G. K. Williamson, W. H. Hall, *X-ray line broadening from filed aluminum and wolfram*, Acta Metallurgica 1 (1953) 22-31.

[4.23] E.T. Kubaski, O.M. Cintho, J.L. Antoniassi, H. Kahn, J.D.T. Capocchi, *Obtaining*

NiAl intermetallic compound using different milling devices, Advanced Powder Technology 23 (2012) 667-672.

[4.24] J. Joardar, S.K. Pabi and B.S. Murty, *Milling criteria for the synthesis of nanocrystalline NiAl by mechanical alloying*, Journal of Alloys and Compounds, Volume 429, Issues 1–2, 21 February 2007, Pages 204-210.

[4.25] Z. G. Liu, J. T. Guo, L. L. He, Z. Q. Hu, *Formation of B2 intermetallic NiAl and FaAl by mechanical alloying*, NanoStructured Materials 4 (1994) 787-794.

[4.26] P. Zeman, Š. Zuzjaková, J. Blažek, R. Čerstvý, J. Musil, *Thermally activated transformations in metastable alumina coatings prepared by magnetron sputtering*, Surface & Coatings Technology 240 (2014) 7-13.

[4.27] Š. Zuzjaková, P. Zeman, Š. Kos, *Non-isothermal kinetics of phase transformations in magnetron sputtered alumina films with metastable structure*, Thermochimica Acta 572 (2013) 85-93.

[4.28] D. M. Lipkin, D. R. Clarke, M. Hollatz, M. Bobeth, W. Pompe, *Stress development in alumina scales formed upon oxidation of (111) NiAl single crystals*, Corrosion Science 39 (1997) 231-242.

[4.29] A.H. Heuer, A. Reddy, D.B. Hovis, B. Veal, A. Paulikas, A. Vlad, M. Rühle, *The effect of surface orientation on oxidation-induced growth strains in single crystal NiAl: An in situ synchrotron study*, Scripta Materialia 54 (2006) 1907-1912.

[4.30] D. R. Clarke, *The lateral growth strain accompanying the formation of a thermally grown oxide,* Acta Materialia 51 (2003) 1393-1407.

[4.31] A.J. Haslam, V. Yamakov, D. Moldovan, D. Wolf, S.R. Phillpot, H. Gleiter, *Effects of grain growth on grain-boundary diffusion creep by molecular-dynamics simulation,* Acta Materialia 52 (2004) 1971-1987.

Chapter 5: The effect of grain size on the oxidation of NiCoCrAlY[1]

C. Kaplin and M. Brochu
McGill University
Department of Materials Engineering
3610 University Street, Montreal, QC, H3A 0C5

---

[1] Published: C. Kaplin, M. Brochu, *The effect of grain size on the oxidation of NiCoCrAlY*, Applied Surface Science 301 (2014) 258-263.

[2] Published: C. Kaplin, M. Brochu, *Effects of water vapor on high temperature oxidation*

Preface

Having established the effect of nanostructure on the constituent β-NiAl phase, this chapter investigates the oxidation performance the complete NiCoCrAlY alloy. Cryomilled and conventional bulk NiCoCrAlY samples, consolidated by spark plasma sintering were subjected to isothermal oxidation. Using similar conditions those used in Chapter 4, oxidation kinetics were studied through thermogravimetric analysis and compared to kinetics in NiAl as well as existing studies on MCrAlY.

Abstract

Ultrafine NiCoCrAlY samples have been obtained through cryomilling of NiCoCrAlY feedstock powder and sintering via SPS. These samples have been subjected to isothermal oxidation tests at 950, 1000 and 1050°C. Oxidation rates on the order of 10^{-13} $g^2/cm^4/s$ for samples oxidized at 950°C, 10^{-11} $g^2/cm^4/s$ at 1000°C and 10^{-12} $g^2/cm^4/s$ at 1050°C have been found. In all cases cryomilled samples demonstrate lower overall oxidation rates than their conventional counterparts. Lower overall oxidation rates found in the cryomilled samples are ascribed to an earlier transition trough the metastable alumina phases, resulting in a stable slow growing α-Al_2O_3. Characterization by XRD and SEM corresponds well with this assessment. Lower oxidation rates seen at 1050 than at 1000°C in both conventional and cryomilled samples are the result of a change from oxidation dominated by θ-alumina to oxidation dominated by α-alumina, as the θ-α transition speeds up with increasing temperature. This change in oxidation regime reduces, but does not eliminate, the beneficial impact of smaller grain size on oxidation rate.

5.1 Introduction

The ongoing campaign to increase efficiency in many industrial processes requires materials able to withstand extremely high temperatures and harsh environments. Industries including power generation, petrochemical refining, and aero- and land-based turbines use numerous components that can be exposed to oxidative or corrosive gases at temperatures sometimes exceeding 1000°C [5.1]. Among the most common methods to protect against high temperatures is the thermal barrier coating (TBC). A typical TBC consists of an yttria-partially-stabilized zirconia (YPSZ) top coat and nickel superalloy bond coat, normally of the MCrAlY class of alloys where M = Ni, Co or a combination of both. These alloys have the ability to grow oxide scales that result in good thermal matchup between other coating layers [5.2]. These same oxide scales also produce substantial high temperature corrosion resistance [5.3].

MCrAlY coatings have a two-phase structure consisting of the γ-phase, a solid solution of Ni, Co and Cr and the β-phase, an intermetallic of Ni and Al at 50 at-% each. At some compositions γ'-Ni_3Al strengthening precipitates can also be found. The presence of the β-phase provides a source of aluminum that allows for the growth of Al_2O_3 on the surface of the coating when exposed to oxidative conditions [5.4]. The presence of Co in many of these alloys provides the advantage of increasing the stability of the β-NiAl phase at high temperature [5.1]. The long-term degradation of these coatings is normally caused by faster growing spinel oxides that occur over the thermally grown alumina layer. As a result, there have been a number of publications focusing on improving the oxidation behaviour of MCrAlY alloys [5.5, 5.6] including several that have focused on reducing grain size of the base alloy in order to lower overall oxidation rate [5.7-5.9].

The growth of alumina has been identified as passing through several metastable transition structures: γ-Al_2O_3, δ-Al_2O_3, and θ-Al_2O_3 before eventually transform to the stable corundum α-Al_2O_3 phase [5.10]. The importance of these transformations on oxidation behaviour and coating stability is notable as the transformation from cubic γ to monoclinic β to rhombohedral α each result in an increase in density of over 10% [5.10]. The metastable alumina phases are responsible for an initial transient stage in oxidation while the final corundum structure dictates overall kinetics [5.11]. As a result α-Al_2O_3 is preferred because the slow diffusion of cations through its lattice limits oxygen diffusion and results in a slow growing oxide [5.12, 5.13].

Several studies have focused on grain size modification to improve oxidation performance in MCrAlY alloys. Lou *et al.* have shown that an as-cast K38G superalloy forms a chromia oxide scale when oxidized in air at 1000°C, while the same alloy, when nanostructured, forms an alumina scale under similar conditions [5.14]. The work of Zhang *et al.*, Ajdelsztajn *et al.*, Liu *et al.*, and Tang *et al.* have all shown that nanostructured MCrAlY coatings show improved oxidation behaviour [5.7, 5.15-5.17]. More recently, Todde *et al.* demonstrated in a study of cryomilling in CoNiCrAlY samples consolidated by spark plasma sintering, that the exclusive formation of an α-alumina oxide scale is promoted by cryomilling [5.18]. Citing several of the above-listed studies, Mercier *et al.* have shown that cryomilling can improve the distribution of aluminum throughout the MCrAlY sample while also reducing the distance required for lattice diffusion and increasing the number of pathways for grain boundary diffusion to the surface [5.8]. In so doing, the effective competition between Al-containing β-NiAl grains that will form alumina in the initial stages, and the γ-grains that require lattice diffusion of Al to oxidize, is reduced. This results in uniform and rapid transport of aluminum to the surface. A recent study by Kaplin and Brochu has also indicated the possibility that grain size reduction promotes an earlier transition through the metastable alumina phases, and this in turn results in improved oxidation performance [5.9].

The purpose of this study is to investigate the oxidation behaviour of conventional and cryomilled NiCoCrAlY samples consolidated via Spark Plasma Sintering (SPS) in order to better understand the effect of grain size on the oxidation of this system. Cryomilling has been chosen as the method for grain size reduction in the NiCoCrAlY precursor powder, while SPS has been selected for sintering, as it is a promising technique for the consolidation of bulk nanostructured samples [5.19, 5.20]. Particular emphasis will be placed on transition aluminum oxides through the study of oxidation kinetics via thermogravimetric analysis, and of morphology via scanning electron microscopy and x-ray diffraction.

5.2 Experimental Procedures

NiCoCrAlY samples were produced from commercially available gas atomized Ni-130/Ni-191 powder from Praxair Surface Technologies. Chemical composition of the powder is presented in Table 5.1. Part of this powder was cryomilled for 16 hours in a Union Process 1-D attrition mill at 180 rpm with stainless steel grinding media, with a ball to powder ratio of 32:1 and 0.2% stearic acid added as a surfactant to prevent coating the balls and interior of the milling vessel. Liquid nitrogen was continuously added to the vessel.

Spark plasma sintering was used to consolidate the conventional and cryomilled powder using a Thermal Technologies 10-3 sintering press. In the case of conventional samples, sintering was conducted under vacuum using a 200°C/minute ramp to 1100°C, held for 7 minutes and cooled to ambient temperature. Cryomilled samples were heated at 250°C/minute to 1100°C, held for 10 seconds and finally cooled to ambient temperature. Density was measured using the Archimedes principle and grain size was direct measured via SEM using the intersecting line method averaging at least 100 grains as well as via X-Ray Diffraction using the Scherrer Equation [5.21].

Table 5.1: Chemical composition of the NiCoCrAlY powder

Alloy Composition (Mass %)				
Ni	Co	Cr	Al	Y
46.55	23	17	13	0.45

Isothermal Oxidation testing was conducted in a Netsch STA 449 F3 Jupiter DT-TGA with coincident Thermogravimetric Analysis (TGA) and Dynamic Scanning Calorimetry (DSC). Samples were cut to cubes of approximately 3mm x 3mm x 3mm and ground to 1200 grit on all surfaces prior to oxidation testing. These samples were heated in the TGA at 10°C/minute in synthetic air up to 950, 1000 and 1050°C, held at said temperature for 24 hours and cooled to ambient temperature. Parabolic rate constants were calculated using the method developed by Pierragi [5.11]. X-Ray Diffraction (XRD) patterns were acquired using a Bruker D8 Discover XRD. Standard XRD and Glancing-Angle X-Ray Diffraction (GAXRD) patterns were obtained using a Cu source and Vantec-5000 2D detector. The GAXRD scans were conducted with a 2° incident angle. In all cases phase identification was completed using X'Pert HighScore software.

Scanning electron microscope (SEM) observations were carried out on a Philips XL-30 FE-SEM with EDAX EDS.

5.3 Results & Discussion

5.3.1 Cryomilling and Consolidation

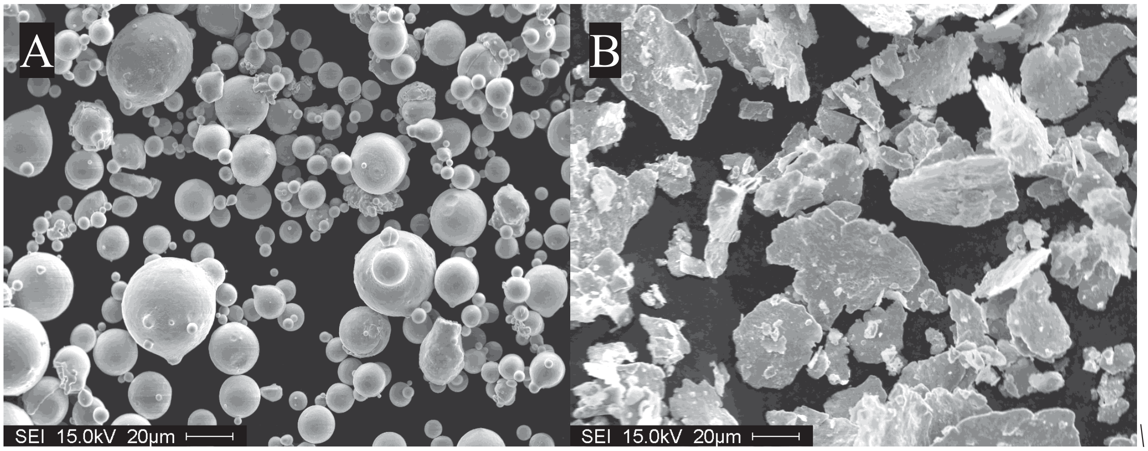

Figure 5.1: SEM images of as-received NiCoCrAlY powder (A) and cryomilled powder (B).

SEM images of the NiCoCrAlY powder before and after cryomilling can be found in Figure 5.1. The flattened, flaky morphology of the cryomilled powder is typical of milled powders and typically indicates a reduction in grain size. The same milling parameters have been previously used to successfully nanostructure NiCoCrAlY powder [5.22]. Figure 5.2 presents XRD patters of both powders. The conventional powder has the expected γ and β peaks, JCPDS #'s 03-065-2865 and 03-065-4197 respectively, while the milled powder has only a single broad peak indicating that the β-NiAl phase has dissolved into γ and that grain size had been notably reduced.

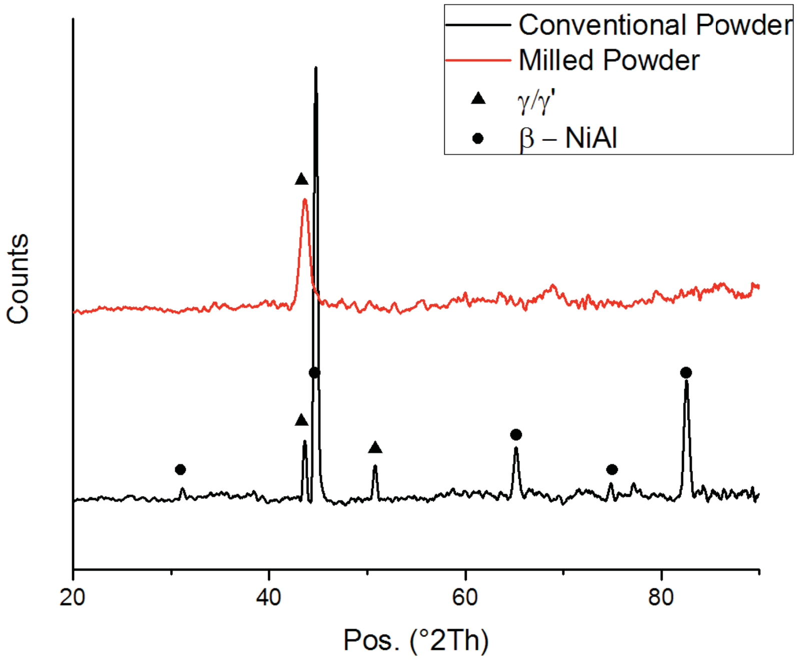

Figure 5.2: XRD patterns for conventional and cryomilled NiCoCrAlY powder.

Cross-sectional images obtained by SEM of SPS-consolidated conventional and cryomilled samples are presented in Figure 5.3 and clearly show the difference in grain size of the consolidated samples. The conventional sample has a grain size of approximately 1.2 μm, while the milled consolidated sample has a grain size of approximately 150 nm measured via SEM and 109 nm according to XRD analysis using the Scherrer Equation [5.21]. Conventional samples were measured at over 99% theoretical density post-consolidation while ultrafine samples were over 96% theoretical density, based on a calculated theoretical density of 7.2 g/cm^3.

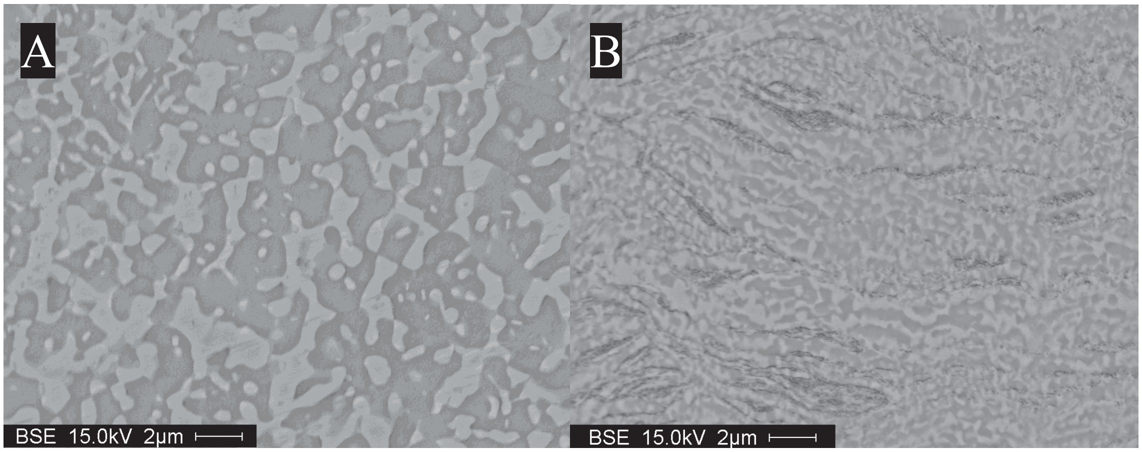

Figure 5.3: Cross-sectional SEM images of consolidated conventional (A) and ultrafine (B) NiCoCrAlY samples.

5.3.2 Characterization of Oxides Formed

The consolidated conventional and cryomilled NiCoCrAlY samples were subjected to oxidation testing and subsequent characterization. Figure 5.4 presents GAXRD patterns obtained from scans of conventional and cryomilled samples after oxidation at various temperatures for 24 hours in air. In all cases the primary and secondary peaks for the γ/γ' phase are present (JCPDS # 03-065-2865 and 03-65-6613), though with less intensity than typically expected, while the β-NiAl phase is not detected. This is due in part to the surface-sensitive nature of GAXRD, resulting in reduced interaction volume and subsequent reduced intensity of "sub-surface" phases [5.21], and also due to depletion of the β phase near the surface during oxidation testing. Of greater interest, however, are the oxide peaks. In both the conventional and cryomilled samples, clear peaks of α-alumina can be identified (JCPDS # 01-071-1123), indicating that after 24 hours of oxidation the transition to corundum is well underway for all samples tested. In the case of the conventional samples, θ-alumina peaks are also visible at all oxidation temperatures (JCPDS # 00-035-0121), which would imply that while the metastable alumina transition is well under way, in the case of conventional NiCoCrAlY it has not yet completed. The cryomilled sample oxidized at 950°C shows peaks of θ-alumina similar to its conventional grain sized counterpart; however, the cryomilled sample oxidized at 1000°C has only one residual peak that is likely θ-alumina, while the sample oxidized at 1050°C has none. This XRD result is evidence that the cryomilled samples have been able to complete the θ-α transition at higher temperatures after 24 hours whereas the conventional samples have not. In both the conventional and cryomilled samples oxidized at 1050°C spinel peaks (JCPDS # 00-010-0339) can be seen though their intensity is notably higher in the conventional sample.

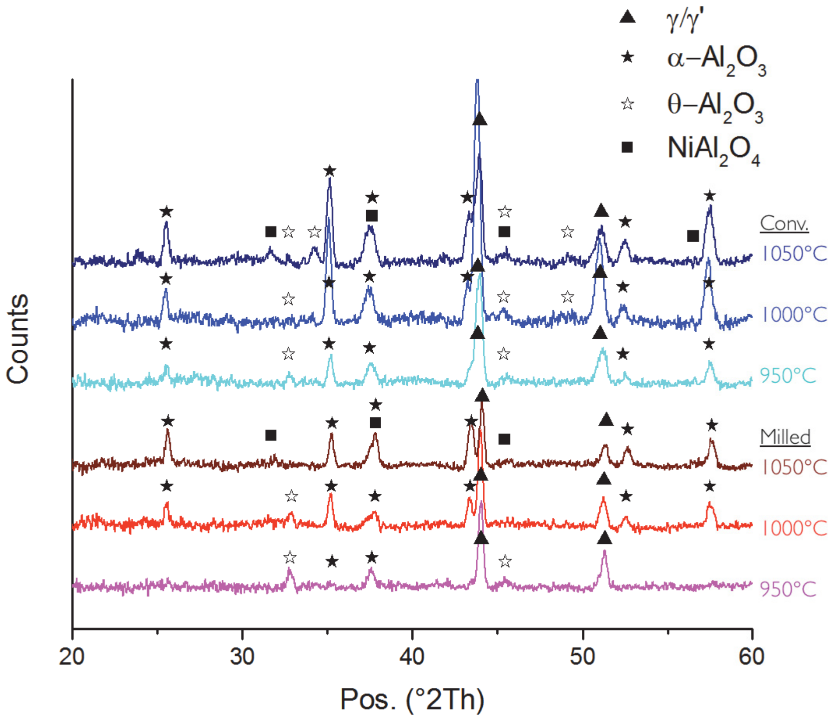

Figure 5.4: GAXRD data for conventional and cryomilled samples after 24 hours oxidation in air at 950 and 1000°C.

Further verification of the surface oxides present has also been conducted via SEM and is presented in Figure 5.5 under both high and low magnification for all testing conditions. Figures 5-A, -B and -C show the surface oxides formed on conventional NiCoCrAlY samples and all three demonstrate the classic blade-like morphology typical of θ-alumina [5.12, 5.23, 5.24]. The flattening of this blade-structure, seen most clearly in Figure 5.5-C-2 is indicative of the ongoing transition to α-alumina that is expected based on the previous XRD results. A similar trend can be seen in Figures 5 D, E and F, showing the oxidized surface of the cryomilled samples. In this case the blade-like structure seen on the conventional samples is repeated on the sample oxidized at 950°C and is somewhat less apparent on the sample oxidized at 1000°C. Interestingly, while a very small amount of blade-structure can be seen in Figure 5.5-F-2, the dominant surface microstructure for the cryomilled sample oxidized at 1050°C is decidedly different from the others presented and corresponds much more with the flattened ridge structure associated with α-alumina [5.23].

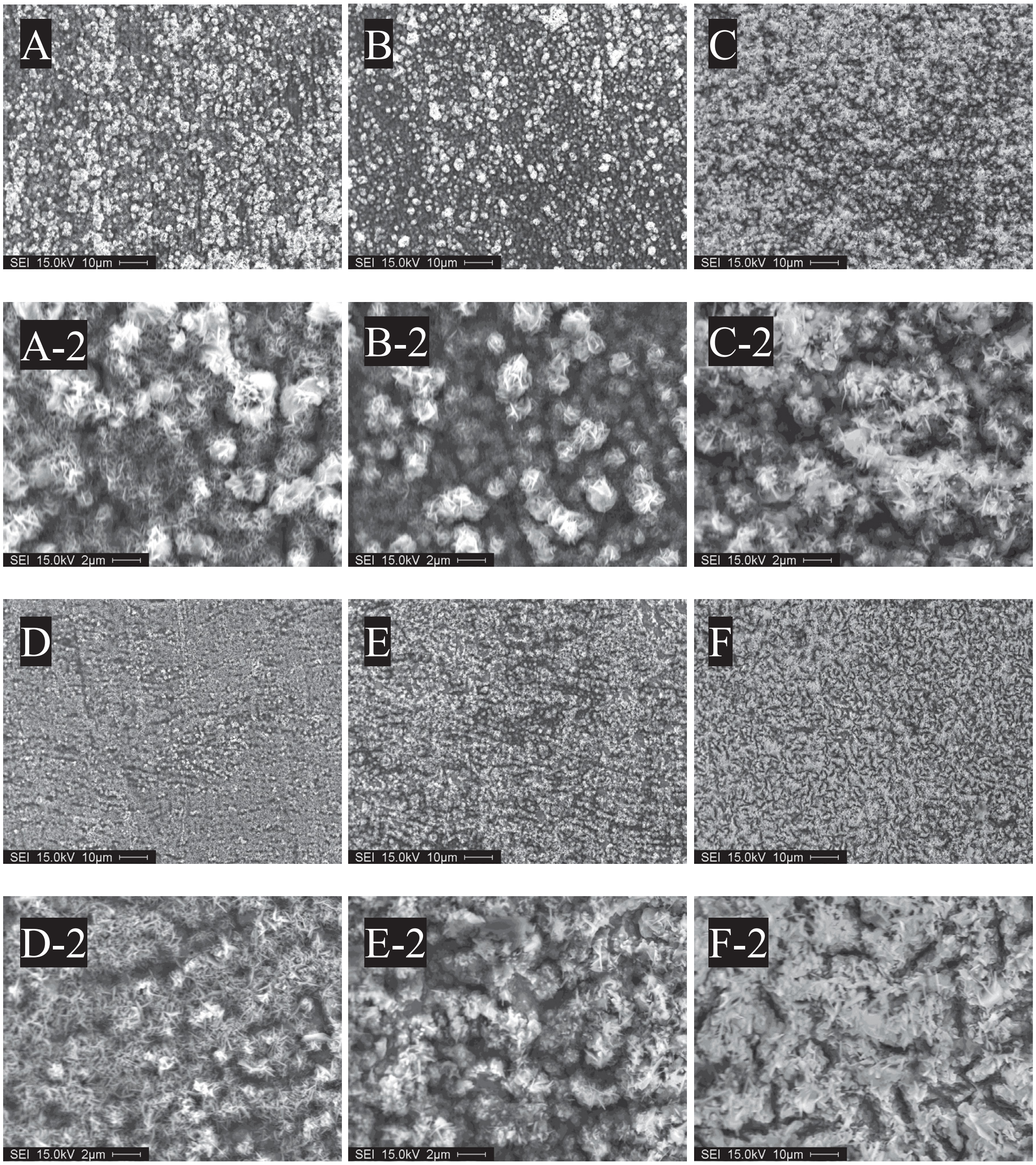

Figure 5.5: Surface micrographs of conventional samples oxidized in air for 24 hours at 950 (A), 1000 (B) and 1050 (C) as well as ultrafine samples oxidized under corresponding conditions (D, E, F). Higher magnification is denoted by a "-2".

5.3.3 Oxidation Kinetics

TGA data from oxidation testing has been presented in Figure 5.6. It is clear from the data presented that at all tested temperatures, after 24 hours of oxidation in air, the cryomilled samples show less overall mass gain than the conventional samples. Examining the parabolic rate constants calculated from said data, presented in the upper section of Table 5.2, reveals that at each temperature the oxidation rate for conventional and cryomilled NiCoCrAlY samples is on the same order of magnitude. Oxidation rates are, however, lower for the cryomilled samples though the difference between cryomilled and conventional shrinks with increasing temperature. It is also of note that, while an expected increase in oxidation rate is seen from 950 to 1000°C, a drop in oxidation rate is seen from 1000 to 1050°C for both sample categories.

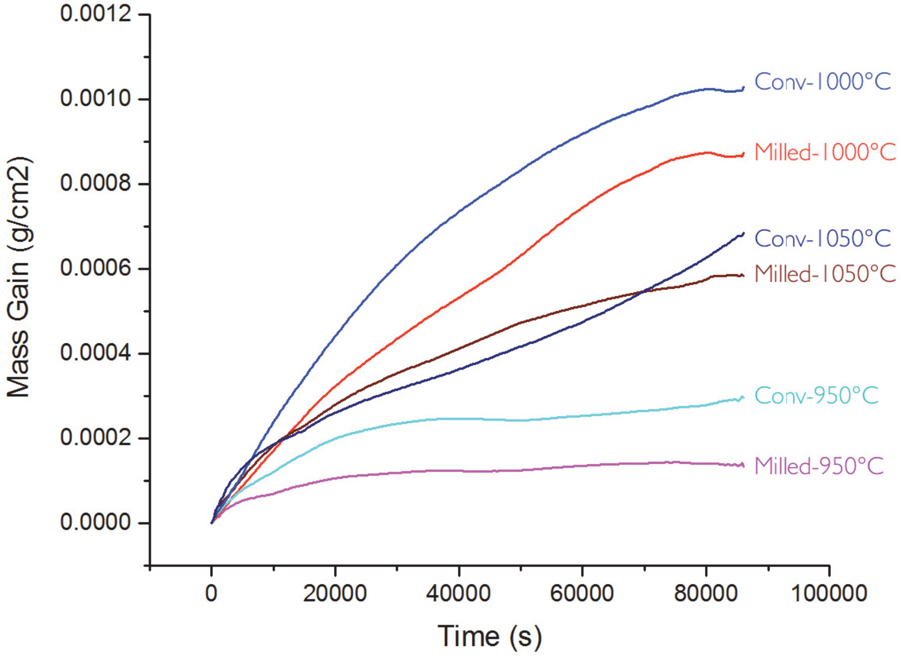

Figure 5.6: TGA data for conventional and cryomilled samples oxidized for 24 hours in air at 950, 1000 and 1050°C.

The θ-α transition is known to be a time-temperature dependent process; Brumm and Grabke have shown that for NiAl samples oxidized in air, at 900°C the transition to α can be measured in hundreds of hours while at 1100°C the transition to α is too short be measurable by TGA, with transition times decreasing as expected between these two temperatures [5.12]. It is expected therefore that any NiAl samples oxidized at 950, 1000 and 1050°C for equal times would show an effective evolution from θ towards α-alumina. In the case of cryomilled samples, this time-temperature dependent transition appears accelerated, indicating that cryomilled samples are in the process of converting to α-alumina more rapidly than their conventional counterparts. In so doing, cryomilled samples have a relatively larger portion of corundum throughout the oxide, acting as a diffusion block and in turn lowering overall oxidation rates. This accelerated transition stage has been shown in [5.9] to reduce overall oxidation rates for nanostructured HVOF-sprayed NiCoCrAlY coatings. Additionally, grain size reduction also decreases the distance required for lattice diffusion of Al through the aluminum-poor γ-phase, ensuring a consistent oxide layer necessary to passivate further oxidation.

In Table 5.2 the parabolic rate constants found in the present study are also compared to a number of other recent studies on the oxidation of MCrAlY class alloys. A previous study [5.9] using the same cryomilled powder to produce HVOF coatings found an oxidation rate at 1000°C slightly higher but on the same order of magnitude as the present study. This is expected given the HVOF samples were not ground prior to oxidation, and several studies have shown that surface treatment serves to decrease oxidation rate, which is reflected in the oxidation rates found in [5.8] and [5.28]. The study by Peng *et al.* [5.25] has found oxidation rates on the order of 10^{-13} $g^2/cm^4/s$ for different EBPVD deposited NiCoCrAlY coatings, despite an oxidation temperature of 1100°C which is higher than any of the temperatures used in the present study. This result could correlate with the drop in oxidation rate seen from 1000 to 1050°C in the present study but more data would be required to make a definite conclusion. Several studies on CoNiCrAlY and NiCrAlY have also been included and indicate oxidation rates on the same order of magnitude as the present study, but these should be used as a rough comparison only, given the varying levels of aluminum in the alloys studied [5.8, 5.26-5.28].

Table 5.2: Parabolic rate constants from various recent oxidation studies of MCrAlY alloys.

Author	Material	Processing	Temp (°C)	k_p ($g^2/cm^4/s$)
Present Work	NiCoCrAlY	SPS + ground	950	7.64×10^{-13}
			1000	1.83×10^{-11}
			1050	5.18×10^{-12}
	NiCoCrAlY	Cryomilled + SPS + ground	950	1.71×10^{-13}
			1000	1.38×10^{-11}
			1050	4.85×10^{-12}
Kaplin [5.9]	NiCoCrAlY	Cryomilled + HVOF	1000	2.27×10^{-11}
Peng [5.25]	NiCoCrAlY	PA-EBPVD	1100	2.9×10^{-12}
		EBPVD	1100	8.0×10^{-13}
Mercier [5.8]	CoNiCrAlY	Cryomilled + HVOF	950	1.96×10^{-12}
			1000	4.88×10^{-12}
			1050	4.97×10^{-12}
		Cryomilled + HVOF + ground	950	7.19×10^{-13}
			1000	7.41×10^{-13}
			1050	1.28×10^{-12}
Brandl [5.26]	CoNiCrAlY	HVOF	950	1.16×10^{-13}
		HVOF + ground	950	6.71×10^{-13}
Belzunce [5.27]	CoNiCrAlY	HFPD	1000	3.34×10^{-12}
Li [5.28]	NiCrAlY	HVOF	1050	4.98×10^{-12}
		HVOF + ground	1050	2.29×10^{-12}
		HVOF + shot-peened	1050	3.09×10^{-12}

The parabolic rate constants presented in Table 5.2 along with the TGA data in Figure 5.6 show that oxidation rate increases from 950 to 1000°C as is normally the case in high temperature oxidation; however, from 1000 to 1050°C the oxidation rate drops for both conventional and cryomilled samples. This would indicate a shift in oxidation behaviour that has previously been identified in [5.12]. The oxidation of aluminum, as previously discussed, transitions through γ-θ-α with the early stages of oxidation being dominated by a different metastable phase depending on temperature. In the time frame of the current study, 24 hours, the dominant oxide from 700 to roughly 900°C should be γ-alumina [5.12, 5.23], from around 850°C to around 1000°C the γ-θ transition is increasingly quick and θ-alumina becomes the dominant oxide [5.12, 5.23]. Finally at around 1000°C the θ-α transition begins to speed up and the dominant oxide is α-alumina up to 1100, at which point the θ-α transition is immeasurably fast [5.12]. It is important to note that the evolution of the dominant oxide phase does not imply a complete transition to α-alumina, but simply that this ongoing transition has the greatest effect on oxidation kinetics during the time frame in question. Based on this, it is clear that between 1000 and 1050°C a shift in oxidation behaviour can be expected and is responsible for the drop in overall oxidation rate for both the conventional and cryomilled samples. This being said, the conventional sample oxidized at 1050°C does still show residual θ-alumina and a slightly slower oxidation rate (5.18×10^{-12} $g^2/cm^4/s$) than the cryomilled samples (4.85×10^{-12} $g^2/cm^4/s$). Interestingly and unsurprisingly, it would appear the benefit of reduced grain size in terms of oxidation rate is less pronounced at 1050°C than at 950 or 1000°C; in essence the time-temperature dependency of the θ-α transition is catching up with the benefits of reduced grain size and closing the gap in oxidation rate between the conventional and cryomilled samples. It is believed that at even higher temperatures the effect of reduced grain size would be negated and oxidation rates will be effectively equal while also lower overall. Rates found by Peng *et al.* for two types of EBPVD NiCoCrAlY samples oxidized at 1100°C (2.9 x 10^{-12} and 8.0 x 10^{-13} $g^2/cm^4/s$) lend some weight to this concept.

5.4 Conclusions

Ultrafine NiCoCrAlY samples have been obtained through cryomilling of NiCoCrAlY feedstock powder and sintering via SPS. Subsequent oxidation testing of conventional grain sized and cryomilled NiCoCrAlY samples reveals oxidation rates on the order of 10^{-13} $g^2/cm^4/s$ for samples oxidized at 950°C, 10^{-11} $g^2/cm^4/s$ at 1000°C and 10^{-12} $g^2/cm^4/s$ at 1050°C. In all cases cryomilled samples demonstrate lower overall oxidation rates than their conventional counterparts. The reduced oxidation rates for cryomilled samples are attributed to an earlier transition trough the metastable alumina phases, resulting in a stable slow growing α-Al_2O_3. XRD and SEM results are in agreement that this earlier transition is occurring and resulting in lower oxidation rates for the cryomilled samples

The drop in oxidation rate from 1000 to 1050°C is attributed to a change from oxidation dominated by θ-alumina to oxidation dominated by α-alumina, as the θ-α transition speeds up with increasing temperature. This has the coincident effect of reducing, but not negating, the beneficial impact of grain size reduction on oxidation rate.

Acknowledgments

The authors would like to thank the Natural Sciences and Engineering Research Council of Canada and Hydro-Quebec for funding this research, as well as Dr. Manas

Paliwal, Mr. Saikat Chatterjee and Prof. In-Ho Jung for their help with thermogravimetric analysis.

5.5 References

[5.1] S. Bose, *High Temperature Coatings*, Buttersworth Heinemann, Burlington, 2007.

[5.2] C. G. Levi, E. Sommer, S. G. Terry, A. Catanoiu, M. Rühle, *Alumina grown during deposition of thermal barrier coatings on NiCrAlY*, Journal of the American Ceramic Society 86 (2003) 676-685.

[5.3] Q. M. Wang, Y. N. Wu, P. L. Ke, H. T. Cao, J. Gong, C. Sun, L. S. Wen, *Hot corrosion behavior of AIP NiCoCrAlY(SiB) coatings on nickel base superalloys*, Surface and Coatings Technology 186 (2004) 389-397.

[5.4] J. Bursík, P. Broz, J. Popovic, *Microstructure and phase equilibria in Ni–Al–Cr–Co alloys*, Intermetallics 14 (2006) 1257-1261.

[5.5] H. Peng, H. Guo, R. Yao, J. He, S. Gong, *Improved oxidation resistance and diffusion barrier behaviors of gradient oxide dispersed NiCoCrAlY coatings on superalloy*, Vacuum 85 (2010) 627-633.

[5.6] M. Subanovic, P. Song, E. Wessel, R. Vassen, D. Naumenko, L. Singheiser, W.J. Quadakkers, *Effect of exposure conditions on the oxidation of MCrAlY-bondcoats and lifetime of thermal barrier coatings*, Surface and Coatings Technology 204 (2009) 820-823.

[5.7] L. Ajdelsztajn, J. A. Picas, G. E. Kim, F. L. Bastian, J. Schoenung, V. Provenzano, *Oxidation behavior of HVOF sprayed nanocrystalline NiCrAlY powder*, Materials Science and Engineering A 338 (2002) 33-43.

[5.8] D. Mercier, C. Kaplin, G. Goodall, G. Kim, M. Brochu, *Parameters influencing the oxidation behavior of cryomilled CoNiCrAlY*, Surface and Coatings Technology 205 (2010) 2546-2553.

[5.9] C. Kaplin, M. Brochu, *Effects of water vapor on high temperature oxidation of cryomilled NiCoCrAlY coatings in air and low-SO_2 environments*, Surface and Coatings Technology 205 (2011) 4221-4227.

[5.10] K. Wefers, C. Misra, *Oxides and Hydroxides of Aluminum*, Alcoa Technical paper, 1987.

[5.11] B. Pierragi, *Calculations of parabolic reaction rate constants*, Oxidation of Metals 27 (1987) 177-185.

[5.12] M. W. Brumm, H. J. Grabke, *The oxidation behavior of NiAl - I. Phase transformations in the alumina scale during oxidation of NiAl and NiAl-Cr alloys*, Corrosion Science 33 (1992) 1677-1690.

[5.13] A.G. Evans, D.R. Mumm, J.W. Hutchinson, G.H. Meier, F.S. Pettit, *Mechanisms controlling the durability of thermal barrier coatings,* Progress in Materials Science 46 (20010 505-553.

[5.14] H. Lou, F. Wang, S. Zhu, B. Xia, L. Zhang, *Oxide formation of K38G superalloy and its sputtered micrograined coating,* Surface and Coatings Technology 63 (1994) 105-114.

[5.15] Q. Zhang, C.-J. Li, C.-X. Li, G.-J. Yang, S.-C. Lui, *Study of oxidation behavior of nanostructured NiCrAlY bond coatings deposited by cold spraying*, Surface and Coatings Technology 202 (2008) 3378-3384.

[5.16] Z. Liu, W. Gao, K. L. Dahm, F. Wang, *Oxidation behaviour of sputter-deposited Ni–Cr–Al micro-crystalline coatings,* Acta Materialia 46 (1998) 1691-1700.

[5.17] F. Tang, L. Ajdelsztajn, J.M. Schoenung, *Influence of Cryomilling on the Morphology and Composition of the Oxide Scales Formed on HVOF CoNiCrAlY Coatings*, Oxidation of Metals 61 (2004) 219-238.

[5.18] S. Todde, R. Licheri, R. Orru, G. Cao, *Spark plasma sintering processing for the evaluation of cryomilled CoNiCrAlY alloys for high temperature applications in oxidizing environment,* Chemical Engineering Journal 200-202 (2012) 68-80.

[5.19] J. Milligan, M. Brochu, *Cladding AA7075 with a cryomilled Al–12Si alloy using spark plasma sintering*, Materials Science and Engineering A 578 (2013) 323-330.

[5.20] R. Vintila, A. Charest, R.A.L. Drew, M. Brochu, *Synthesis and consolidation via spark plasma sintering of nanostructured Al-5356/B4C composite*, Materials Science and Engineering A 528 (2011) 4395-4407.

[5.21] B. D. Cullity, Elements of X-Ray Diffraction, 2nd edition, Addison-Wesley, Reading, Massachusetts, 1978.

[5.22] D. Mercier, B. D. Gauntt, M. Brochu, *Thermal stability and oxidation behavior of nanostructured NiCoCrAlY coatings*, Surface and Coatings Technology 205 (2011) 4162-4168.

[5.23] J. Doychak, J. L. Smialek, T. E. Mitchell, *Transient Oxidation of Single Crystal ß-NiAl*, Metallurgical Transactions 20A (1989) 499.

[5.24] B.A. Pint, J.R. Martin, L.W. Hobbs, *The oxidation mechanism of θ-Al2O3 scales*, Solid State Ionics 78 (1995) 99-107.

[5.25] H. Peng, H. Guo, J. He, S. Gong, *Microscale lamellar NiCoCrAlY coating with improved oxidation resistanc*e, Surface & Coatings Technology 207 (2012) 110-116.

[5.26] W. Brandl, G. Marginean, D. Maghet, D. Utu, *Effects of specimen treatment and surface preparation on the isothermal oxidation behaviour of the HVOF-sprayed MCrAlY coatings,* Surface and Coatings Technology 188-189 (2004) 20-26.

[5.27] F.J Belzunce, V Higuera, S Poveda, *High temperature oxidation of HFPD thermal-sprayed MCrAlY coatings,* Materials Science and Engineering A 297 (2001) 162-167.

[5.28] L.-Y.Ni, Z.-L.Wu, C.-G. Zhou, *Effects of surface modification on isothermal oxidation behaviour of HVOF-sprayed NiCrAlY coatings*, Progress in Natural Science: Materials International 21 (2011) 173-179.

Chapter 6: Effects of water vapour on high temperature oxidation of cryomilled NiCoCrAlY coatings in air and low-SO_2 environments[2]

C. Kaplin and M. Brochu
McGill University
Department of Materials Engineering
3610 University Street, Montreal, QC, H3A 0C5

---

[2] Published: C. Kaplin, M. Brochu, *Effects of water vapor on high temperature oxidation of cryomilled NiCoCrAlY coatings in air and low-*SO_2 *environments*, Surface and Coatings Technology 205 (2011) 4221-4227.

Preface

After investigating the ideal, isothermal oxidation kinetics of NiCoCrAlY, it is of interest to extend this investigation to more realistic industrial conditions. First, the effect of environment on nanostructured HVOF-deposited NiCoCrAlY coatings was explored. The coatings were subjected to isothermal oxidation in environments designed to mimic the conditions in an oil refinery boiler, containing SO_2 and varying levels of water vapour and the ensuing differences in oxidation rate and oxide morphology were explored.

Abstract

Nanostructured NiCoCrAlY coatings were obtained through cryomilling and subsequent HVOF-spraying of the nanostructured powder onto copper substrates, followed by leaching of the Cu to obtain freestanding coatings. Oxidation tests in both air and an environment bearing 0.5% SO_2 with water vapour levels varying from 0 to 8% were conducted for 24 and 48 hours at 1000°C. It has been found that the oxides formed under all conditions are alumina followed by a spinel phase consisting primarily of cobalt aluminum oxide. In both air and the SO_2 environment an increase in total mass gain was seen up to 4% water vapour, followed by a decrease at 6 and 8%. This behaviour is attributed to an extension of the transient oxidation stage, resulting first in a variation in scale thickness through increased spinel growth and second in a rise in internal oxidation caused by increased oxygen transport through the scale in the presence of water vapour. It would appear that above 4% water vapour the thickened spinel is able to compensate for alumina loss and create a diffusion barrier to internal oxidation, once again reducing mass gain.

6.1 Introduction

The petrochemical industry can be a maintenance-intensive business due to various extreme conditions presented by the extraction and refining processes [6.1]. Corrosion in particular can be detrimental to many areas of the refinery and corrosion control can often account for 60% to 70% of a plant maintenance budget [6.2]. Sulphur is evolved from the refining process and is present in effluent gases as H_2S, H_2SO_4 and notably SO_2. Combined with the high temperatures and presence of water vapour in boilers and other components, a significant maintenance issue arises. Current methods for dealing with corrosion include constant monitoring of equipment and use of corrosion resistant bulk materials or coatings [6.2].

One such coating that has been garnering interest is the MCrAlY system, NiCoCrAlY in particular. MCrAlY coating are typically used as the bond coat in a thermal barrier coating system because of their ability to grow oxide scales resulting in good thermal matchup between other coating layers [6.3]. These same oxide scales also produce substantial high temperature corrosion resistance [6.4]. Consequently NiCoCrAlY has been proposed as a stand-alone coating for certain hot spot or high-corrosion/oxidation applications including key areas in oil refinery boilers.

NiCoCrAlY and MCrAlY's generally form a 2-phase structure of γ, a solid solution of Ni, Co and Cr, and β (NiAl), an aluminum-rich phase that feeds the oxide layer [6.5]. Depending on concentration, there is the possibility of a third γ' phase, coherent precipitates of Ni_3Al that improve mechanical properties, although these precipitates are known to dissolve in the range of 800 to 950°C [6.6, 6.7]. Upon exposure to an oxidative environment at high temperature these alloys form an Al_2O_3 scale, seeded by the β phase, followed by a mixed oxide layer that can contain Cr_2O_3, $CoAl_2O_4$, $NiAl_2O_4$, NiO and any number of other mixed oxides depending on the initial composition and microstructure of the MCrAlY. The formation of a dense, single-layer alumina scale is desirable for all applications.

Research to date has been primarily focused on oxidation behaviour of NiCoCrAlY, however there have been only a small number of studies in environments bearing water vapour or sulphur. Leyens *et al.* studied the effect of a range of H_2/H_2O atmospheres on the oxidation of an electron-beam physical vapour deposited NiCoCrAlY coating heat treated at 1100°C and found that the presence of water vapour led to an increase of up to 25% in total mass gain over 28 hours of oxidation at 1080 and 1100°C [6.8]. Similar results were found by Zhou *et al.* in the testing of a NiCrAlY coating deposited by low pressure plasma spray; in this case 50% greater mass gain at 100 hours and 100% greater mass gain at 400 hours were found with 5% water vapour as opposed to dry air at 1050°C [6.9]. A review by Saunders *et al.* of oxidation in atmospheres containing water vapour found that across a number of studies MCrAlY's sometimes show an increase in oxidation rate due to the presence of water vapour, but in some cases did not form alumina at all. In general it was found that the effect of water vapour was more pronounced in the initial stages of oxidation as water vapour has a greater effect on the stability of transient alumina phases as opposed to the diffusion processes in an established, protective alumina layer [6.10]. Most recently, Subanovic *et al.* studied the effects of H_2/H_2O vapour systems on NiCoCrAlY, which resulted in the formation of large blisters and internal oxidation of the coating [6.11]. Finally Godlewska *et al.* have studied the effect of NiCoCrAlY exposure to various H_2/H_2S pressures at high temperature [6.12]. In this case the coating evolved a sulphide scale rather than an oxide scale but otherwise followed similar, although faster, growth kinetics. To date no studies have been performed in gaseous SO_2-bearing environments or on combined oxidation and sulfidation of MCrAlY's.

Nanostructuring is thought to have a significant effect on the oxidation of MCrAlY's. Generally speaking, nanostructured coatings are thought to produce a more consistent and better-adhered alumina layer than their conventional counterparts [6.13, 6.14]. This is due to increased grain boundary area allowing for greater Al diffusion [6.13] to the scale and the formation of small amounts of aluminum oxide within the cryomilled powder and subsequent coating [6.15]. These oxides give nucleating points for a denser alumina scale. Mercier *et al.* have found that nanostructuring speeds up the transition from θ-Al_2O_3 to α-Al_2O_3 and results in a denser, slow-growing α-alumina layer that serves as a diffusion barrier to the formation of the second spinel layer. [6.16] This effect can however be negated by surface oxides formed in the thermal spray process used if samples are not surface-treated prior to oxidation.

The purpose of this study is to investigate the behaviour of nanostructured NiCoCrAlY coatings in an environment containing O_2, SO_2 and water vapour. The environment chosen is representative of an oil refinery boiler, which typically operates at temperatures around 800°C, with localized hot spots as high as 1000°C [6.2]. Samples of high-velocity oxy-fuel sprayed (HVOF), nanostructured NiCoCrAlY were selected as HVOF is a relatively easy, low-cost deposition method that is known to preserve nanostructure from feedstock to coating [6.17].

6.2 Experimental Procedures

The NiCoCrAlY coatings were produced from commercially available gas atomized -325 mesh Amdry 9951 powder from Sulzer Metco. Initial powder composition can be found in Table 6.1.

Table 6.1: Chemical composition of the NiCoCrAlY powder

Alloy Composition (Mass %)				
Ni	Co	Cr	Al	Y
46.5	23	17	13	0.5

Nanostructure was obtained through cryomilling for 16 hours in a Union Process 1-S attrition mill at 180rpm. The ball to powder ratio was 30:1. Liquid nitrogen levels were maintained through continuous addition to the vessel and 0.2% stearic acid was added to the powder to prevent the particles from coating the steel balls and the vessel. The nanostructured powder was then deposited onto a copper substrate via HVOF, resulting in a coating 470 μm thick, on average. Freestanding coatings were obtained by leaching away the copper substrate in nitric acid. Transmission electron microscopy of the same samples conducted previously shows that nanostructure was indeed preserved with an average grain size of 10.5±5.5 nm, for the as-sprayed coating [6.18].

A first cycle of oxidation testing was conducted in a controlled environment custom-built tube furnace mated to a Cahn D-100 balance for thermogravimetric analysis (TGA), shielded with helium. Samples were placed on an alumina plate suspended from the balance into the furnace, the system was closed and heated to 1000°C at 4.2°C/min in argon. Once at temperature and stable, the Ar was replaced with flowing air for 48 hours followed by another Ar purge and cooling. Prior to entering the furnace, the air was bubbled through water at varying temperatures to pick up 0, 4 or 8% water vapour.

Calculation of parabolic rate constants (k_p) was performed using the method described by Pierraggi [6.19].

A second cycle of static oxidation tests were conducted in a similar custom-built tube furnace without TGA. Samples were placed in the tube on an alumina refractory sample holder then closed and heated to 1000°C at 8°C/min in air. Once the desired temperature was reached air or a mixture containing 0.5% SO_2 described in Table 6.2 was introduced. In this case a wider range of water vapour levels was used: 0, 2, 4, 6 or 8%. TGA tests indicated that under all conditions stable oxidation following a parabolic rate law was established within 6 hours. Consequently, tests of 24-hour durations were run; in each case the system was purged with air on completion of the test and furnace-cooled.

Table 6.2: Composition of the SO_2-bearing environment

Gas Composition (Mass %)			
N_2	CO_2	O_2	SO_2
82.5	12	5	0.5

Mass of samples for the oxidation tests was measured before and after testing using a Sartorius BP 110S Scale. X-ray diffraction (XRD) patterns were obtained with a Philips PW1070 X-Ray Diffractometer with a scan angle ranging from 30 to 80 (2θ), step size of 0.005 (2θ) and dwell time of 0.5s. Phase identification was completed using X'Pert HighScore software. Scanning electron microscope (SEM) observations and energy-dispersive spectroscopy (EDS) were carried out on a Philips XL-30 FE-SEM with EDAX EDS.

A thermodynamic study of the system was also conducted using FactSage thermochemical software. In oxidation of alumina-forming alloys, the oxygen partial pressure can vary through the thermally grown oxide layers. At the metal interface, the oxygen partial pressure is low and the system is considered to be in metallic saturation. A gradient of oxygen partial pressure exists across the oxide layer, and the gas interface can be considered in relative oxygen saturation. Calculations using the FACT53, FTOxid and SGTE databases were conducted to determine the oxide layers present at equilibrium in the SO_2-bearing environment with 4% water vapour. The thermodynamic calculations do not account for the kinetic effects of diffusion and also assume the entire metallic substrate reacted to form oxide.

6.3 Results

Figure 6.1 shows the calculated oxidation behaviour of the NiCoCrAlY coating at 1000°C. Thermodynamic modeling indicates that on a substrate consisting of FCC γ-phase and BCC NiAl intermetallic β-phase the initial layer formed is an Al_2O_3 corundum phase evolving into an $(Al,Cr)_2O_3$ corundum phase at increase oxygen partial pressure. Depletion of aluminum in the substrate from corundum formation results in a second spinel-phase layer comprised primarily of $NiAl_2O_4$, $CoAl_2O_4$ and other similar oxides. FactSage also indicates the thermodynamic possibility of forming a third NiO or CoO layer, upon depletion of all other constituents, but this does not take into account the diffusion limiting effect of the previous oxide layers formed. Consequently this third layer has not been seen in many studies. It is important to note that from a thermodynamic standpoint the presence of 0.5% SO_2 do not have any substantial effect on the type of oxides that form.

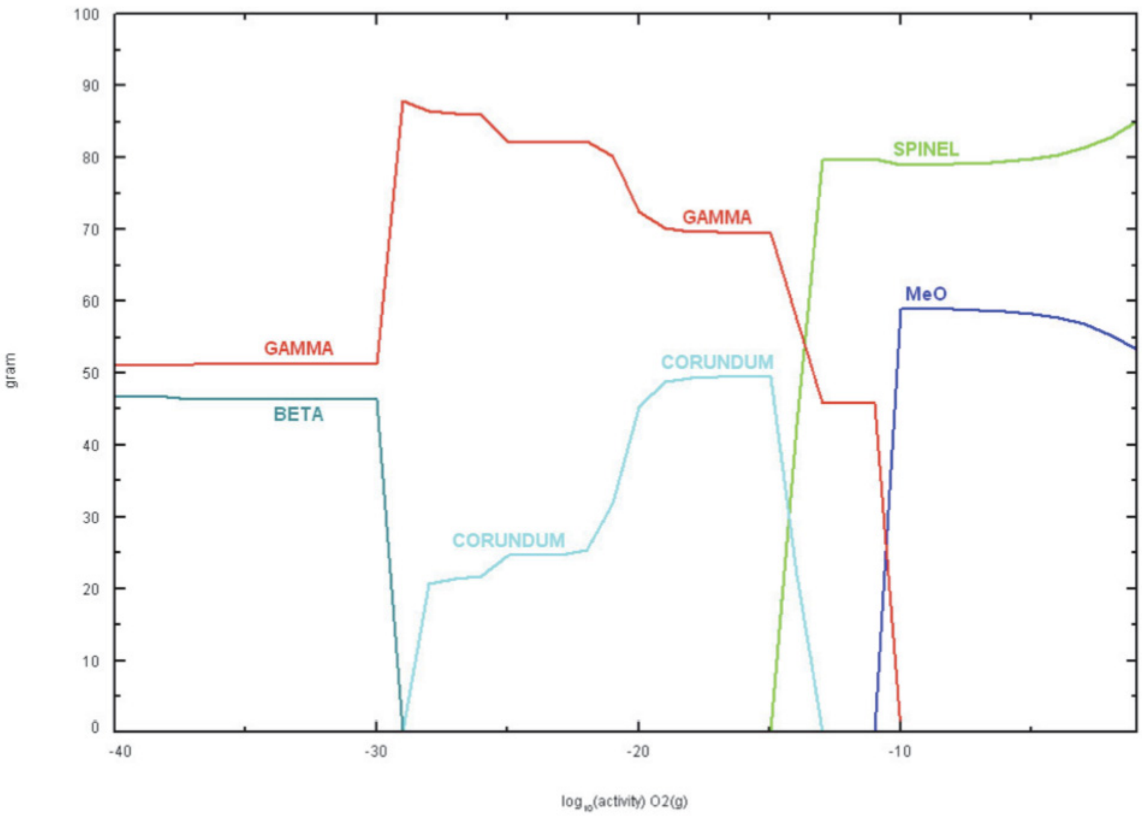

Figure 6.1: FactSage model of surface oxides formed on NiCoCrAlY.

XRD patterns for samples oxidized in Air and the 0.5% SO_2 environment at both 0 and 8% water vapour are presented in Figure 6.2. The tallest peaks correspond with the γ-phase (JCPDS #001-1258) and in all cases the surface oxides formed are alumina (JCPDS #011-0661) and $CoAl_2O_4$ (JCPDS #044-0160), which is consistent with results found by Mercier *et al.* for oxidation of MCrAlY alloys in air [6.18]. While FactSage predicted that more $NiAl_2O_4$ should form on the surface, rather than $CoAl_2O_4$, these oxides are substitutionally interchangeable in the spinel phase and relatively difficult to differentiate due to their similar diffraction patterns.

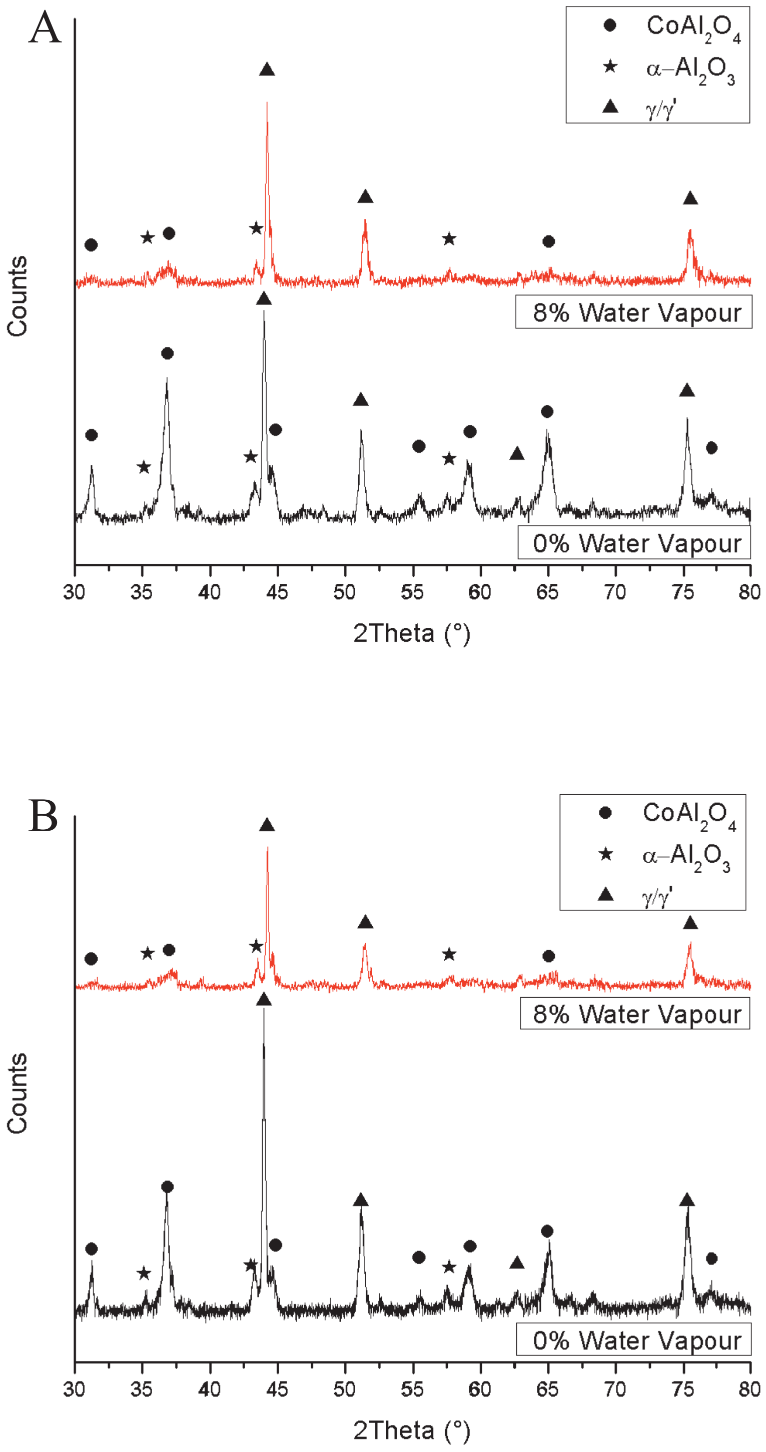

Figure 6.2: XRD patterns of nanostructured NiCoCrAlY coatings oxidized at 1000°C for 24 hours in air (A) and the SO_2 mixture (B) with 0 and 8% water vapour.

Thermogravimetric data for samples oxidized in air at 0, 4 and 8% water vapour is presented in Figure 6.3. All three cases show typical oxidation growth, characterized by an initial period of rapid mass gain followed by stable growth that observes the parabolic rate law. At 4% water vapour this initial oxidation stage, which is typically associated with the formation of metastable θ-alumina phases [6.20], is extended and results in substantially more overall mass gain, while the second stable oxidation stage follows kinetics similar to the sample oxidized without water vapour. In order to verify the existence of metastable aluminas a 30-minute interrupted oxidation test was conducted under the same conditions as the longer TGA tests. A glancing-angle XRD pattern for said samples is presented in Figure 6.4 showing peaks of θ-alumina along with the expected α-alumina and substrate phases. In contrast the sample oxidized at 8% water vapour not only has a shorter transient period, but also shows slower kinetics in the second stage and less overall mass gain. This is further highlighted in Table 6.3 describing the parabolic rate constants for both stages of oxidation. The presence of water vapour increases k_p for the initial stage by one order of magnitude and while second stage kinetics are indeed similar for 0 and 4% water vapour, 8% causes a drop in second-stage oxidation rate.

Table 6.3: Parabolic rate constants for transient and stable oxidation in air with 0, 4 and 8% water vapour.

	Parabolic Rate Constant, k_p ($g^2/cm^4/s$)		
Vapour Level	0%	4%	8%
Initial Stage	3.329×10^{-11}	3.323×10^{-10}	2.496×10^{-10}
Second Stage	2.265×10^{-11}	2.883×10^{-11}	3.534×10^{-12}

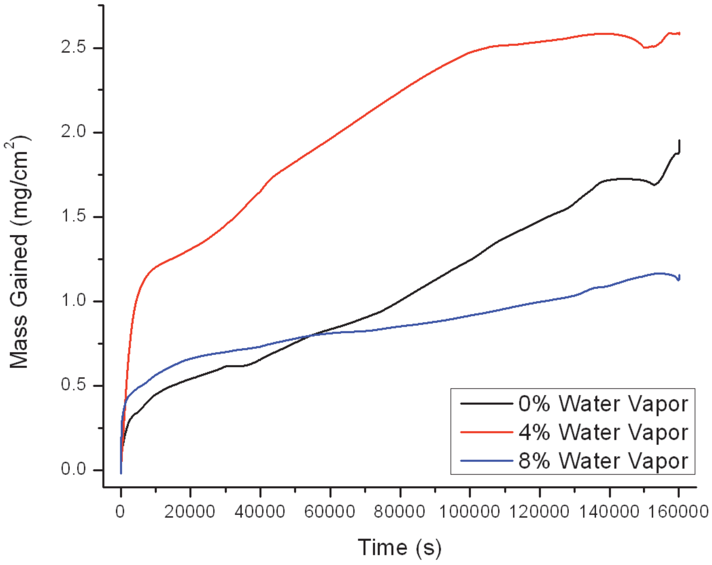

Figure 6.3: Thermogravimetric data for NiCoCrAlY coatings oxidized at 1000°C for 48 hours in air with varying water vapour content.

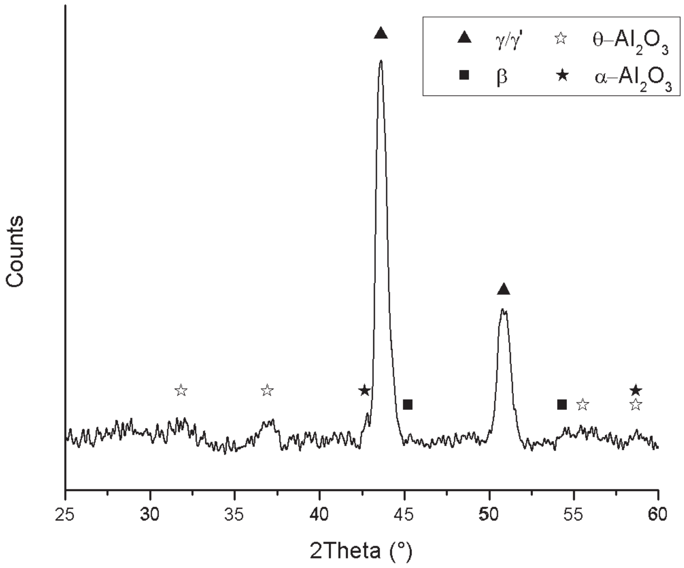

Figure 6.4: Glancing angle XRD pattern of nanostructured NiCoCrAlY coating oxidized at 1000°C for 30 minutes in air.

Mass gain for the second series of oxidation tests, in both air and the 0.5% SO_2 environment containing various levels of H_2O, is presented in Figure 6.5 and notably similar behaviour can be observed for both environments. Samples oxidized in air appear to have consistent mass gain in the range of 1.5%, but with a clear increase at specifically 4% water vapour. Coatings oxidized in the SO_2-bearing environment show a similar peak in mass gain at 4% water vapour, although this rise is spread more gradually across the range of water vapour levels.

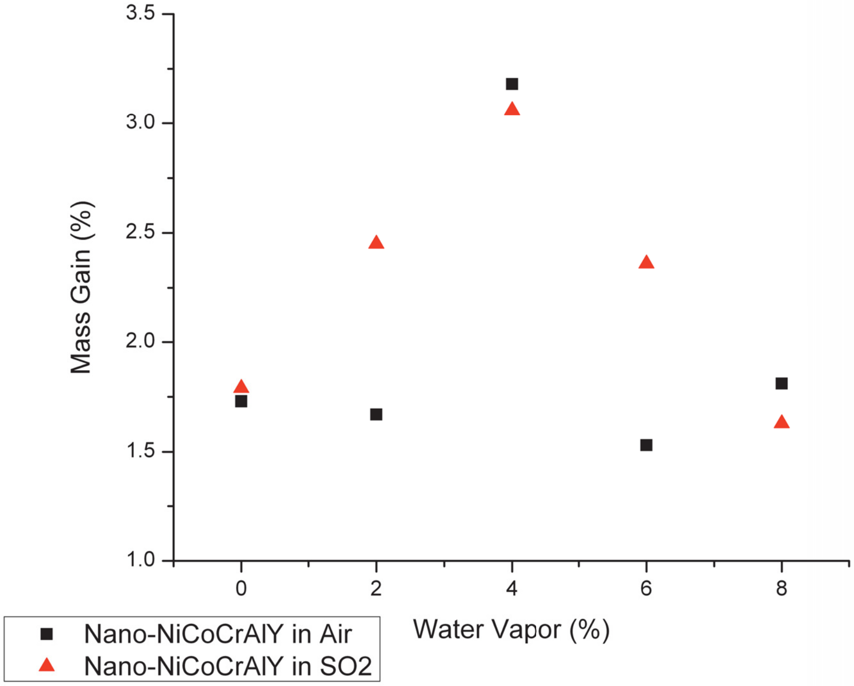

Figure 6.5: Mass Gain data for nanostructured NiCoCrAlY coatings oxidized at 1000°C for 24 hours in air and the SO_2 mixture with varying water vapour content.

Thickness measurements of the oxide scale for samples exposed to air and SO_2 are presented in Figures 6 and 7 respectively. Each data point represents an average of scale thickness across multiple SEM images and analyzed with CLEMEX image analysis software. In the both cases the inner scale, composed of alumina, appears to thin slightly with increasing water vapour up to 4%. In contrast the outer spinel scale thickens substantially. Combined, this results a drop in total scale thickness at lower vapour levels and an overall increase in scale thickness at higher water vapour levels.

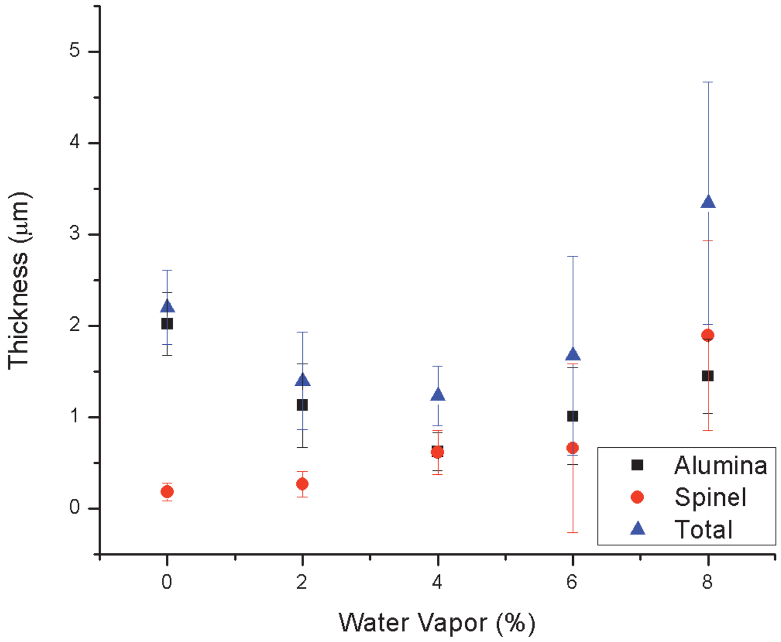

Figure 6.6: Thickness of the oxide scales formed on NiCoCrAlY oxidized in air at varying levels of water vapour.

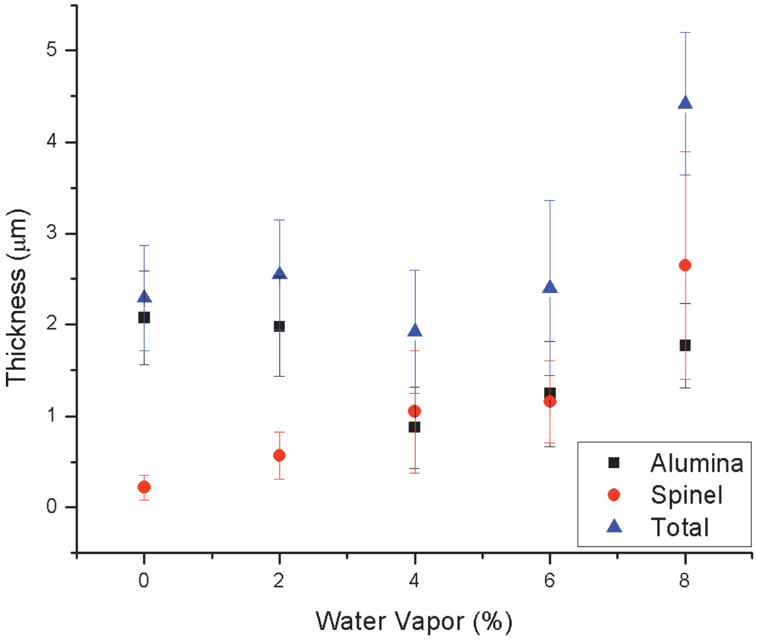

Figure 6.7: Thickness of the oxide scales formed on NiCoCrAlY oxidized in the SO_2 environment at varying levels of water vapour.

This evolution in scale thickness can also be seen in cross-sectional backscattered electron micrographs of the corresponding samples, presented in Figures 8 and 9, the former showing samples oxidized in air and the latter in the 0.5% SO_2 environment. The oxide scale shows two regions, the darker alumina phase on the coating surface and the lighter mixed-oxide phase as an outer layer. The mixed oxide layer was shown to contain Ni, Co, Al, Cr and O by EDS analysis confirming the spinel found in XRD analysis. A visible variation in scale thickness is clear across the range of vapour levels, notably in the spinel layer. Internal oxidation is also observed along prior particle boundaries and similarly to the inner surface scale is comprised solely of Al and O, as confirmed by EDS. Unlike the surface scale that appears to thicken at higher water vapour levels, the internal oxidation only appears to increase up to 4%, and is notably less in the 6 and 8%

samples. Composition of all oxides found is consistent with XRD observations and FactSage predictions.

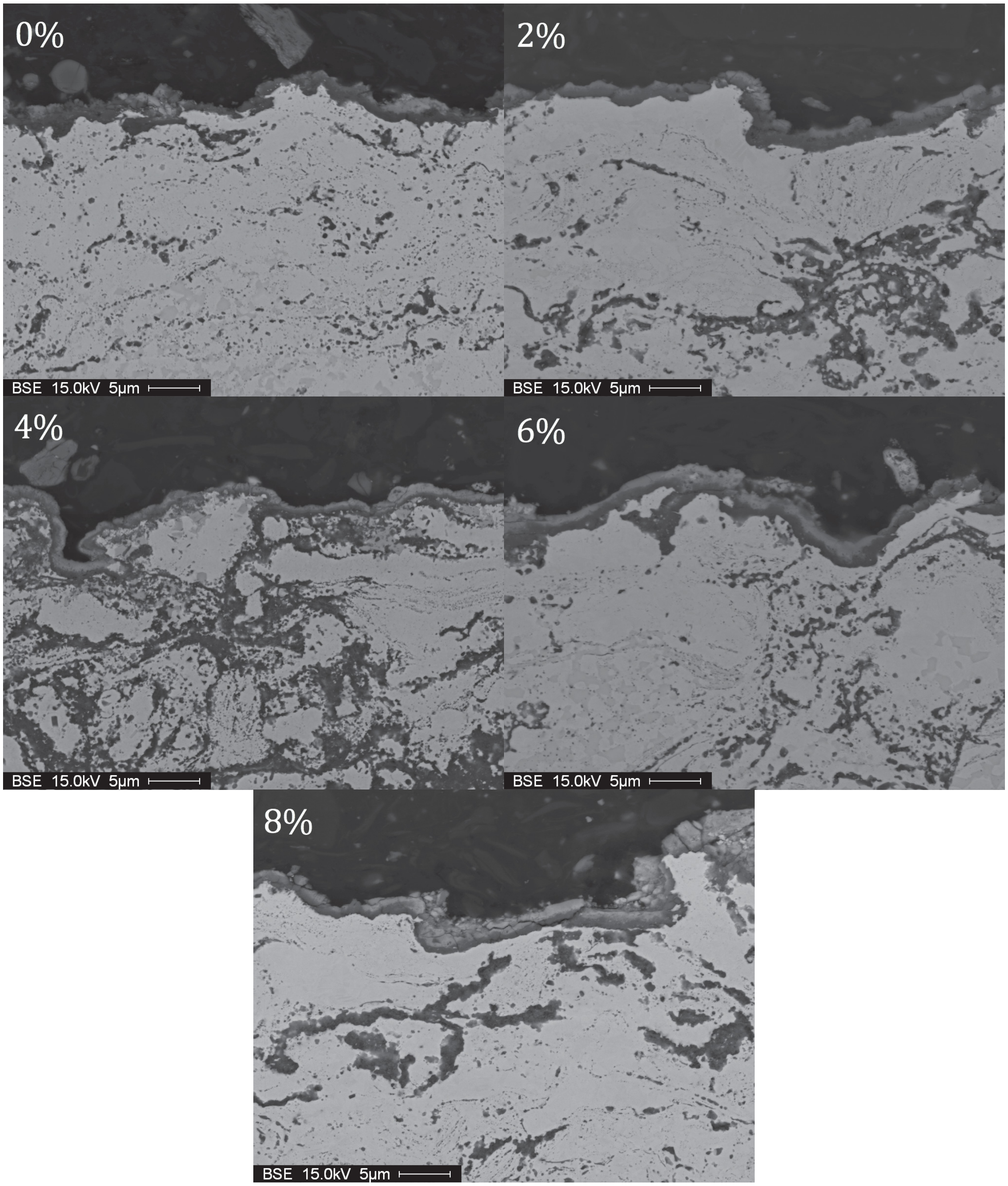

Figure 6.8: Backscattered electron micrographs of nanostructured NiCoCrAlY coatings oxidized at 1000°C for 24 hours in air with indicated water vapour levels.

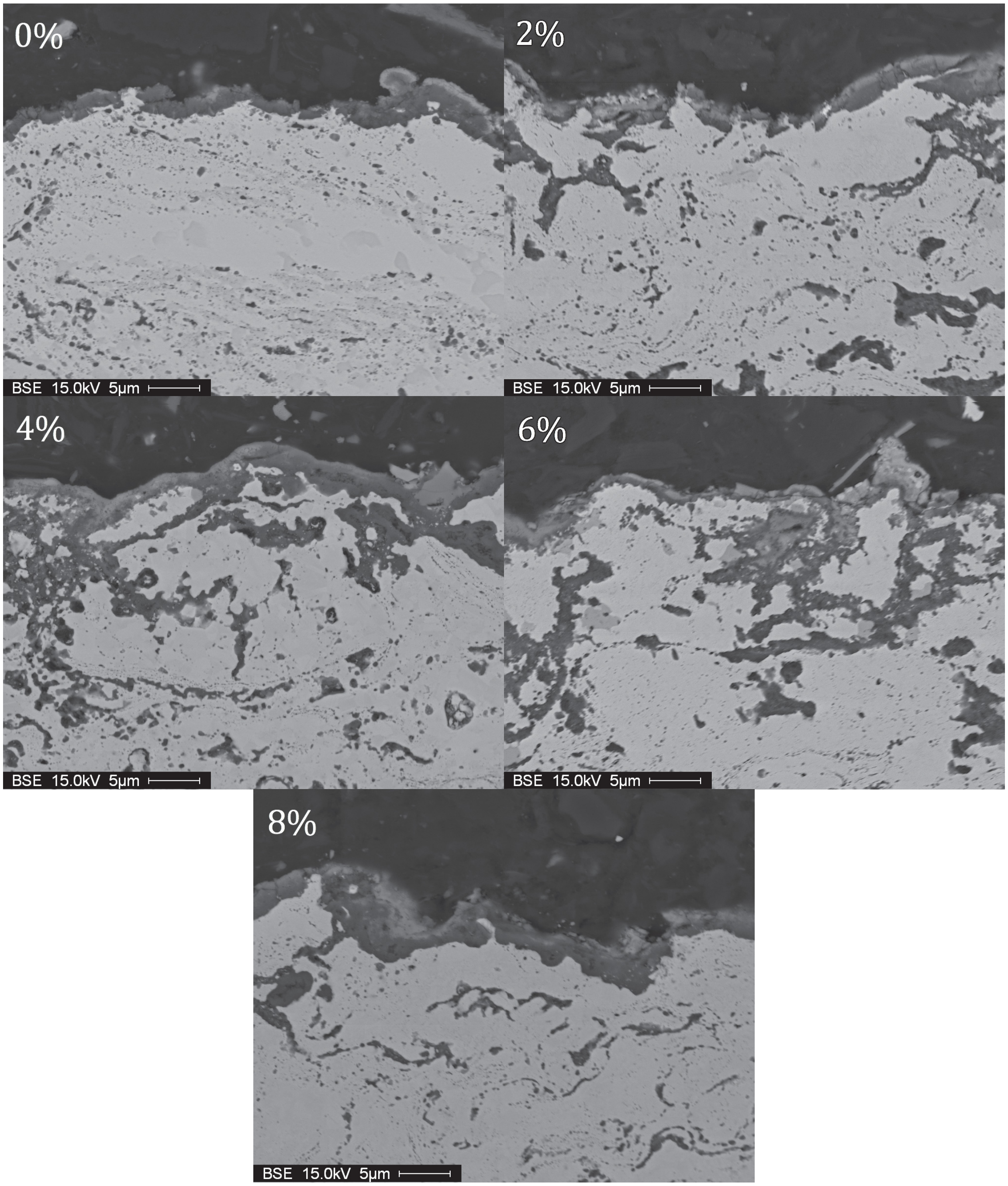

Figure 6.9: Backscattered electron micrographs of nanostructured NiCoCrAlY coatings oxidized at 1000°C for 24 hours in the SO_2 *environment with indicated water vapour levels.*

6.4 Discussion

6.4.1 Scale Effects

Birks *et al.* have shown that the presence of water vapour generally causes an increase in the oxidation rate of metals [6.21]. This is due to increased H_2O partial pressure with respect to oxygen across pores in the coating, particularly close to the coating surface. As a result increased transport of H_2O across the pores is witnessed and an overall increase in scaling rates can be seen. The studies by Leyens *et al.*, Zhou *et al.*, Saunders *et al.* and Subanovic *et al.*, all support this increase in scaling for the case of MCrAlY alloys [6.8-6.11], and as such an increase in oxide thickness can be expected. Furthermore, the study by Zhou *et al.* indicates increased formation of Ni- and Cr-based oxides as a second oxide layer with water vapour present. The work of Maris-Sida *et al.* on Ni-Cr-Al alloys goes further to explain that the dissociation of water vapour can cause an increase of vacancies in both the alumina and spinel phases formed while also reducing the interfacial toughness of the alumina/alloy interface [6.22]. This could in turn allow for an increase in internal oxidation along with increased scaling.

A similar effect appears to occur in the present work and is reflected specifically in the initial stages of oxidation. The presence of water vapour appears to increase oxidation rates during the early formation of transient θ-alumina, which later converts to the more stable α-alumina. The transient stage is also lengthened at 4% water vapour. Metastable θ-alumina is notably 13% less dense than the stable α-Al_2O_3 [6.23] allowing for substantially more diffusion through the scale for a longer period of time. This rise in vacancies allows for transport of Ni across the scale interface as well as O_2, leading to increased spinel formation through upward diffusion of Ni. The growth of alumina is not substantially affected however, as the inward transport of O_2 is already present in n-type semiconductors; this is reflected in the similar k_p found for the stable oxidation stage at both 0 and 4% vapour. This effect is evidenced additionally in Figures 6 and 7, showing only a very slightly drop in alumina thickness with increasing water vapour up to 4%, contrasted with substantial increases in spinel thickness.

6.4.2 Internal Oxidation

Concurrent to the variation in scale thickness, the micrographs presented in Figures 8 and 9 show a likely trend of internal oxidation of the coating itself. This trend appears to increase with water vapour up to 4%, and subsequently decrease at 6 and 8% water vapour. This internal oxidation may be caused by the extension of the transient oxidation stage allowing for more penetration of oxygen into the coating itself. Interestingly when comparing oxidation at 0 and 4% vapour, all of the extra mass gain seen in the 4% sample occurs in the initial transient stage. This effect would indicate that the internal oxidation is primarily occurring while θ-alumina is allowing oxygen penetration, and that internal oxidation is likely limited by conversion from θ to α. Furthermore, Evans *et al.* have postulated that in plasma-sprayed MCrAlY coatings, oxidation effects in spraying can result in diffusional isolation of certain areas within the coating with respect to the bulk [6.24]. These areas form “diffusion cells” typically limited along grain boundaries or prior particle boundaries and will experience increased aluminum depletion as the surrounding boundary forms alumina. The inward diffusion of oxygen will thus exacerbate internal oxidation of the coating [6.24]. At higher levels of water vapour (6 or 8%), despite the increase in k_p for the transient stage, total mass gain is in fact reduced. This reduction of mass gain could be attributed the thickening effect discussed in the previous section; in this case the more porous θ-alumina forms a thicker oxide layer in addition to the thickened spinel layer. This scale may block diffusion of O simply by virtue of the longer diffusion path through the scale. It is possible that this lengthened diffusion path prevents some internal oxidation. Additionally this thicker scale, once converted to α-alumina, serves as even more of a diffusion barrier resulting in a reduced k_p in the second stage of oxidation, even compared to samples oxidized in dry air.

Maris-Sida *et al.*, in addition to increased spinel formation, also saw extensive formation of internal Al_2O_3 in Ni-Cr-Al alloys and have attributed this effect to an extension of the transient oxidation stages, among other effects [6.22] and the review by Saunders *et al.* attributes increase internal oxidation to the fast diffusion of water through oxides by increased cation vacancies or by increased molecular diffusion through pores in the oxide layer and into the coating [6.10]. As well, oxygen concentration on the surface of the oxide may be increased due to catalytic dissociation of water on alumina [6.25]. This in turn can create a larger oxygen gradient across the scale, allowing again for the possibility of increased oxide penetration.

6.4.3 Combined Effect

Given these observations, the effect of water vapour appears to manifest itself in several competing phenomena. First an extension of the transient oxide stage results in the formation of more θ-alumina for longer periods of time and allows for more diffusion through the scale during this transient stage. Second, due to this extended transient stage, a thickening of the oxide layer at high water vapour levels with an increase in spinel phase is seen. This causes a lengthening of the diffusion path through the oxide, subsequently limiting the transport of oxygen through the scale. Finally the presence of water vapour may also cause a rise in internal oxidation due to increased transport across the scale. It would appear that 4% water vapour is the threshold at which lengthening of the diffusion path has not yet begun to block movement through the scale layer, but internal oxidation may have increased to a detrimental level causing substantial mass gain.

6.4.4 Impact of SO_2

Thermodynamic predictions with FactSage indicate that oxidation of NiCoCrAlY in a SO_2-bearing environment should not differ from oxidation in air, giving an indication that behaviour with water vapour present should also be similar in these two systems. Again similar competing effects of oxide penetration versus decreased transport across the scale appear to occur. It has as well been proposed by Smialek *et al.* that the presence of sulphur at the Al_2O_3/alloy interface can cause bond stretching and weakening [6.26]. The authors went on to attribute this interface effect, in combination with moisture, to the spallation and failure of the alumina scale, but the possibility of increased transport through H_2O-sulfur interaction must be acknowledged. While in this case sulphur has not been detected in the oxide scale and the maximum mass gain at 4% water vapour is not affected by SO_2, total scale thickness is increased slightly and the change in mass appears more gradual across the range of water vapours. The proposed interfacial effect may be indeed be responsible for these slight variations experienced, though not enough to cause substantial overall changes in mass gain.

6.5 Conclusions

In summary it has been found that the oxides formed on nanostructured NiCoCrAlY coatings deposited by HVOF are alumina followed primarily by cobalt aluminum oxide and the presence of 0.5% SO_2 does not appear to alter these in any way. The effect of water vapour on mass gain has been characterized for both systems. In both cases the presence of water vapour causes an increase in oxidation rate and an extension of the initial transient stage of oxidation. Consequently increased diffusion though the scale is possible over a longer period of time. This effect combined with the general increase in reaction rates due to the presence of water vapour results in a thickening of the spinel layer and a slight thinning of the alumina layer as a function of vapour level. This results in an overall increase in scale thickness at higher vapour levels.

At the same time, the extended transient stage allows substantial internal oxidation of the coating to occur until the point that the scale thickening can again block diffusion. 4% water vapour seems to be “crossover” point for these effects, above which internal oxidation is limited and mass gain is again notably reduced. Interestingly the thickened oxide layer, once past transient oxidation and converted to dense α-alumina serves to limit mass gain further in the second stage of oxidation. This is evidenced in the reduction of k_p at 8% vapour.

Acknowledgments

The authors would like to thank Imperial Oil for funding this research as well as Dominic Mercier for analysis of the as-sprayed coating and Dr. In-Ho Jung for his help with thermodynamic calculations.

6.6 References

[6.1] J. Gutzeit, R.D. Merrick, L.R. Schaferstein, *Corrosion in petroleum refining and petrochemical operations* in: ASM Handbook, Vol 13: Corrosion, ASM Handbook Comittee, Pittsburgh, 1998.

[6.2] R. Terms, A. M. Al Zahrani, *Cost of corrosion in oil production and* refining, Saudi Aramco Journal of Technology, Summer (2006) 2-14.

[6.3] C. G. Levi, E. Sommer, S. G. Terry, A. Catanoiu, M. Rühle, *Alumina grown during deposition of thermal barrier coatings on NiCrAlY*, Journal of the American Ceramic Society 86 (2003) 676-685.

[6.4] Q. M. Wang, Y. N. Wu, P. L. Ke, H. T. Cao, J. Gong, C. Sun, L. S. Wen, *Hot corrosion behaviour of AIP NiCoCrAlY(SiB) coatings on nickel base superalloys*, Surface and Coatings Technology 186 (2004) 389-397.

[6.5] J. Bursík, P. Broz, J. Popovic, *Microstructure and phase equilibria in Ni‑Al‑Cr‑Co alloys*, Intermetallics 14 (2006) 1257-1261.

[6.6] B. Baufeld, M. Bartsch, P. Broz, M. Schmucker, *Microstructural changes as postmortem temperature indicator in Ni–Co–Cr–Al–Y oxidation protection coatings*, Materials Science and Engineering A 384 (2004) 162-171.

[6.7] K. J. Hemker, B. G. Mendis, C. Eberl, *Characterizing the microstructure and mechanical behavior of a two-phase NiCoCrAlY bond coat for thermal barrier systems*, Materials Science and Engineering A 483-484 (2008) 727-730.

[6.8] C. Leyens, K. Fritscher, R. Gehrling, M. Peters, W. A. Kaysser, *Oxide scale formation on an MCrAlY coating in various H2-H2O atmospheres*, Surface and Coatings Technology 82 (1996) 133-144.

[6.9] C. Zhou, J. Yu, S. Gong, H. Xu, *Influence of water vapour on the isothermal oxidation behaviour of low pressure plasma sprayed NiCrAlY coating at high temperature*, Surface and Coatings Technology 161 (2002) 86-91.

[6.10] S. R. J. Saunders, M. Monteiro, F. Rizzo, *The oxidation behaviour of metals and alloys at high temperatures in atmospheres containing water vapour: A review*, Progress in Materials Science 53 (2008) 775-837.

[6.11] M. Subanovic, D. Naumenko, M. Kamruddin, G. Meier, L. Singheiser, W. J. Quadakkers, *Blistering of MCrAlY-coatings in H2/H2O-atmospheres*, Corrosion Science 51 (2009) 446-450.

[6.12] E. Godlewska, E. Roszczynialska, Z. Zurek, *The influence of sulfur pressure on Sulfidation behaviour of NiCoCrAl(Y) alloys at high temperature,* Werkstoffe Und Korrosion 45 (1994) 341-348.

[6.13] L. Ajdelsztajn, J. A. Picas, G. E. Kim, F. L. Bastian, J. Schoenung, V. Provenzano, *Oxidation behavior of HVOF sprayed nanocrystalline NiCrAlY powder*, Materials Science and Engineering A 338 (2002) 33-43.

[6.14] F. Wang, *The Effect of Nanocrystallization on the Selective Oxidation and Adhesion of Al_2O_3 Scales*, Oxidation of Metals 48 (1997) 215-224.

[6.15] F. Tang, L. Ajdelsztajn, J.M. Schoenung, *Influence of Cryomilling on the Morphology and Composition of the Oxide Scales Formed on HVOF CoNiCrAlY Coatings*, Oxidation of Metals 61 (2004) 219-238.

[6.16] D. Mercier, C. Kaplin, G. Goodall, G. Kim, M. Brochu, *Parameters influencing the oxidation behaviour of cryomilled CoNiCrAlY*, Surface and Coatings Technology 205 (2010) 2546-2553.

[6.17] L. Zhao, M. Parco, E. Lugscheider, *High velocity oxy-fuel thermal spraying of a NiCoCrAlY alloy*, Surface and Coatings Technology 179 (2004) 272-278.

[6.18] D. Mercier, B. D. Gauntt, M. Brochu, *Thermal stability and oxidation behaviour of nanostructured NiCoCrAlY coatings*, Surface and Coatings Technology 205 (2011) 4162-4168.

[6.19] B. Pierragi, *Calculations of parabolic reaction rate constants*, Oxidation of Metals 27 (1987) 177-185.

[6.20] M. W. Brumm, H. J. Grabke, *The oxidation behaviour of NiAl - I. Phase transformations in the alumina scale during oxidation of NiAl and NiAl-Cr alloys*, Corrosion Science 33 (1992) 1677-1690.

[6.21] N. Birks, G. H. Meier, F. S. Pettit, *Introduction to the high temperature of metals*, 2nd edition, Cambridge University Press, Cambridge, 2006.

[6.22] M.C. Maris-Sida, G.H. Meier, F.S. Pettit, *Some Water Vapor Effects during the Oxidation of Alloys that are α-Al_2O_3 Formers*, Metallurgical and Materials Transactions: A 34A (2003) 2609-2619.

[6.23] K. Wefers, C. Misra, *Oxides and Hydroxides of Aluminum*, Alcoa Technical paper, 1987.

[6.24] H.E. Evans, M.P. Taylor, *Diffusion Cells and Chemical Failure of MCrAlY Bond Coats in Thermal-Barrier Coating Systems*, Oxidation of Metals 55 (2001) 17-34

[6.25] S.N. Rashkeev, K.W. Sohlbeg, S. Zhuo, S.T. Pantelides, *Hydrogen-induced initiation of corrosion in aluminum*, Journal of Physical Chemistry 111 (2007) 7175-7178.

[6.26] J.L. Smialek, G.N. Morscher, *Delayed alumina scale spallation on Rene'N5+Y: moisture effects and acoustic emission*, Materials Science and Engineering A 332 (2002) 11-24.

Chapter 7: The effect of grain size on the cyclic oxidation of NiCoCrAlY[3]

C. Kaplin, J. Fassoni and M. Brochu
McGill University
Department of Materials Engineering
3610 University Street, Montreal, QC, H3A 0C5

---

[3] Published: C. Kaplin, J. Fassoni, M. Brochu, *The effect of grain size on the cyclic oxidation of NiCoCrAlY*, Journal Of Metals, available online 5 April 2014.

Preface

While variations in oxidative environment are common in many industrial settings, other factors can have a substantial effect on oxidation performance. Chapters 4 through 6 focused on various aspects of the oxidation of MCrAlY alloys while maintaining isothermal oxidation conditions. Non-isothermal conditions, however, commonly occur in industry, particularly in air- and land-based gas turbines. The following chapter discusses the thermal cycling performance of the bulk NiCoCrAlY samples, with an emphasis on the improved thermal cycling performance of nanostructured samples through reduced spallation and subsequent internal oxidation.

Abstract

NiCoCrAlY samples were fabricated via spark plasma sintering (SPS) with and without prior cryomilling of the as-received powder. Thermal cycling oxidation tests were conducted at 1000°C in air up to 200 1-hour cycles. Mass gain data indicates a notably lower mass gain for the cryomilled NiCoCrAlY sample. In both the conventional and cryomilled samples, scanning electron microscopy and x-ray diffraction data indicate a single layer oxide scale of α-alumina has formed, having undergone a transition from θ-alumina during oxidation testing. Spallation in the conventional sample allowed a significant amount of internal spinel oxide formation, while this was not found in the cryomilled sample. The difference in behaviour is attributed to increased pathways for aluminum diffusion to the surface and nucleation sites for the α-alumina transition, as well as improved scale adhesion through nanostructuring and stress relief through the accelerated θ-α transition.

7.1 Introduction

Aero- and land-based gas turbines are among the most complex and demanding systems in industry. Varied and cyclic thermal and mechanical loads, oxidative and corrosive gasses, and erosion and degradation processes all lead to significant challenges in terms of material selection and design [7.1]. One of the most common methods to protect turbine components in high temperature environments or thermal cyclic environments is the thermal barrier coating system (TBC). A typical TBC consists of an yttria-partially-stabilized zirconia (YPSZ) top coat and nickel superalloy bond coat, normally of the MCrAlY class of alloys where M = Ni, Co or a combination of both. MCrAlY alloys provide the dual benefit of oxidation protection through the formation of a thermally grown oxide (TGO) [7.1] and provide good thermal matchup between other coating layers [7.2]. The thermally grown oxide scales can also result in notable high temperature corrosion resistance [7.1, 7.3].

MCrAlY alloys normally consist of a two-phase structure containing the γ-phase, a solid solution of Ni, Co and Cr and the β-phase, an intermetallic of Ni and Al. The γ' phase, strengthening precipitates of Ni_3Al, is also present at some compositions. The β-NiAl phase is essential in that it provides a source of aluminum for the growth of an alumina TGO under oxidizing conditions [7.4]; this phase can be stabilized by the presence of Co in the alloy, while Cr lowers the required concentration of Al to form a continuous scale [7.1]. The failure of TBC systems is normally attributed to fast-growing spinel oxides that can develop on MCrAlY alloys at long oxidation times; the stresses induced at the interface between the bond coat and top coat by these oxides cause cracking and spallation of the oxide scale [7.5]. Consequently, several recent publications have focused on improving the oxidation performance of TBC's and MCrAlY alloys [7.6, 7.7]. Of particular interest, some studies have also focused on grain size reduction as a method to improve oxidation resistance in MCrAlY alloys [7.8-7.10]. In particular, the work of Ajdelsztajn *et al.*, Liu *et al.*, and Tang *et al.* have all shown nanostructured MCrAlY coatings exhibit improved oxidation behaviour [7.8, 7.11, 7.12]. In all three cases improved oxidation rates were attributed to increased grain boundary diffusion in the nanostructured coating. Additionally Liu *et al.* found that nanostructured NiCr coatings required a reduced minimum Al content to form alumina scales. More recently, Todde *et al.* demonstrated that the formation of a single-layer α-alumina oxide scale is promoted by cryomilling in a study of CoNiCrAlY samples consolidated by spark plasma sintering [7.13]. Mercier *et al.* have shown, based on several of the studies mentioned, that cryomilling has the dual benefit of improving aluminum distribution throughout an MCrAlY sample while also shortening the necessary distance for lattice diffusion and increasing the number of pathways for grain boundary diffusion to the surface [7.9].

Nijdam *et al.* conducted oxidation experiments of a NiCoCrAlY coating for up to 750 1-hour cycles at 1100°C [7.14]. The sample showed a mass gain of approximately 0.95 mg/cm^2 after 200 cycles. Pint *et al.* studied NiCoCrAlYHfSi coatings on various superalloy substrates using 1-hour thermal cycles at 1050°C and found oxidation rates ranging from 1.1 to 1.25 mg/cm^2 after 200 cycles [7.15]. Liang *et al.* have reported a mass gain of 0.55 mg/cm^2 for CoCrAlY samples thermally cycled using a similar procedure but at 1050°C [7.16]. Lan *et al.* studied the effect of Dy addition on the thermal cycling behaviour of CoNiCrAlY and found mass gains of approximately 0.28 and 0.59 mg/cm^2 for samples with and without Dy additions, respectively, after 100 1-

hour cycles at 1100°C [7.17].

As several of these studies focus on the growth of the alumina scale, it would be of interest to discuss the phases of thermally grown alumina. Several metastable structures have been identified as transitional forms of alumina that occur during thermal oxide growth: γ-Al_2O_3, δ-Al_2O_3, and θ-Al_2O_3 can form depending on oxidation temperature and time, before the eventual transformation to the stable corundum α-Al_2O_3 phase [7.18]. The transformation from cubic γ to monoclinic β to rhombohedral α each result in an increase in density of over 10% [7.18], which can have a significant impact on oxygen diffusion and subsequent oxidation kinetics. An earlier transition to α-Al_2O_3 is therefore desirable, as slow cation diffusion through its denser lattice results in a slow growing oxide in the long term [7.19, 7.20].

The aim of this study is to examine the thermal cycling behaviour of conventional and cryomilled NiCoCrAlY samples consolidated via Spark Plasma Sintering (SPS) in order to better understand the effect of grain size on the oxidation of this system. Cryomilling was selected as a reliable method for grain size reduction of the NiCoCrAlY powder while SPS, known for consolidation of bulk nanostructured and ultrafine samples, was chosen and a rapid method of consolidation.

7.2 Experimental Procedures

The NiCoCrAlY samples were fabricated with commercially available gas atomized Ni-130/Ni-191 powder obtained from Praxair Surface Technologies; the chemical composition of this powder is presented in Table 7.1. A portion of the powder was cryomilled for 16 hours in a Union Process 1-D attrition mill at 180 rpm with stainless steel grinding media, a ball to powder ratio of 32:1 and 0.2 wt% stearic acid added as a surfactant to prevent coating the vessel and milling media. Liquid nitrogen was continuously added throughout the cryomilling step.

Table 7.1: Chemical composition of the NiCoCrAlY powder.

Alloy Composition (Mass %)				
Ni	Co	Cr	Al	Y
46.55	23	17	13	0.45

Consolidation of the conventional and cryomilled powder was accomplished via spark plasma sintering in a Thermal Technologies 10-3 sintering press. In both cases sintering was conducted under vacuum. Conventional samples were heated at 200°C/minute to 1100°C, held for 7 minutes and cooled to ambient temperature. Cryomilled samples were heated at 250°C/minute to 1100°C, held for 10 seconds and cooled to ambient temperature. Density measurements were made using the Archimedes principle while grain size was measured via scanning electron microscopy (SEM) using the line intercept method averaging at least 100 grains as well as via X-Ray Diffraction (XRD) using the Scherrer Equation [7.21].

Cyclic oxidation testing was conducted in a custom-built tube furnace, where the hot section of the furnace was rail-mounted and could be moved onto or off of a quartz tube. The pressed samples were discs of approximately 20 mm diameter and 5 mm height; three full discs were kept for the 200-cycle tests, while half-discs were used for the shorter tests. The samples were polished to 1200 grit on all surfaces and placed in the quartz tube on an alumina sample holder. A continuous airflow of 2 lpm was introduced. The furnace was heated to 1000°C and moved over the quartz tube. A thermocouple on the sample holder reached 1000°C within 5 minutes. After 60 minutes the furnace was moved away and the airflow increased for a 15-minute forced-air quench. The airflow was then reduced to 2 lpm and the cycle restarted. After every 8 cycles the samples were removed from the furnace and weighed. Samples were removed after 24, 48, 96 and 144 cycles to characterize morphology, and 3 samples were kept for 200 cycles to monitor mass change.

XRD scans were obtained using a Bruker D8 Discover XRD using a Cu source and Vantec-5000 2D detector. Phase identification was completed using X'Pert HighScore software. SEM observations were carried out on a Philips XL-30 FE-SEM with EDAX EDS operated at 10 kV.

7.3 Results

7.3.1 Cryomilling and Consolidation

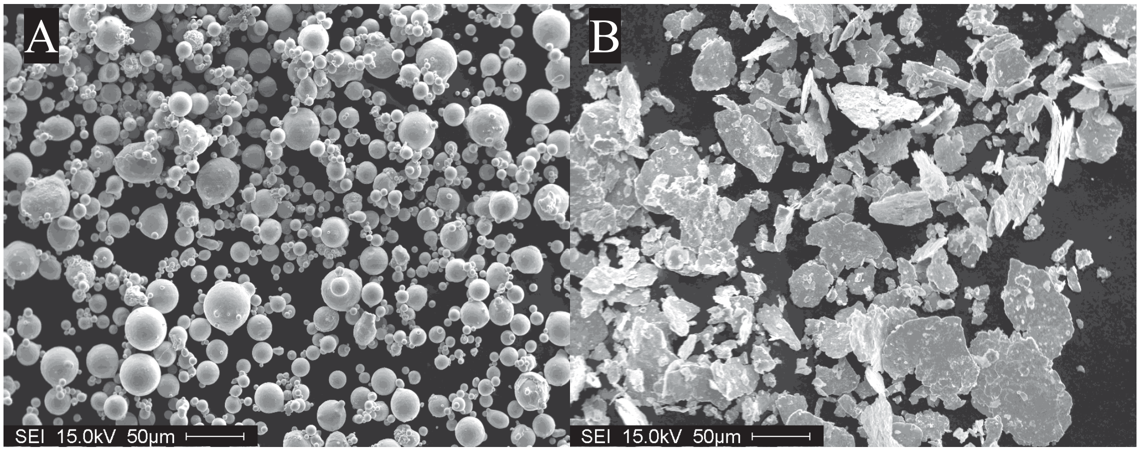

Figure 7.1: SEM images of as-received NiCoCrAlY powder (A) and cryomilled powder (B).

Milling parameters previously proven to generate significant grain refinement in NiCoCrAlY samples [7.22] were used in the present study. Micrographs of the as-received and post-cryomilled powder are presented in Figure 7.1. The flat, flaky morphology seen in Figure 7.1B is typical of cryomilled powders and indicated a reduction in grain size. This is also reflected in the XRD scans of both powders, presented in Figure 7.2. While the as-received, conventional powder has the classic sharp diffraction pattern of a γ-β NiCoCrAlY microstructure (JCPDS #'s 03-065-2865 and 03-065-4197 respectively), the cryomilled powder has only a single broad peak indicating significant grain size reduction as well as dissolution of the β-NiAl phase into the γ phase.

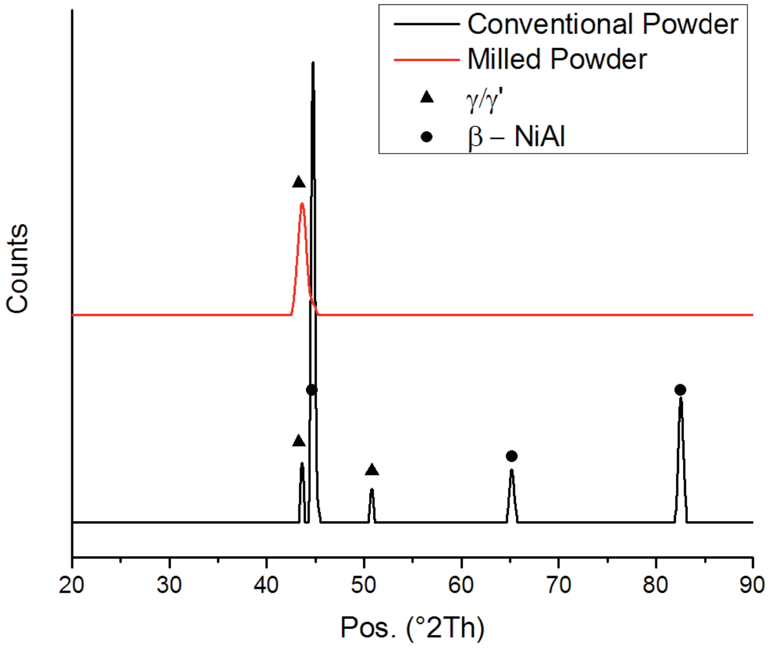

Figure 7.2: XRD patterns for conventional and cryomilled NiCoCrAlY powder.

Figure 7.3 contains cross-sectional SEM micrographs of consolidated conventional and cryomilled samples, showing clear differences in grain size post-consolidation. While the conventional sample has an average grain size of 1.2 μm, the milled consolidated sample has a grain size of approximately 150 nm measured via SEM and 109 nm according to XRD analysis using the Scherrer Equation [7.21]. Based on a calculated theoretical density of 7.2 g/cm^3, conventional samples were measured to be over 99% of theoretical density and milled samples were over 96% of theoretical density.

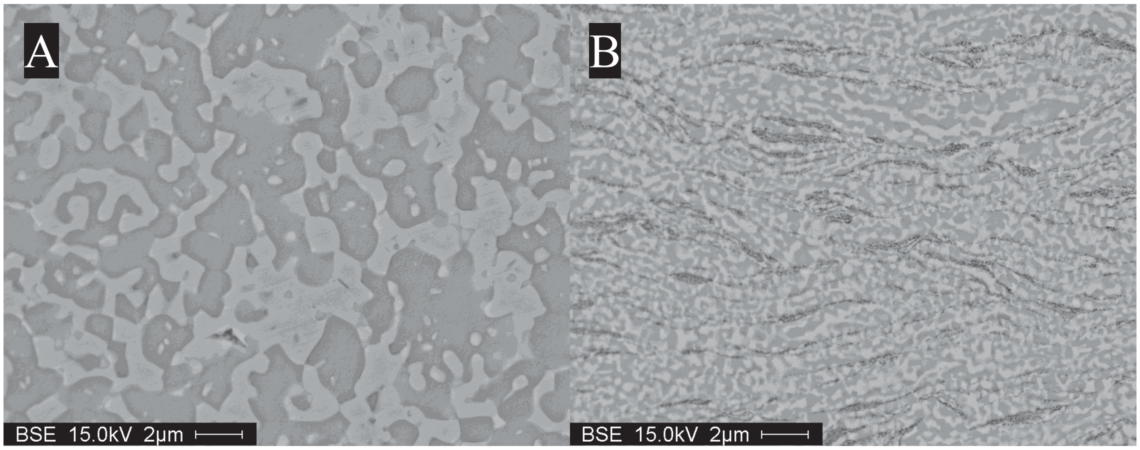

Figure 7.3: Cross-sectional SEM images of consolidated conventional (A) and ultrafine (B) NiCoCrAlY samples.

7.3.2 Thermal Cyclic Oxidation

The consolidated conventional and cryomilled NiCoCrAlY samples were subjected to oxidation testing via thermal cycling and subsequent characterization. Average mass gain data from the thermal cycling tests is presented in Figure 7.4. It is clear that cryomilled samples showed lower overall mass gain than their conventional counterparts throughout the test. Total mass gain after 200 cycles averaged 0.29 mg/cm^2 in the conventional samples and 0.22 mg/cm^2 in the cryomilled samples. The mass gain data from several studies discussed earlier [7.14-7.17] along with the data from the present study is presented in Table 7.2. It is important to note that the cryomilled NiCoCrAlY sample, having an average mass gain of only 0.22 mg/cm^2 after 200 1-hour cycles at 1000°C, is among the lowest reported for similar alloys in this temperature range.

Table 7.2: Mass gain data for various thermal cycling studies of MCrAlY alloys.

Ref	Material & Processing	Heating	Temp (°C)	Hold (min)	Cooling	# of cycles	Mass gain (mg^2/cm^4)
	NiCoCrAlY - SPS + ground	200°C/ min	1000	60	10 min forced	200	0.29
	NiCoCrAlY- Cryomilled + SPS + ground	200°C/ min	1000	60	10 min forced	200	0.22
[7.14]	NiCoCrAlY - EBPVD coating + ground	15 min	1100	45	N/A	200	0.95
[7.15]	NiCoCrAlYHfSi - HVOF on X4 + Vac Annealed	N/A	1050	60	10 min	200	1.25
	NiCoCrAlYHfSi - HVOF on X4-1 + Vac Annealed	N/A	1050	60	10 min	200	1.7
	NiCoCrAlYHfSi - HVOF on X4-2 + Vac Annealed	N/A	1050	60	10 min	200	1.1
[7.16]	CoCrAlY - EBPVD on DZ125 +	N/A	1050	50	10 min	160	0.55
	Vac Annealed + Shot Peened	N/A	1050	50	forced	300	0.85
[7.17]	CoNiCrAlY - Arc Melting +	N/A	800	60	10 min	100	0.13
	Vac Anneal + Ground	N/A	1100	60	ambient	100	0.59
	CoNiCrAlY + Dy - Arc Melting	N/A	800	60	10 min	100	0.06
	+ Vac Anneal + Ground	N/A	1100	60	ambient	100	0.28

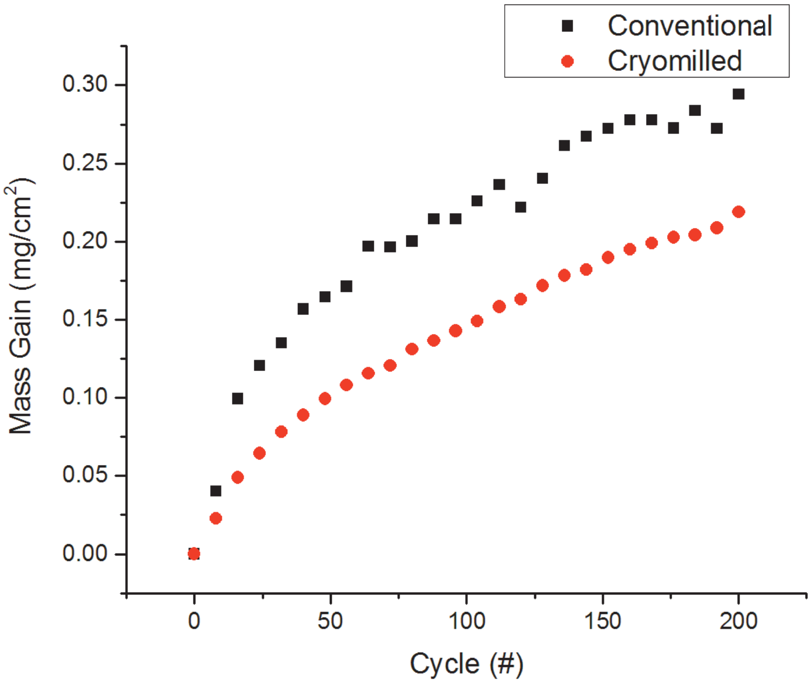

Figure 7.4: Average mass gain data for conventional and cryomilled samples oxidized for 200 cycles at 1000°C.

7.3.3 Characterization

XRD patterns for conventional and cryomilled samples oxidized for 24, 96 and 200 cycles at 1000°C are presented in Figure 7.5. At all times the primary γ/γ’ phase is clearly visible while the β-NiAl phase, known to deplete during oxidation, is detectable only by its primary peak. Examining first the cryomilled samples, peaks corresponding to α-alumina (JCPDS # 00-010-0173) become increasingly apparent with increasing number of cycles. A single, sharp peak corresponding to θ-alumina (JCPDS # 00-047-1771) is also visible, and decreases in intensity with cycle time, as expected. Examining next the conventional samples, the same primary γ/γ’ peaks and α-alumina peaks are also present. However, in this case several θ-alumina peaks are visible throughout testing, while some Spinel phase peaks (JCPDS # 00-010-0339) are ale present after 200 cycles.

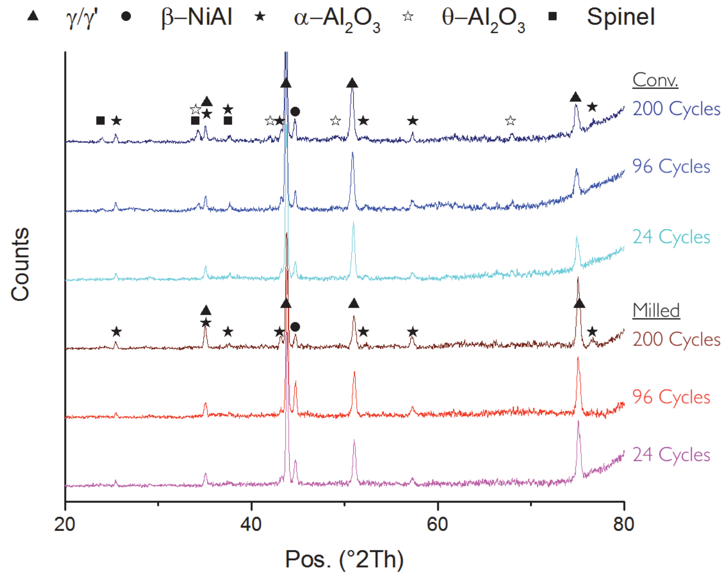

Figure 7.5: XRD data for conventional and cryomilled samples after 24, 96 and 200 1-hour oxidation cycles at 1000°C.

Cross sectional micrographs of samples oxidized for 24, 48, 96, 144 and 200 cycles were taken and are presented in Figure 7.6. Figures 6-A through E are conventional samples while 6-F through J are cryomilled. Here distinct differences in the oxide scales can be seen, particularly at longer cycle times. After 24 cycles both the conventional and cryomilled samples have developed a single-layer scale that covers most of the sample surface. The scale thickness is similar as is the depth of the β-depleted zone. After 48 cycles the scales have thickened slightly on both samples, more so on the conventional, but otherwise behaviour is similar. EDS analysis of both samples indicates that this single oxide layer is alumina. Significant differences in oxidation behaviour become more apparent after 96 cycles, presented in Figures 6-C and -H. The oxide layer on the cryomilled sample appears slightly thicker still, while also becoming consistent, showing fewer cracks and thickness variations than shorter cycle times. In contrast the conventional sample appears to have experienced some spallation, with clear thinning of the alumina scale, visible cracks, and some exposed surface areas. Additionally a small amount of internal oxidation can be seen, penetrating down from the oxidized surface. This trend continues through 144 and 200 cycles with the cryomilled sample maintaining a consistent and relatively even alumina layer while the conventional sample appears to experience degradation of the oxide layer and increasing internal oxidation.

The final conventional sample after 200 cycles, in Figure 7.6E, has a distinctly discontinuous alumina scale of varying thickness, and areas where the scale does not fully cover the substrate can be seen. EDS analysis indicates, however, that the scale is composed entirely of alumina. A significant amount of internal oxidation is visible, extending approximately 5 to 8 microns into the substrate. EDS analysis of this oxide indicates an oxide of Ni, Al and O, which corresponds with the $NiAl_2O_4$ observed during XRD analysis. It would appear that while a single surface layer of α-alumina has formed and been maintained to some extent, this layer is not continuous to the point of passivating and blocking further oxidation. As such, a fair amount of internal oxidation has occurred in the form of undesirable spinel oxide. In contrast, the cryomilled sample in Figure 7.6J has rather different behaviour. In this case the oxide layer is somewhat thicker and noticeably more continuous, with no exposed substrate regions visible. While a small amount of internal oxidation is present, it has occurred along prior particle boundaries at the beginning of the oxidation test, and has not grown or changed throughout the thermal cycling test. EDS analysis indicates these oxides are Al_2O_3 and not spinel.

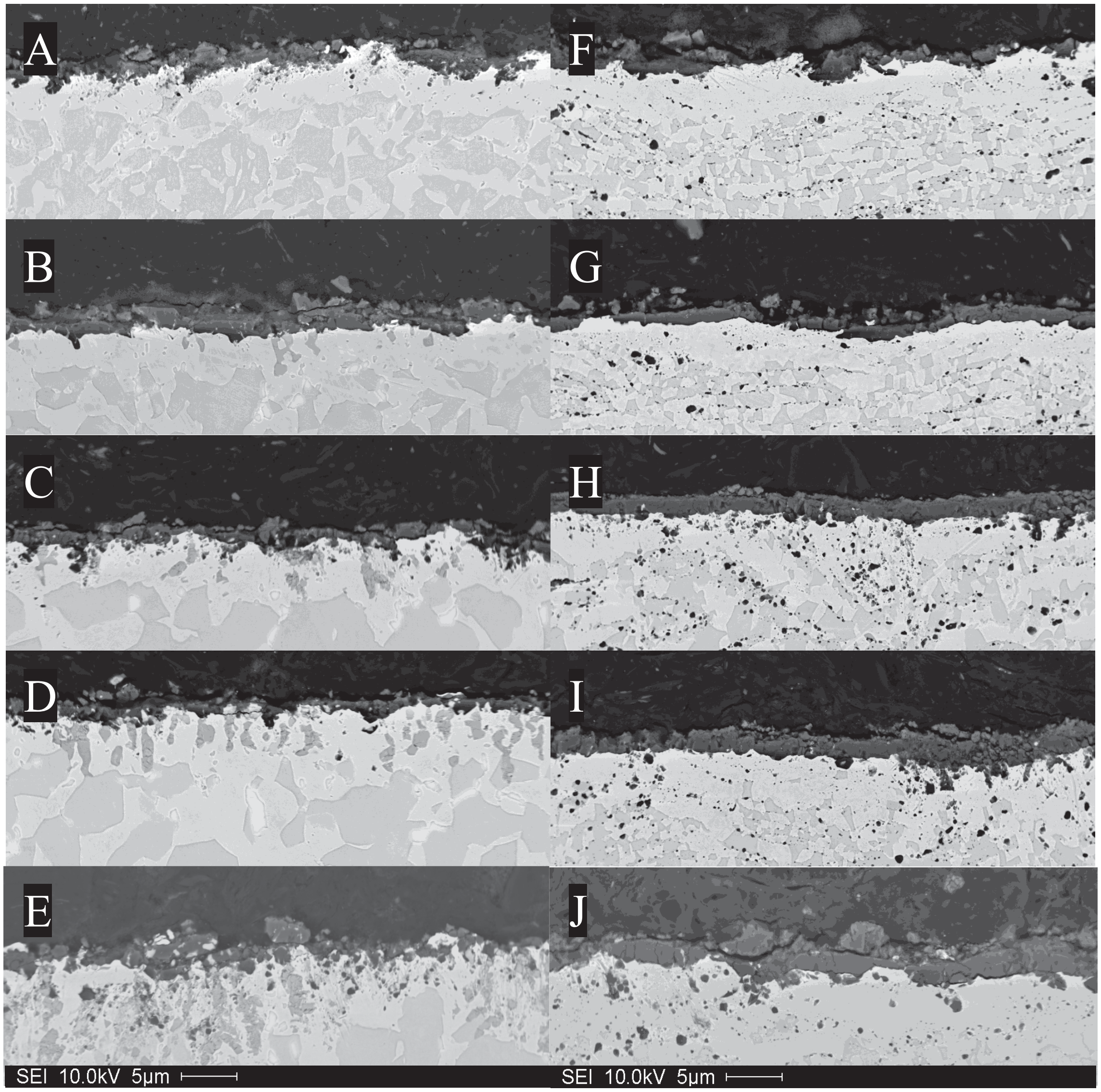

Figure 7.6: Cross-sectional SEM micrographs of conventional NiCoCrAlY samples oxidized for 24, 48, 96, 144, and 200 cycles at 1000°C (A, B, C, D, E) and cryomilled samples oxidized under the same conditions (F, G, H, I, J).

7.4 Discussion

The combined mass gain, XRD and SEM data paint a picture of two somewhat different scenarios for the conventional and cryomilled samples. In the first case, the conventional sample forms an alumina scale that follows the expected θ-α transition and XRD data would indicate that this transition is mostly complete by the end of the oxidation test (200 cycles). Several other studies of similar alloys under thermal cycling conditions have found spinel oxides on the outer surface of the oxide [7.6, 7.17, 7.23, 7.24], however this was not the case for the conventional sample. In contrast, the conventional sample studied herein appears to experience degradation of the alumina scale in the range of 48 to 96 cycles, and this degradation continues throughout the remainder of the oxidation testing. This results in a somewhat discontinuous surface scale through the second half of the oxidation test, which allowed internal oxidation to take place, almost entirely in the form of spinel. Depletion of the β-phase in the surface region of the substrate likely contributed to the internal oxides being primarily spinel and not alumina, as formation of spinel is associated with this depletion [7.6]. Interestingly, the expected mass loss from spallation of the alumina scale appears to be compensated by the ensuing internal oxidation of the conventional NiCoCrAlY, such that mass gain presented in Figure 7.4 continues to increase throughout the test. The study by Unocic and Pint [7.23] also found internal oxidation in a cast Co and Y-doped NiCrAlY alloy. Cao *et al.* studied cyclic oxidation of NiCoCrAlY samples with Hf and Si at 1050°C and found Y and Hf-rich mixed oxide intrusions of varying depth and concentration [7.25].

Unlike the conventional sample, the cryomilled sample does not show a significant level of internal oxidation and does not appear to have formed any spinel oxides after 200 cycles of oxidation at 1000°C. In this case a slightly thicker and more continuous layer of alumina has formed, and similarly undergone the expected θ-α transition. Previous studies by Kaplin *et al.* [7.10, 7.26] have indicated that a reduced grain size has a significant impact on this transition, causing the θ-α transition to occur earlier and reduce overall oxidation rates in the long term.

Several studies on the effect of dopants on the thermal cyclic oxidation of alumina forming alloys have indicated that these dopants improve oxidation performance. It must first be recognized that the θ-Al_2O_3 to α-Al_2O_3 transition follows a regime of α crystallite nucleation on θ-alumina crystallites, followed by growth of the α-alumina phase [7.27]. Lan *et al.* [7.22] have shown that the presence of Dy can provide an increased number of heterogeneous nucleation sites for the formation of α-alumina in the θ-alumina scale on CoNiCrAlY, hence accelerating the θ-α transition and improving overall oxidation performance. This was based on the work of Jedlińsky [7.28] who found that up to a critical concentration, Y accelerates the θ-α transition by providing increased nucleation sites as well as hampering grain growth of metastable aluminas. At the same time, it was noted that mechanically milled alloys should provide a more pronounced effect as the distribution of elements in these alloys will aid in the availability of nucleation sites. Complementing this study, Wang has found that while rare earth element additions can significantly enhance alumina scale adhesion and reduce spallation, nanostructure can have a similar effect [7.29]. Wang found that the increased grain boundary area on the metal surface can increase Al diffusion from the substrate while also providing nucleation sites. This is supported by the work of Mercier *et al.*, who found that grain size reduction also improves aluminum distribution throughout the substrate while increasing the number of pathways for grain boundary diffusion to the surface [7.9]. Additionally, they found that the reduction in grain size reduced the lattice diffusion distance necessary to provide aluminum for oxidation over non-aluminum bearing grains.

Wang also found that adhesion of alumina scales was increased in nanostructured samples, through the formation of oxide pegs that bond the oxide scale to the substrate

[7.29]. These pegs form predominantly at grain boundaries; as such the increased grain boundary area in cryomilled samples can result in more oxide pegs and better scale adhesion. In an interesting parallel to the rare earth effect on the θ-α transition, Li *et al.* have found that the presence of Dy and Hf in NiAl also promotes bonding across the oxide-metal interface, reducing spallation during thermal cycling [7.30]. Similar results have been found by Pint *et al.* in samples with Zr additions [7.31]. Finally using luminescence spectra, Chen *et al.* have found that the volumetric decrease associated θ-α transition can also serve to reduce compressive stresses in the oxide scale, resulting in exceptional oxide adherence in a nanostructured CoCrAlY alloy [7.32].

It is believed that in the conventional samples, stresses induced by thermal cycling resulted in partial spallation and degradation of the alumina scale in the range of 48 to 96 cycles. This degradation allowed oxygen penetration into the substrate, resulting in the internal formation of spinel oxides through the β-depleted zone. In contrast the cryomilled scale demonstrated a continuous and well-adhered alumina scale throughout oxidation testing, with no detectable spallation or internal oxidation, as well as lower overall mass gain. This improved performance is attributed to several factors. First the nanostructured substrate provides increased nucleation sites for α-alumina, accelerating the θ-α transition, which results in a passivating scale that reduces overall oxidation rate. At the same time, the accelerated θ-α transition can reduce compressive stresses in the oxide scale generated by thermal cycling [7.32]. Furthermore, increased grain boundary area on the surface of the substrate can lead to improved scale adhesion through trans-interfacial oxide pegs that form at grain boundaries. The combined effect is the presence of a well adhered, continuous and highly passivating oxide layer on the cryomilled sample, which successfully blocks oxide penetration and prevents the formation of internal spinel oxides seen in the conventional sample. Unsurprisingly, this results in lower overall mass gain in the cryomilled sample throughout the cyclic oxidation test.

7.5 Conclusions

Thermal cyclic oxidation testing of NiCoCrAlY sample with conventional and ultrafine grain size has been conducted. Conventional samples were fabricated via spark plasma sintering of as-received NiCoCrAlY powders, while ultrafine samples were cryomilled prior to sintering. Thermal cycling in air at 1000°C up to 200 cycles has revealed substantially lower mass gain in the cryomilled samples when compared to conventional.

XRD and SEM analysis indicate that while both samples formed a single surface layer of alumina, the conventional sample experienced spallation followed by a significant amount of internal oxidation in the form of $NiAl_2O_4$-spinel oxides while the cryomilled sample did not. This difference in behaviour is attributed to an accelerated θ-α transition resulting in lower oxidation rates, as well as increased scale adherence in the cryomilled sample.

Acknowledgments

The authors would like to thank the Natural Sciences and Engineering Research Council of Canada and Hydro-Quebec for funding this research, as well as Dr. Sriraman Rajagopalan for his help with XRD analysis and Mr. David Walker for his help with cryomilling.

7.6 References

[7.1] R. Rajendran, *Gas turbine coatings – An overview*, Engineering Failure Analysis 26 (2012) 355-369.

[7.2] C. G. Levi, E. Sommer, S. G. Terry, A. Catanoiu, M. Ruhle, *Alumina grown during deposition of thermal barrier coatings on NiCrAlY*, Journal of the American Ceramic Society 86 (2003) 676-685.

[7.3] Q. M. Wang, Y. N. Wu, P. L. Ke, H. T. Cao, J. Gong, C. Sun, L. S. Wen, *Hot corrosion behavior of AIP NiCoCrAlY(SiB) coatings on nickel base superalloys*, Surface and Coatings Technology 186 (2004) 389-397.

[7.4] J. Bursík, P. Broz, J. Popovic, *Microstructure and phase equilibria in Ni-Al-Cr-Co alloys*, Intermetallics 14 (2006) 1257-1261.

[7.5] H.E. Evans, *Oxidation failure of TBC systems: An assessment of mechanisms*, Surface and Coatings Technology, 206 (2011) 1512-1521.

[7.6] G. Margineau and D. Utu, *Cyclic oxidation behaviour of different treated CoNiCrAlY coatings*, Applied Surface Science 258 (2012) 8307-8311.

[7.7] T. Patterson, A. Leon, B Jayaraj, J. Liu, Y.H. Sohn, *Thermal cyclic lifetime and oxidation behavior of air plasma sprayed CoNiCrAlY bond coats for thermal barrier coatings*, Surface & Coatings Technology 203 (2008) 437-441.

[7.8] L. Ajdelsztajn, J. A. Picas, G. E. Kim, F. L. Bastian, J Schoenung, V. Provenzano, *Oxidation behavior of HVOF sprayed nanocrystalline NiCrAlY powder*, Materials Science and Engineering A 338 (2002) 33-43.

[7.9] D. Mercier, C. Kaplin, G. Goodall, G. Kim, M. Brochu, *Parameters influencing the oxidation behavior of cryomilled CoNiCrAlY*, Surface and Coatings Technology 205 (2010) 2546-2553.

[7.10] C. Kaplin, M. Brochu, *Effects of water vapor on high temperature oxidation of cryomilled NiCoCrAlY coatings in air and low-SO_2 environments*, Surface and Coatings Technology 205 (2011) 4221-4227.

[7.11] Z. Liu, W. Gao, K. L. Dahm, F. Wang, *Oxidation behaviour of sputter-depositedNi-Cr-Al micro-crystalline coatings,* Acta Materialia 46 (1998) 1691-1700.

[7.12] F. Tang, L. Ajdelsztajn, J.M. Schoenung, *Influence of Cryomilling on the Morphology and Composition of the Oxide Scales Formed on HVOF CoNiCrAlY Coatings,* Oxidation of Metals 61 (2004) 219-238.

[7.13] S. Todde, R. Licheri, R. Orru, G. Cao, *Spark plasma sintering processing for the evaluation of cryomilled CoNiCrAlY alloys for high temperature applications in oxidizing environment,* Chemical Engineering Journal 200-202 (2012) 68-80.

[7.14] T. H. Nijdam, W. G. Sloof, *Effect of reactive element oxide inclusions on the growth kinetics of protective oxide scales*, Acta Materialia 55 (2007) 5980-5987.

[7.15] B. A. Pint, M. A. Bestor, J A. Haynes, *Cyclic oxidation behavior of HVOF bond coatings deposited on La- and Y-doped superalloys*, Surface and Coatings Technology

206 (2011) 1600-1604.

[7.16] T. Liang, H. Guo, H. Peng, S. Gong, *Cyclic Oxidation Behavior of an EB-PVD CoCrAlY Coating Influenced by Substrate/coating Interdiffusion*, Chinese Journal of Aeronautics 25 (2012) 796-803.

[7.17] H. Lan, Z.-G. Yang, Z.-X. Xia, Y.-D. Zhang, C. Zhang, *Effect of dysprosium addition on the cyclic oxidation behaviour of CoNiCrAlY alloy*, Corrosion Science 53 (2011) 1476-1483.

[7.18] K. Wefers, C. Misra, *Oxides and Hydroxides of Aluminum*, Alcoa Technical paper, 1987.

[7.19] M. W. Brumm, H.J. Grabke, *The oxidation behaviour of NiAl-I. Phase transformations in the alumina scale during oxidation of NiAl and NiAl-Cr alloys.* Corrosion Science 33 (1992) 1677-1690.

[7.20] A. G. Evans, D. R. Mumm, J. W. Hutchinson, G. H. Meier, F. S. Petitt, *Mechanisms controlling the durability of thermal barrier coatings,* Progress in Materials Science 46 (2001) 505-553.

[7.21] B. D. Cullity, Elements of X-Ray Diffraction, 2nd edition, Addison-Wesley, Reading, Massachusetts, 1978.

[7.22] D. Mercier, B. D. Gauntt, M. Brochu, *Thermal stability and oxidation behavior of nanostructured NiCoCrAlY coatings*, Surface & Coatings Technology 205 (2011) 4162-4168.

[7.23] K. A. Unocic, B. A. Pint, *Oxidation behavior of co-doped NiCrAl alloys in dry and wet air*, Surface & Coatings Technology 237 (203) 8-15.

[7.24] P.-C. Tsai, C.-F. Tseng, C.-W. Yang, I.-C. Kuo, Y.-L. Chou, J.-W. Lee, *Thermal cyclic oxidation performance of plasma sprayed zirconia thermal barrier coatings with modified high velocity oxygen fuel sprayed bond coatings*, Surface & Coatings Technology 228 (2013) S11-S14.

[7.25] F. Cao, B. Tryon, C. J. Torbet, T. M. Pollock, *Microstructural evolution and failure characteristics of a NiCoCrAlY bond coat in ''hot spot'' cyclic oxidation*, Acta Materialia 57 (2009) 3885-3894.

[7.26] C. Kaplin, M. Brochu, *The effect of grain size on the oxidation of NiCoCrAlY*, submitted to: Applied Surface Science, 2014.

[7.27] H.-L. Wen, F.-S. Yen, *Growth characteristics of boehmite-derived ultrafne theta and alpha-alumina particles during phase transformation*, Journal of Crystal Growth 208 (2000) 696-708.

[7.28] J. Jedliński, *Comments on the effect of yttrium on the early stages of oxidation of alumina formers*, Oxidation of Metals 39 (1993) 55-60.

[7.29] F. Wang, *The Effect of Nanocrystallization on the Selective Oxidation and Adhesion of* $A1_20_3$ *Scales*, Oxidation of Metals 48 (1997) 215-224.

[7.30] D. Li, H. Guo, H. Peng, S. Gong, H. Xu, *Improved alumina scale adhesion of electron beam physical vapor deposited Dy/Hf-doped β-NiAl coatings*, Applied Surface

Science 283 (2013) 513-520.

[7.31] B. A. Pint, I. G. Wright, W. Y. Lee, Y. Zhang, K. Prüßner, K.B. Alexander, *Substrate and bond coat compositions: factors affecting alumina scale adhesion*, Materials Science and Engineering A 245 (1998) 201-211.

[7.32] G. Chen, M. Rühle, *Transient alumina transformation on a sputtered K38G nanocrystalline coating*, Surface & Coatings Technology 191 (2005) 263-266.

Chapter 8: General Discussion

8.1 Introduction

The goal of this thesis is to study the oxidation behaviour of nanostructured NiAl and NiCoCrAlY alloys, to explore the potential benefits nanostructuring can offer in terms of oxidation performance. The effect of grain refinement on oxidation behaviour is commonly known to be positive [8.1]. Studies have shown that grain refinement, in general terms, can offer increased diffusion pathways in an oxidizing substrate [8.1] while also increasing chemical homogeneity in systems where selective oxidation plays a role [8.2], and both of these effects have been tied to decreased oxidation rates and more protective oxide scales.

This being said, some debate exists as to the effect of grain refinement on the oxidation behaviour of MCrAlY alloys. As discussed in section 1.4, of the few studies that exist most have been focused on nanostructured MCrAlY coatings. In general it is agreed that grain refinement can reduce oxidation rates, though in some studies the formation of a two-layer alumina/spinel scale continues to occur, while in others a single layer of alumina is formed. To the author’s knowledge, only a single study has been performed on the NiCoCrAlY composition explored in this thesis and few of these studies have explored the effect of nanostructuring on bulk MCrAlY alloys, without the coincident effects related to coating deposition.

On the point of coating effects, several of the inconsistencies in reporting also deal with deposition method, namely HVOF. It is generally accepted that deposition via HVOF causes in in-flight oxidation of powders and this results in a dispersion of oxides within the deposited coating, but studies are divided in their opinion of this effect. However, among the few studies on nanostructured MCrAlY’s deposited by HVOF, it would appear that in-flight oxidation is detrimental to oxidation behaviour and surface treatment is required post-spraying.

In order to develop a clearer understanding of the underlying benefits of nanostructure on MCrAlY alloys, this research uses spark plasma sintering to consolidate MCrAlY powders. SPS is a technique with the potential to preserve fine grained or otherwise thermally sensitive microstructures [8.3] that does not involve the high impact velocity, fuel, or in-flight oxidation associated with HVOF. SPS has been chosen to eliminate these potential variables such that the effect of nanostructure can be emphasized. At the same time, developing a broader understanding of the consolidation of NiCoCrAlY powders and nanostructures is essential given the shortage of studies on these subjects.

8.2 Obtaining and Preserving Nanostructure

Grain refinement was obtained in both the NiAl and MCrAlY powders through the cryomilling process. In cryomilling the refined grain structure is formed by the generation of an array of dislocations, which then align and recombine to form sub-grain boundaries. As milling continues, these sub-grain boundaries will slide against one another, changing from small angle grain boundaries to high angle grain boundaries.

The synthesis of NiAl powders from Ni and Al precursor powders has been well documented. Among the most extensive work is that of Joardar *et al.* [8.4, 8.5] and they found that milling times in excess of 20-24 hours were needed to produce intermetallic NiAl. In Chapter 4, however, the precursor powder was NiAl intermetallic, and consequently 16 hours of milling was sufficient to produce nanostructured powders. Additionally, studies to date have focused on mechanical milling without the use of a cryogenic milling medium, which can significantly improve the milled product in terms of reduced oxygen pickup and preventing dynamic recrystallization [8.6]. The NiCoCrAlY powders used in Chapters 5, 6 and 7 were milled using procedures previously established by this research group, and proven to produce nanostructured powders [8.7].

Consolidation of both the cryomilled NiAl and cryomilled NiCoCrAlY powders was first conducted by SPS, though under different conditions for each powder. Due to the extremely high melting point of the NiAl intermetallic (1638°C), a high-temperature sintering profile was necessary, using a peak temperature of 1500°C with a short hold time. This corresponds to 91.5% of melting temperature. NiCoCrAlY powders were sintered at 1100°C, corresponding to 89% of melting temperature. In both cases it was found that short hold times with appropriately adjusted heating ramps helped to preserve nanostructure. The grain size of the final consolidated NiAl was 94 nanometers while the NiCoCrAlY was measured in the range of 109 to 150 nanometers. It is believed that the good thermal stability of intermetallic NiAl has helped in preserving nanostructure throughout the consolidation process.

Consolidation of NiCoCrAlY via HVOF, documented in Chapter 6, is noted a more effective process for preserving grain refinement in cryomilled samples. The same techniques have been used in previous studies [8.7, 8.8] on nanostructured CoNiCrAlY and NiCoCrAlY; in the present work HVOF deposition yielded an average grain size of 10.5 nanometers, an order of magnitude smaller than samples consolidated by SPS. This being said, the flight time in HVOF can be measured in fractions of a second, while the heating time in SPS is on the order of minutes. Both of these techniques have relatively low energy input and can consequently preserve refined grain structure, and SPS has clear advantages discussed in the previous section, but from the perspective solely of preserving nanostructure, HVOF is a markedly better choice.

8.3 Isothermal Oxidation Behaviour

A considerable portion of this thesis is spent exploring the oxidation behaviour of NiAl and NiCoCrAlY samples of various grain sizes and consolidation methods. The parabolic oxidation constants from all of these studies have been compiled in Table 8.1. A clear trends exists in that grain refined samples have consistently lower oxidation rates than corresponding conventional samples for a given system and temperature. This trend is most obvious in the case of nanostructured NiAl samples, which demonstrate a substantial decrease in rate constant with increasing temperature while the conventional samples remain on the same order of magnitude. In the case of NiCoCrAlY samples this trend is less pronounced, in that the oxidation rate does not drop with increasing temperature, but is consistently lower than the equivalent conventional sample. The difference in oxidation behaviour is partly due to the drastic difference in aluminum content between the two alloys, NiAl having 32 wt% aluminum (corresponding to 50 at%) in a single-phase system whereas the NiCoCrAlY alloy has 13 wt% aluminum and is two-phase.

In the case of NiAl it is assumed that the oxidation of aluminum is allowed to proceed with effectively no competing phenomena and the metastable alumina transition is the predominant mechanism. As discussed in Chapter 4, the work of Brumm & Grabke [8.9] reveals a transitional range between 950 and 1050°C where a change from oxidation dominated by θ-alumina to oxidation dominated by α-alumina occurs. It is believed that the drop in oxidation rate is associated with the nanostructured samples proceeding through this change, resulting in the more protective α-alumina forming earlier, and reducing overall oxidation rate.

Table 8.1: Summary of parabolic rate constants found for various systems.

	Parabolic Rate Constant k_p ($g^2/cm^4/s$)					
	Conventional			Cryomilled		
	950°C	1000°C	1050°C	950°C	1000°C	1050°C
SPS						
NiAl	$2.19x10^{-11}$	$3.27x10^{-11}$	$1.42x10^{-11}$	$1.65x10^{-11}$	$2.05x10^{-12}$	$6.78x10^{-13}$
NiAl (2)			$1.58x10^{-11}$			$4.35x10^{-12}$
NiCoCrAlY	$7.64x10^{-13}$	$1.83x10^{-11}$	$5.18x10^{-12}$	$1.71x10^{-13}$	$1.38x10^{-11}$	$4.85x10^{-12}$
HVOF						
NiCoCrAlY					$2.27x10^{-12}$	

In contrast, in the two-phase NiCoCrAlY system, the θ-α transition, while exceedingly important to overall oxidation rate, must also contend with the transient oxidation of the γ-phase and the possibility of forming Ni and Co-based spinel oxides. In this case grain refinement results in lower overall oxidation rates, without the drastic drop in rate constant seen from 950 to 1000 to 1050°C. While conventional samples were not consolidated via HVOF, it is important to note that the nanostructured NiCoCrAlY samples consolidated in this manner reported among the lowest overall oxidation rates at 1000°C for all samples reported, and this despite previous studies indicating that surface modification would be necessary to obtain better oxidation performance [8.7, 8.8].

To complement the overview of oxidation rates presented, the oxide layering behaviour for all samples has also been summarized, in this case in Table 8.2. Each system and condition is noted in terms of single or dual oxide layer as well as the composition of these layers. θ/α refers to a single alumina layer wherein residual θ was still found after the oxidation test, indicating that the θ/α transition was not complete in the 24 hours of oxidation testing. A layer denoted only as α signifies that little or no residual θ was detected, indicating a complete transition. Finally dual layer systems marked with a "+ S" indicate a significant second spinel layer was detected.

Table 8.2: Summary of oxide layering found in various systems.

	Oxide Layering					
	Conventional			Cryomilled		
	950°C	1000°C	1050°C	950°C	1000°C	1050°C
			SPS			
NiAl	Single	Single	Single	Single	Single	Single
	θ/α	θ/α	θ/α	θ/α	α	α
NiAl (2)			Single			Single
			θ/α			α
NiCoCrAlY	Single	Dual	Dual	Single	Single	Single
	θ/α	θ/α + S	θ/α + S	θ/α	θ/α	α
			HVOF			
NiCoCrAlY					Dual	
					α + S	

In the case of NiAl a single oxide layer was found across all conditions, this is not surprising given the higher aluminum content and single-phase structure of this alloy, as discussed above. What is interesting, however, is the variation in the time-temperature relationship of the θ-α transition. As discussed at length in Chapter 4, it would appear that nanostructure accelerates the metastable transition. Conventional samples, across all temperatures, show some residual θ-alumina after 24 hours of oxidation. SEM and XRD data presented in Chapter 4 indicate that the transition tends toward completion with increasing temperature, but still higher temperatures or longer oxidation times would be necessary to witness the full transformation. In contrast the nanostructured samples appear to complete this transition within 24 hours at both 1000 and 1050°C due to the increased number of diffusion paths for aluminum, increased nucleation points for α within the θ alumina matrix and the strain-relief mechanism associated with nanostructure, and discussed in section 4.3.5.

Among the NiCoCrAlY samples consolidated by SPS, two trends are apparent. Firstly, the trend of accelerated θ-α transition revealed in NiAl is maintained but delayed slightly in the NiCoCrAlY samples. Similar to the NiAl oxidation tests, conventional NiCoCrAlY samples show traces of residual θ-alumina at all tested temperatures, indicating an incomplete transition. This is to be expected given the behaviour of conventional NiAl. Among cryomilled samples, the trend is similar in that samples oxidized at lower temperatures continue to evidence residual θ-alumina, whereas higher temperatures have a complete θ-α transition within the 24-hour test period. The difference is that in NiCoCrAlY samples this transition is shifted by one temperature segment, such that residual θ is detected at 950 and 1000°C, but not at 1050°C. Interestingly, in the HVOF-deposited sample, the transition appears to be complete for the alumina layer, with only α-alumina detected. In this case the much smaller grain size noted in the previous section comes in to play, emphasizing the beneficial effect of nanostructure on the θ-α transition.

The second trend among NiCoCrAlY samples is in regard to oxide layering. At 950°C both the conventional and cryomilled samples form only a single layer of alumina and it is believed this is due to the very low oxidation rates found in both of these samples. With very little oxidation occurring, only a small amount of spinel is likely to occur during the initial transient stage, when γ grains are exposed to the oxidative environment. It is believed that with the formation of a complete alumina layer in the early stages of oxidation and subsequent (partial) transformation to α-alumina, this small amount of spinel is not detected at the end of the 24-hour test. At 1000 and 1050°C, however, a dual oxide layer is detected in the conventional samples, and is attributed to both initial transient stage oxidation as well as diffusion through the θ-alumina layer. As discussed in Chapter 5, the transition to α-alumina serves to block diffusion of elements through the oxide scale, and can prevent the formation, or growth, of a second spinel oxide layer. In the case of nanostructured samples, where the θ-α transition appears to be accelerated, this effect is pronounced. Accordingly, cryomilled NiCoCrAlY samples, across all tested temperatures, do not show any significant amount of spinel oxide as a second layer.

The HVOF-deposited NiCoCrAlY sample, despite being nanostructured, formed a dual-layer oxide scale, also despite appearing to complete the θ-α transition. The paradox of this result is indicative of the issues related to HVOF deposition. As found by Mercier *et al.* and Tang *et al.* [8.7, 8.8, 8.10] the in-flight oxidation during HVOF can result in the formation of oxide seeds within the deposited coating, that serve to nucleate spinel oxides and cause the formation of a second oxide layer. They both found that surface treatment was a necessary preventative step, which was not done in the present study. Despite the inconsistencies with regard to in-flight oxidation, the results present in this thesis support the results of Mercier el al. and Tang *et al.* that in-flight oxidation has a negative effect on grain refined MCrAlY alloys. The formation of these oxide seeds and ensuing second oxide layer, however, in no way hindered the accelerated θ-α transition associated with nanostructure.

8.4 Oxidation in real-world conditions

In chapters 4 and 5, it has been shown that grain refinement can have a notable influence on the oxidation behaviour of NiCoCrAlY, both in terms of oxidation rate and in terms of suppression of the second spinel oxide layer for the studied time scales. However, it would be naïve to assume that these benefits will necessarily carry forward to more realistic conditions, where temperature is not isothermally controlled via PID and oxidizing gases are not purified to laboratory grade and bottled. Consequently, in chapters 6 and 7, grain refined NiCoCrAlY samples were subjected to a range of conditions inspired by real environments. In the first case, nanostructured HVOF coatings were subjected to oxidation in environments containing water vapour and low-levels of SO_2, similar to the interior of an oil refinery boiler. In the second case grain refined SPS-consolidated samples were subject to thermal cycling, a common allegory for many turbine components that employ MCrAlY alloys.

The presence of a low level of SO_2 was found to have a relatively little effect on the oxidation behaviour of nanostructured NiCoCrAlY, however the effect of water vapour is pronounced. It was found that water vapour causes a significant increase in oxidation rates through an increase in vacancies in both the alumina and spinel phases. This results in a thickening of the oxide scale and increased internal oxidation. It is noted that, interestingly the increase in oxide scale formation is primarily though thickening of the spinel layer, and that at high enough water vapour levels the thickened spinel layer serves as a diffusion block and reduces internal oxidation, causing a drop in oxidation rates. While this is a fortuitous side effect with regard to degradation of the coating, it is not a desirable outcome. Overall it was found that in the presence of water vapour, the initial transient stage of oxidation is extended and results in substantial overall mass gain, and the potential for internal oxidation. The benefits of nanostructure were notably less pronounced, though it bears mention that coatings tested in this case were not surface treated prior to oxidation.

Under thermal cycling conditions, the benefits of nanostructure were more apparent. In this case the accelerated θ-α transition in the cryomilled sample appears to have yielded a better adhered and more protective oxide scale, effectively suppressing the formation of a second spinel layer while also preventing internal oxidation. It was found that in conventional samples spallation of the oxide layer led to internal oxidation in the form of spinels and increased overall mass gain. In this case consolidated SPS samples were independent of HVOF spray-effects and showed a significant improvement in behaviour among grain-refined samples.

8.5 Industrial Considerations

Examining the results presented in chapters 4 through 7, several considerations can be put forth, from the perspective of realistic implementation of nanostructured NiCoCrAlY. It is clear that grain refinement or nanostructuring can impact the metastable θ-α transition in NiCoCrAlY and effectively accelerate this transition, causing the formation of a complete and stable α-alumina layer at lower oxidation temperatures or in less oxidation time (or both). The earlier transition to α-alumina has the potential to delay the formation of the second spinel oxide layer and results in lower overall oxidation rates and, in the case of thermal cycling, can prevent coating spallation, at least up to 200 cycles. Accordingly, it is believed that nanostructured or grain refined NiCoCrAlY has the potential to offer significant improvements to oxidation resistance and component lifetime. This being said, the benefits of nanostructure can be negated through processing and environmental factors. It has been found that the in-flight oxidation occurring in HVOF deposition can be detrimental, as can exposure to systems containing water vapour, at least in cases where no post-spraying treatment is conducted.

SPS consolidation has been proven a reliable method for creating bulk grain refined NiCoCrAlY components, but because SPS is a batch process that can be geometrically constrained, it faces a number of limitations in terms of industrial adoption. In contrast, HVOF can also be used to fabricate nanostructured NiCoCrAlY coatings, and already has a strong industrial following. It is believed that if nanostructured NiCoCrAlY coatings are to be adopted by industry this will most likely be through HVOF.

An interesting note in this regard is the industrial trend of annealing or heat-treating HVOF coatings post-spraying in order to consolidate inter-particle bonds and close pores. While this process is a current industry standard, given the temperature-sensitive nature of nanostructured materials, it could be detrimental to nanostructured coatings. Eliminating this step and replacing it with a rapid surface treatment such as shot peening, grit-blasting or low-pressure burnishing could save time and expense, and help to offset the increased material cost associated with nanostructured powders. This would have the added benefit of eliminating surface oxide seeds picked up in-flight and allowing the improved oxidation behaviour to manifest. Surface treatment in and of itself may be enough to counteract the detrimental effects of water vapour. Failing this it is believed a short pre-oxidation step, allowing the α-alumina to form prior to exposure to water vapour, would be ideal.

8.6 References

[8.1] B.A. Pint, *High Temperature Corrosion of Alumina-forming Iron, Nickel and Cobalt-base Alloys* in: Shrier's Corrosion, Elsevier, Oxford, 2010, 606-645.

[8.2] H. Habazaki, *Corrosion of Amorphous and Nanograined Alloys* in: Shrier's Corrosion, Elsevier, Oxford, 2010, 2192-2204.

[8.3] J. He, J. M. Schoenung, *Review: Nanostructured Coatings*, Materials Science and Engineering A 336 (2002) 274-319.

[8.4] J. Joardar, S. K. Pabi, H.-J. Fecht, B. S. Murty, *Stability of nanocrystalline disordered NiAl synthesized by mechanical alloying*, Philosophical Magazine Letters 82 (2002) 469-475.

[8.5] J. Joardar, S.K. Pabi and B.S. Murty, *Milling criteria for the synthesis of nanocrystalline NiAl by mechanical alloying*, Journal of Alloys and Compounds, Volume 429, Issues 1–2, 21 February 2007, Pages 204-210.

[8.6] C. Suryanarayana, *Mechanical alloying and milling,* Progress in Materials Science 46 (2001) 1-184.

[8.7] D. Mercier, B. D. Gauntt, M. Brochu, *Thermal stability and oxidation behavior of nanostructured NiCoCrAlY coatings*, Surface and Coatings Technology 205 (2011) 4162-4168.

[8.8] D. Mercier, C. Kaplin, G. Goodall, G. Kim, M. Brochu, *Parameters influencing the oxidation behavior of cryomilled CoNiCrAlY*, Surface and Coatings Technology 205 (2010) 2546-2553.

[8.9] M. W. Brumm, H. J. Grabke, *The oxidation bahaviour of NiAl - I. Phase transformations in the alumina scale during oxidation of NiAl and NiAl-Cr alloys*, Corrosion Science 33 (1992) 1677-1690.

[8.10] F. Tang, L. Ajdelsztajn, G. E. Kim, V. Provenzano, J. M. Schoenung, *Effects of surface oxidation during HVOF processing on the primary stage oxidation of a CoNiCrAlY coating*, Surface and Coatings Technology 185 (2004) 228-233.

Chapter 9: Summary

The goal of this thesis is to study the oxidation behaviour of nanostructured NiAl and NiCoCrAlY alloys; a summary of the investigations made is presented here:

1. The isothermal oxidation behaviour of conventional and nanostructured NiAl samples consolidated by SPS was investigated by thermogravimetric analysis. Oxidation rates for nanostructured samples decreased with increasing temperature, as low as 6.78×10^{-13} $g^2/cm^4/s$, notably lower than conventional samples that remained on the order of 10^{-11} $g^2/cm^4/s$. This trend is associated with a shift from θ-alumina dominated oxidation to α-alumina. Overall reduced oxidation rates for nanostructured samples are the result of this accelerated θ-α transition, which is cause by increased pathways for aluminum diffusion, increased nucleation points for α-alumina, and exothermic strain relief occurring in the nanostructured sample.
2. Following this, the isothermal oxidation behaviour of conventional and grain refined NiCoCrAlY itself was studied, in similarly SPS consolidated samples. It was found that the accelerated θ-α transition noted for grain refined NiAl samples carries forward into similarly refined NiCoCrAlY samples, resulting in lower overall oxidation rates and supressing the formation of a second spinel layer. A change in oxidation behaviour with increasing temperature was also noted, and once again associated with a shift of dominant oxidation in the θ-α transition.
3. The effect of environment on nanostructured HVOF-deposited NiCoCrAlY coatings was explored though oxidation tests in an environment containing SO_2 and varying levels of water vapour. While the presence of SO_2 is found to have little effect on oxidation kinetics, the effect of water vapour is twofold. First, the

presence of water vapour extends the transient oxidation stage resulting in the internal oxidation of the NiCoCrAlY coatings. Second, this extended transient oxidation stage also results in significant thickening of the second spinel layer. Overall oxidation rates were drastically increased with increasing vapour level, up to the point that the thickened spinel layer itself acts as a diffusion block, and thereby lowering oxidation rates.

4. Finally the thermal cycling behaviour of conventional and grain refined NiCoCrAlY samples was investigated. Total mass gain after 200 cycles averaged 0.29 mg/cm^2 in the conventional samples and 0.22 mg/cm^2 in the cryomilled samples. Greater mass gain in the conventional samples is associated with scale spallation and subsequent internal oxidation in the form of spinels. Nanostructured samples demonstrated a single, consistent layer of α-alumina and no internal oxidation. The improved performance is attributed to increased scale adhesion and stress relief in the nanostructured sample, as well as an earlier θ-α transition resulting in lower overall mass gain.

Chapter 10: Contributions to Original Knowledge

This final chapter presents the most significant contributions to scientific knowledge that have arisen from this research.

1. The first study on the oxidation behaviour of nanostructured, SPS-consolidated NiAl was performed.
    a. The effects of nanostructure on increased aluminum diffusion pathways, increased sites for α-alumina nucleation and increased distribution of aluminum throughout the substrate have been shown to accelerate the θ-α transition resulting in lower overall oxidation rates.
    b. The catalytic effect of exothermic strain relief in nanostructured NiAl has been established as a key factor in accelerating the θ-α transition, which can occur approximately 150°C lower in nanostructured samples.
2. Similarly, the first study on the isothermal oxidation behaviour of nanostructured, SPS-consolidated NiCoCrAlY was performed.
    a. It has been shown that the effects of nanostructure identified in NiAl are equally present in NiCoCrAlY and can accelerate the θ-α transition, resulting in lower overall oxidation rates as well as improved performance under thermal cycling.
3. The first in-depth investigation of the oxidation of nanostructured NiCoCrAlY in the presence of water vapour and SO_2 was carried out. The effect of water vapour in extending the transient oxidation stage, resulting in increased internal oxidation and spinel formation was identified.

4. A more comprehensive understanding of the impact of grain refinement on the oxidation performance of MCrAlY alloys has been established, both under isothermal and non-isothermal conditions. Included herein is an understanding of the potential negating effects of HVOF deposition and the presence of water vapour.